Computer Methods in Applied Mechanics and Engineering 452 (2026) 118742

Contents lists available at ScienceDirect

Comput. Methods Appl. Mech. Engrg.

journal homepage: www.elsevier.com/locate/cma

Symmetrisation and hyperbolicity of first-order conservation laws in large strain compressible viscoelasticity using the smoothed particle hydrodynamics method

Chun Hean Lee [a,*], Antonio J. Gil [b,*], Tadas Jaugielavičius [a], Thomas Richardson [b], Sébastien Boyaval [c,d], Damien Violeau [c,e], Javier Bonet [f,g]

[a] Glasgow Computational Engineering Centre (GCEC), James Watt School of Engineering, University of Glasgow, United Kingdom
[b] Zienkiewicz Institute for Modelling, Data and AI, Faculty of Science and Engineering, Swansea University, Bay Campus, United Kingdom
[c] LHSV, ENPC, Institut Polytechnique de Paris EDF R&D, Chatou, France
[d] Inria, France
[e] EDF R&D/ LNHE, 6 quai Watier, Chatou, 78400, France
[f] Centre Internacional de Mètodes Numèrics en Enginyeria (CIMNE), Barcelona, Spain
[g] Departament de Enginyeria Civil i Ambiental (DECA), Universitat Politècnica de Catalunya, Barcelona, Spain

ARTICLE INFO

Keywords:
Solid dynamics
Conservation laws
Smoothed particle hydrodynamic
Viscoelasticity
Riemann solver
Large strain

ABSTRACT

This paper presents a new first-order hyperbolic framework with relaxation (or dissipation) terms for large strain viscoelastic solids. The framework is based on a compressible Maxwell-type viscoelastic model and integrates linear momentum conservation, geometric conservation laws, and evolution equations for internal variables. First, we propose a polyconvex strain energy function that is jointly convex with respect to the deformation measures and internal variables. Second, we introduce a generalised convex entropy function to symmetrise the hyperbolic system in terms of dual conjugate (entropy) variables. Third, we demonstrate that the system is hyperbolic (i.e., real wave speeds) under all deformation states, and that the relaxation terms correctly capture viscoelastic dissipation. Fourth, we present an upwinding Smoothed Particle Hydrodynamics (SPH) [1–3] scheme that enforces the second law of thermodynamics semi-discretely and uses the time rate of the generalised convex entropy to monitor internal dissipation and stabilise the simulation. Finally, the proposed framework is validated through numerical examples and benchmarked against the in-house Updated Reference Lagragian SPH [2,3] and vertex-centred finite volume [4–7] algorithms, demonstrating stability, accuracy, and consistent energy dissipation.

1. Introduction

Viscoelastic materials exhibit both elastic and viscous behaviour and can store energy whilst dissipating it over time. This dual response makes them indispensable in impact and shock problems, where controlled energy and damping are required. Applications include protective structures, vibration and noise reduction systems, flexible wave energy converters, and a wide range of engineered and biological materials. To model these behaviours, we require frameworks that can capture large deformations together with time-dependent dissipation.

* Corresponding authors.
E-mail addresses: chunhean.lee@glasgow.ac.uk (C.H. Lee), a.j.gil@swansea.ac.uk (A.J. Gil).

https://doi.org/10.1016/j.cma.2026.118742
Received 15 October 2025; Received in revised form 12 December 2025; Accepted 6 January 2026
Available online 28 January 2026

The majority of viscoelastic models [8–13] for large strain solids are based on Maxwell-type formulations. These phenomenological models typically decompose the deformation gradient into elastic and viscous components [8,12–15], and their internal variables evolve in a manner that guarantees thermodynamically consistent dissipation [16]. An alternative class of models is based on hereditary integrals, which generalise linear viscoelasticity to large deformations using relaxation functions [17,18]. In this formulation, viscous effects are incorporated directly into the stress-strain relationship through a time history integral that accounts for the fading memory of the material [19–21]. In computational solid dynamics, Maxwell-type viscoelastic models have been extensively implemented using finite element methods, in particular the Variational Multi-Scale (VMS) Finite Element Method [22,23]. Scovazzi et al. [22] demonstrated the use of Prony series representations within the VMS framework, and subsequent extensions incorporated a multiplicative decomposition of viscoelasticity [23]. Importantly, for dynamic simulations, maintaining hyperbolicity is crucial to ensure real wave speeds and a well-posed evolution [24]. A natural way to achieve this is through the formulation of a symmetric hyperbolic system, which is a main objective of the present work.

To achieve this, we propose a compressible polyconvex viscoelastic model, inspired by Boyaval's approach to polyconvexity in viscoelastic solids [25]. In our work, we introduce an extended set of internal variables $\boldsymbol{\mathcal{Y}} = \{\boldsymbol{Y}_a, y_1, \dots, \boldsymbol{Y}_{n_\mathrm{M}}, y_{n_\mathrm{M}}\}$ to represent the time-dependent (viscous) response of the material, where n_M denotes the total number of Maxwell branches. The strain energy function is additively decomposed into an equilibrium (long-term) part and a non-equilibrium (time-dependent) part, with the latter formulated to ensure thermodynamic consistency. As the viscous strain evolves, the viscous strain energy decays and eventually vanishes once the viscous strain matches the total strain, indicating the physical relaxation of the material. Furthermore, the strain energy is formulated to be convex with respect to both the triplet of deformation measures $\boldsymbol{\mathcal{X}} = \{\boldsymbol{F}, \boldsymbol{H}, J\}$ and the internal variables $\boldsymbol{\mathcal{Y}}$, yielding a framework that is jointly convex in both $\boldsymbol{\mathcal{X}}$ and $\boldsymbol{\mathcal{Y}}$. This extends our previous work [1,26,27], which focused only on hyperelastic models with a strain energy convex in $\boldsymbol{\mathcal{X}}$.

This joint convexity naturally leads to the introduction of a generalised convex entropy function, which incorporates the (convex) kinetic energy together with the polyconvex strain energy. This allows the hyperbolic system to be symmetrised in terms of dual (entropy) variables. Symmetrisation ensures a consistent thermodynamic structure, making the system both mathematically useful (i.e., solutions exist and are both unique and stable) and physically meaningful (i.e., energy and dissipation evolve correctly), consistent with the principle of causality and determinism. Within this symmetric framework, we demonstrate the system is hyperbolic, guaranteeing real wave speeds across any deformation states and ensuring stable propagation of elastic waves. The relaxation terms correctly capture viscoelastic dissipation, providing energy attenuation during dynamic processes.

For spatial discretisation, we implement an upwinding Smoothed Particle Hydrodynamics (SPH) scheme based on the acoustic Riemann solver, with a linear reconstruction procedure to achieve second-order accuracy. The SPH scheme ensures semi-discrete satisfaction of the second law of thermodynamics by evaluating numerical stabilisation using the time rate of the generalised convex entropy. In the numerical examples presented in the current paper, we monitor both internal dissipation and numerical dissipation introduced by the upwinding procedure. Both dissipation rates remain non-negative, respecting the second law of thermodynamics. In practice, internal dissipation quantifies the energy dissipated by the viscoelastic material, whereas numerical dissipation measures the energy loss introduced by the algorithm and helps verify its consistency.

For temporal integration, we employ an explicit three-stage Runge-Kutta time integrator. The evolution of internal variables is integrated analytically in time by solving a first-order non-homogeneous ordinary differential equation. A series of benchmark test cases with smooth solutions is presented to assess the robustness and accuracy of the algorithm, including a manufactured solution to verify the order of convergence. The proposed SPH framework is benchmarked against an in-house Updated Reference Lagrangian SPH algorithm [2,3] and a vertex-centred finite volume method to evaluate consistency and accuracy.

The paper is organised as follows. Section 2 revisits the standard viscoelasticity at large strains. Extension to a polyconvex model and the symmetrisation of the hyperbolic system are discussed in Section 3, where a symmetric hyperbolic system expressed in terms of conjugate entropy variables is also presented. Section 4 demonstrates the hyperbolicity proof and the relaxation response of the system. Sections 5 and 6 describe the associated SPH discretisation and the explicit time integration scheme used. Several numerical examples are presented in Section 7, and concluding remarks and future work are discussed in Section 8. Appendix A provides the expressions for the conjugate stress components and Hessian of the proposed viscoelastic model. Appendices B and C present the procedures for obtaining numerical stabilisation via the second law of thermodynamics, and for deriving the Cauchy stress tensor and the evolution of internal variables for linear viscoelasticity, which are needed to construct the exact solution for the manufactured problem.

2. Revisiting classical large strain viscoelasticity

Consider the motion of a continuum whose material (or initial) configuration is defined by the domain Ω_R with boundary $\partial\Omega_R$ and unit outward normal vector $\boldsymbol{N}$. After deformation, the continuum occupies the spatial (or current) configuration $\Omega(t)$ with boundary $\partial\Omega(t)$ and outward unit normal $\boldsymbol{n}$. The motion is described by a time-dependent mapping field $\boldsymbol{\phi}(\boldsymbol{X}, t)$, which relates a material point $\boldsymbol{X}$ to its spatial position $\boldsymbol{x}$ via $\boldsymbol{x} = \boldsymbol{\phi}(\boldsymbol{X}, t)$. The governing equation of motion in the material configuration is

$$\frac{\partial \boldsymbol{p}_R}{\partial t} - \mathrm{DIV}\boldsymbol{P} = \boldsymbol{f}_R; \qquad \boldsymbol{p}_R = \rho_R \boldsymbol{v}, \tag{1}$$

where $\boldsymbol{p}_R$ is the linear momentum (per unit material volume), $\boldsymbol{v}$ is the velocity, ρ_R is the material density (per unit material volume), $\boldsymbol{P}$ is the first Piola-Kirchhoff stress tensor, $\boldsymbol{F} = \frac{\partial \boldsymbol{\phi}(\boldsymbol{X},t)}{\partial \boldsymbol{X}}$ is the deformation gradient tensor, and $\boldsymbol{f}_R$ is the body force per unit material volume.

Classically, in isothermal viscoelasticity [8,28], the strain energy density Ψ (defined per unit undeformed volume) depends on $\boldsymbol{F}$ and a set of internal state variables $\boldsymbol{C}_{v_\alpha}^{-1}$, representing the inverse of a viscous type right Cauchy-Green strain tensor, where $\alpha = 1, \dots, n_{\mathrm{M}}$, with n_{M} denoting the number of Maxwell branches describing the viscoelastic response [9,22]. This dependence is written as $\Psi = \Psi(\boldsymbol{F}, \boldsymbol{C}_{v_1}^{-1} \dots \boldsymbol{C}_{v_{n_{\mathrm{M}}}}^{-1})$[1] [10]. The strain energy can be additively decomposed into an equilibrium (long-term) component, Ψ_∞, and non-equilibrium (time-dependent) viscous contributions, Ψ_α, given as follows [10]

$$\Psi\left(\boldsymbol{F}, \boldsymbol{C}_{v_1}^{-1} \dots \boldsymbol{C}_{v_{n_{\mathrm{M}}}}^{-1}\right) = \Psi_\infty(\boldsymbol{F}) + \sum_{\alpha=1}^{n_{\mathrm{M}}} \Psi_\alpha\left(\boldsymbol{F}, \boldsymbol{C}_{v_\alpha}^{-1}\right). \tag{2}$$

For thermodynamic equilibrium [9], the viscous terms Ψ_α and their derivatives with respect to the deformation gradient and internal variables must vanish when the material is fully relaxed. This occurs when the viscous deformation tensor $\boldsymbol{C}_{v_\alpha}^{-1}$ aligns with the inverse of total right Cauchy-Green strain tensor, defined as $\boldsymbol{C}^{-1} = \boldsymbol{F}^{-1}\boldsymbol{F}^{-T}$. Mathematically, these conditions are expressed as

$$\Psi_\alpha(\boldsymbol{F}, \boldsymbol{C}_{v_\alpha}^{-1} = \boldsymbol{C}^{-1}) = 0; \qquad \left.\frac{\partial \Psi_\alpha(\boldsymbol{F}, \boldsymbol{C}_{v_\alpha}^{-1})}{\partial \boldsymbol{F}}\right|_{\boldsymbol{C}_{v_\alpha}^{-1} = \boldsymbol{C}^{-1}} = \boldsymbol{0}; \qquad \left.\frac{\partial \Psi_\alpha(\boldsymbol{F}, \boldsymbol{C}_{v_\alpha}^{-1})}{\partial \boldsymbol{C}_{v_\alpha}^{-1}}\right|_{\boldsymbol{C}_{v_\alpha}^{-1} = \boldsymbol{C}^{-1}} = \boldsymbol{0}. \tag{3}$$

These conditions ensure that the material reaches a long-term equilibrium state with no further internal energy dissipation due to viscous effects.

From a thermodynamic perspective, the internal dissipation [30] (or local entropy production [31]) $\dot{\mathcal{D}}_{\mathrm{int}}$ in isothermal viscoelasticity is given by

$$\begin{aligned} 0 \le \dot{\mathcal{D}}_{\mathrm{int}} &= \boldsymbol{P} : \dot{\boldsymbol{F}} - \dot{\Psi}(\boldsymbol{F}, \boldsymbol{C}_{v_1}^{-1} \dots \boldsymbol{C}_{v_{n_{\mathrm{M}}}}^{-1}) \\ &= \left(\boldsymbol{P} - \frac{\partial \Psi(\boldsymbol{F}, \boldsymbol{C}_{v_1}^{-1} \dots \boldsymbol{C}_{v_{n_{\mathrm{M}}}}^{-1})}{\partial \boldsymbol{F}}\right) : \frac{\partial \boldsymbol{F}}{\partial t} - \sum_{\alpha=1}^{n_{\mathrm{M}}} \frac{\partial \Psi(\boldsymbol{F}, \boldsymbol{C}_{v_1}^{-1} \dots \boldsymbol{C}_{v_{n_{\mathrm{M}}}}^{-1})}{\partial \boldsymbol{C}_{v_\alpha}^{-1}} : \frac{\partial \boldsymbol{C}_{v_\alpha}^{-1}}{\partial t}. \end{aligned} \tag{4}$$

Here, the overdot $[\dot{\bullet}]$ denotes the material time derivative. Since $\frac{\partial \boldsymbol{F}}{\partial t}$ is arbitrary, the multiplier of $\frac{\partial \boldsymbol{F}}{\partial t}$, that is $\boldsymbol{P} - \frac{\partial \Psi(\boldsymbol{F}, \boldsymbol{C}_{v_1}^{-1} \dots \boldsymbol{C}_{v_{n_{\mathrm{M}}}}^{-1})}{\partial \boldsymbol{F}}$, must vanish for the dissipation inequality to hold for under all admissible processes. This leads to the constitutive relation for the first Piola-Kirchhoff stress tensor as

$$\boldsymbol{P}(\boldsymbol{F}, \boldsymbol{C}_{v_1}^{-1} \dots \boldsymbol{C}_{v_{n_{\mathrm{M}}}}^{-1}) = \boldsymbol{P}_\infty(\boldsymbol{F}) + \sum_{\alpha=1}^{n_{\mathrm{M}}} \boldsymbol{P}_\alpha(\boldsymbol{F}, \boldsymbol{C}_{v_\alpha}^{-1}); \qquad \boldsymbol{P}_\square = \frac{\partial \Psi_\square}{\partial \boldsymbol{F}}; \qquad \square = \{\infty, \alpha\}. \tag{5}$$

The stresses depend on the deformation gradient and internal variables describing viscoelastic effects. The remainder inequality (4) simplifies to[2]

$$0 \le \dot{\mathcal{D}}_{\mathrm{int}} = -\sum_{\alpha=1}^{n_{\mathrm{M}}} \frac{\partial \Psi_\alpha(\boldsymbol{F}, \boldsymbol{C}_{v_1}^{-1} \dots \boldsymbol{C}_{v_{n_{\mathrm{M}}}}^{-1})}{\partial \boldsymbol{C}_{v_\alpha}^{-1}} : \frac{\partial \boldsymbol{C}_{v_\alpha}^{-1}}{\partial t}. \tag{6}$$

Suitable evolution equations[3] for the internal variables $\boldsymbol{C}_{v_\alpha}^{-1}$ must be defined to ensure both the dissipation inequality (6) and thermodynamic equilibrium. Viscoelastic formulations are designed to satisfy the dissipation inequality (also referred to as relaxation behaviour due to internal dissipation), but this alone does not necessarily guarantee hyperbolicity of the governing equations. Without hyperbolicity, the system may lack real-valued wave speeds. This property is important in solid dynamics to ensure finite propagation wave speeds and the well-posedness of initial boundary value problems.

3. Polyconvexity, convex entropy function, and symmetrisation in first-order systems

One approach to ensure hyperbolicity in systems with relaxation terms is to reformulate the conservation-law system in symmetric hyperbolic form through the introduction of a convex entropy function [25,32–35]. The following discussion is general and applies to any first-order system, including those with relaxation terms. Such a system can be written as

$$\frac{\partial \boldsymbol{\mathcal{U}}}{\partial t} + \sum_{I=1}^{3} \frac{\partial \boldsymbol{\mathcal{F}}_I}{\partial X_I} = \boldsymbol{\mathcal{S}}(\boldsymbol{\mathcal{U}}); \qquad \boldsymbol{\mathcal{S}}(\boldsymbol{\mathcal{U}}) = \boldsymbol{\mathcal{S}}_{\mathrm{ext}} + \boldsymbol{\mathcal{R}}(\boldsymbol{\mathcal{U}}); \qquad \boldsymbol{\mathcal{R}}(\boldsymbol{\mathcal{U}}) = \sum_{\alpha=1}^{n_{\mathrm{M}}} \boldsymbol{\mathcal{R}}_\alpha(\boldsymbol{\mathcal{U}}). \tag{7}$$

[1] Frame-indifference [28,29] requires that Ψ be equivalently expressed in terms of the right Cauchy-Green strain tensor $\boldsymbol{C}$ and internal state variables $\boldsymbol{C}_{v_\alpha}^{-1}$, described by

$$\Psi(\boldsymbol{F}, \boldsymbol{C}_{v_1}^{-1} \dots \boldsymbol{C}_{v_{n_{\mathrm{M}}}}^{-1}) = \tilde{\Psi}(\boldsymbol{C}, \boldsymbol{C}_{v_1}^{-1} \dots \boldsymbol{C}_{v_{n_{\mathrm{M}}}}^{-1}); \qquad \boldsymbol{C} = \boldsymbol{F}^T\boldsymbol{F}.$$

[2] For hyperelastic materials under isothermal conditions, the internal dissipation vanishes since no viscous effects are present.

[3] Physically, these equations describe how the internal variables evolve due to microstructural rearrangement under deformation.

Here, $\boldsymbol{\mathcal{U}}$ denotes the set of conservation variables and $\boldsymbol{\mathcal{F}}_I(\boldsymbol{\mathcal{U}})$ is the flux vector in the material Cartesian direction I. The source term $\boldsymbol{\mathcal{S}}(\boldsymbol{\mathcal{U}})$ can be decomposed into two contributions. Specifically, $\boldsymbol{\mathcal{S}}_{\text{ext}}$ accounts for external sources such as body forces, and $\boldsymbol{\mathcal{R}}$ the relaxation contribution. The relaxation term itself is a sum of branch contributions $\sum_{\alpha=1}^{n_{\text{M}}} \boldsymbol{\mathcal{R}}_\alpha(\boldsymbol{\mathcal{U}})$, each describing the evolution of internal variables associated with Maxwell branch α. The following conditions (summarised from Chen, Levermore, and Liu [35]) ensure symmetric hyperbolicity [36,37] of the system (7) and thermodynamically consistent treatment of relaxation (or dissipation) effects:

(i) Existence of a convex entropy function S, which requires a polyconvex viscoelastic energy density W consistent with thermodynamic equilibrium.
(ii) Positive definiteness of the Hessian operator $\frac{\partial^2 S}{\partial \boldsymbol{\mathcal{U}} \partial \boldsymbol{\mathcal{U}}}$, ensuring the existence of a suitable symmetriser for the system.
(iii) Symmetry of the flux Jacobian matrices in entropy variables, expressed by $\boldsymbol{\mathcal{A}}_I \boldsymbol{\mathcal{A}}_0$, with $\boldsymbol{\mathcal{A}}_I = \frac{\partial \boldsymbol{\mathcal{F}}_I}{\partial \boldsymbol{\mathcal{U}}}$ and $\boldsymbol{\mathcal{A}}_0 = \left[\frac{\partial^2 S}{\partial \boldsymbol{\mathcal{U}} \partial \boldsymbol{\mathcal{U}}}\right]^{-1}$.
(iv) Satisfaction of the dissipation inequality $-\sum_{\alpha=1}^{n_{\text{M}}} \boldsymbol{\mathcal{V}}^T \boldsymbol{\mathcal{R}}_\alpha \geq 0$, where $\boldsymbol{\mathcal{V}} = \frac{\partial S}{\partial \boldsymbol{\mathcal{U}}}$ denotes the conjugate entropy variables, guaranteeing non-negative entropy production during relaxation.

In what follows, condition (i) is first addressed through the formulation of a polyconvex viscoelastic model and the associated evolution equations for internal variables. Building on this, we construct the generalised convex entropy function by combining the polyconvex strain energy density with the kinetic energy, thereby obtaining its conjugate variables and Hessian components (as required by condition (ii)). This structure then enables the symmetrisation of the hyperbolic system to obtain its dual formulation in terms of entropy conjugate variables (as required by condition (iii)). Finally, we demonstrate that the source term associated with relaxation effects satisfies the dissipation inequality, as required by condition (iv).

Remark 1. To prove hyperbolicity, we linearise[4] the system in (7) about a reference state $\bar{\boldsymbol{\mathcal{U}}}$, typically chosen at thermodynamic equilibrium. Let $\delta\boldsymbol{\mathcal{U}} = \boldsymbol{\mathcal{U}} - \bar{\boldsymbol{\mathcal{U}}}$ denote a small perturbation. Linearising the fluxes and source terms about this state gives

$$\boldsymbol{\mathcal{F}}_I(\boldsymbol{\mathcal{U}}) \approx \boldsymbol{\mathcal{F}}_I(\bar{\boldsymbol{\mathcal{U}}}) + \underbrace{D\boldsymbol{\mathcal{F}}_I[\delta\boldsymbol{\mathcal{U}}]}_{\frac{\partial \boldsymbol{\mathcal{F}}_I}{\partial \boldsymbol{\mathcal{U}}}\Big|_{\bar{\boldsymbol{\mathcal{U}}}} \delta\boldsymbol{\mathcal{U}}}; \qquad \boldsymbol{\mathcal{S}}(\boldsymbol{\mathcal{U}}) \approx \boldsymbol{\mathcal{S}}(\bar{\boldsymbol{\mathcal{U}}}) + \underbrace{D\boldsymbol{\mathcal{S}}[\delta\boldsymbol{\mathcal{U}}]}_{\frac{\partial \boldsymbol{\mathcal{S}}}{\partial \boldsymbol{\mathcal{U}}}\Big|_{\bar{\boldsymbol{\mathcal{U}}}} \delta\boldsymbol{\mathcal{U}}}. \tag{8}$$

We then introduce the flux Jacobian matrix $\boldsymbol{\mathcal{A}}_I(\bar{\boldsymbol{\mathcal{U}}}) = \frac{\partial \boldsymbol{\mathcal{F}}_I}{\partial \boldsymbol{\mathcal{U}}}\Big|_{\bar{\boldsymbol{\mathcal{U}}}}$ and the relaxation Jacobian matrix $\boldsymbol{\mathcal{J}}(\bar{\boldsymbol{\mathcal{U}}}) = \frac{\partial \boldsymbol{\mathcal{S}}}{\partial \boldsymbol{\mathcal{U}}}\Big|_{\bar{\boldsymbol{\mathcal{U}}}} = \sum_{\alpha=1}^{n_{\text{M}}} \frac{\partial \boldsymbol{\mathcal{R}}_\alpha}{\partial \boldsymbol{\mathcal{U}}}\Big|_{\bar{\boldsymbol{\mathcal{U}}}}$, both evaluated at the reference state $\bar{\boldsymbol{\mathcal{U}}}$. The resulting linearised system is

$$\frac{\partial \delta\boldsymbol{\mathcal{U}}}{\partial t} + \sum_{I=1}^{3} \boldsymbol{\mathcal{A}}_I(\bar{\boldsymbol{\mathcal{U}}}) \frac{\partial \delta\boldsymbol{\mathcal{U}}}{\partial X_I} = \boldsymbol{\mathcal{J}}(\bar{\boldsymbol{\mathcal{U}}}) \delta\boldsymbol{\mathcal{U}}. \tag{9}$$

3.1. Polyconvex viscoelasticity and the associated evolution of internal variables

As required by condition (i), and following Theorem 2 from Reference [38], we reformulate the standard strain energy function $\Psi\left(\boldsymbol{F}, \boldsymbol{C}_{v_1}^{-1} \dots \boldsymbol{C}_{v_{n_{\text{M}}}}^{-1}\right)$ (previously introduced in (2)) as a convex multivariable function W

$$\Psi\left(\boldsymbol{F}, \boldsymbol{C}_{v_1}^{-1} \dots \boldsymbol{C}_{v_{n_{\text{M}}}}^{-1}\right) = W(\boldsymbol{\mathcal{X}}_{\mathcal{Y}}), \tag{10}$$

where

$$W(\boldsymbol{\mathcal{X}}_{\mathcal{Y}}) = W_\infty(\boldsymbol{\mathcal{X}}) + \sum_{\alpha=1}^{n_{\text{M}}} W_\alpha(\boldsymbol{\mathcal{X}}, \boldsymbol{\mathcal{Y}}_\alpha); \quad \boldsymbol{\mathcal{X}}_{\mathcal{Y}} = \{\boldsymbol{\mathcal{X}}, \boldsymbol{\mathcal{Y}}\}; \quad \boldsymbol{\mathcal{Y}} = \{\boldsymbol{\mathcal{Y}}_1, \boldsymbol{\mathcal{Y}}_2, \dots \boldsymbol{\mathcal{Y}}_{n_{\text{M}}}\}. \tag{11}$$

Here, $\boldsymbol{\mathcal{X}} = \{\boldsymbol{F}, \boldsymbol{H}, J\}$ represents the triplet of deformation measures, where $\boldsymbol{F}$ is the deformation gradient tensor (or fibre map), $\boldsymbol{H}$ is its cofactor (area map) defined as $\boldsymbol{H} = \frac{1}{2}\boldsymbol{F} \times \boldsymbol{F}$, and $J = \frac{1}{3}\boldsymbol{H} : \boldsymbol{F}$ is the Jacobian (or volume map). In above definition of $\boldsymbol{H}$, the symbol $\times$ denotes the cross product between second order tensors [39]. The internal state variables associated with each Maxwell viscoelastic branch α are grouped as

$$\boldsymbol{\mathcal{Y}}_\alpha = \{\boldsymbol{Y}_\alpha, y_\alpha\}; \qquad \boldsymbol{Y}_\alpha = \boldsymbol{C}_{v_\alpha}; \qquad y_\alpha = \det\left(\boldsymbol{C}_{v_\alpha}^{-1}\right). \tag{12}$$

The function W is jointly convex in both the deformation triplet measures $\boldsymbol{\mathcal{X}}$ and the internal variables $\boldsymbol{\mathcal{Y}}$. Thermodynamic equilibrium requires that both W_α and its derivatives (e.g., the thermodynamic conjugate stresses with respect to the deformation measures and internal variables) vanish. This condition is satisfied when $\boldsymbol{Y}_\alpha = \boldsymbol{C}$ and $y_\alpha = J^{-2}$.

[4] In computational mechanics, hyperbolicity is commonly assessed by linearising (or perturbing) a nonlinear system of conservation laws about a given state to analyse local wave propagation (e.g., wave speeds and their directions). This should not be confused with a linear hyperbolic system. Linearisation around a given state does not imply that the system is a linear hyperbolic system with constant wave speeds. It indeed examines the local behaviour of a nonlinear system using a tangent (linear) approximation at that state, similar to the Newton-Raphson linearisation of a nonlinear equation.

Given the polyconvex strain energy W (11), we first define the conjugate stresses associated with the deformation measures $\boldsymbol{\mathcal{X}}$ as $\boldsymbol{\Sigma}_{\square} = \frac{\partial W}{\partial \square}$, where $\square = \{\boldsymbol{F}, \boldsymbol{H}, J\}$. The first Piola-Kirchhoff stress tensor $\boldsymbol{P}$ is then obtained by taking time derivative of W (11) whilst holding the internal variables $\boldsymbol{\mathcal{Y}}$ fixed, which gives [10]

$$\boldsymbol{P} : \left.\frac{\partial \boldsymbol{F}}{\partial t}\right|_{\boldsymbol{\mathcal{Y}}} = \left.\frac{dW}{dt}\right|_{\boldsymbol{\mathcal{Y}}} = \left(\boldsymbol{\Sigma}_{\boldsymbol{F}} + \boldsymbol{\Sigma}_{\boldsymbol{H}} \times \boldsymbol{F} + \Sigma_J \boldsymbol{H}\right) : \left.\frac{\partial \boldsymbol{F}}{\partial t}\right|_{\boldsymbol{\mathcal{Y}}}, \tag{13}$$

where $[\bullet]\big|_{\square}$ indicates that $\square$ is held fixed during differentiation. Comparing both sides gives the following expression for the first Piola-Kirchhoff stress as

$$\boldsymbol{P} = \boldsymbol{\Sigma}_{\boldsymbol{F}} + \boldsymbol{\Sigma}_{\boldsymbol{H}} \times \boldsymbol{F} + \Sigma_J \boldsymbol{H}. \tag{14}$$

The symbol $\times$ denotes the tensor cross product between vectors and/or second order tensors as defined in [26,33,39,40]. Utilising expression (11), each conjugate stress comprises two components, namely a long-term equilibrium part and a viscous part. These are expressed as

$$\boldsymbol{\Sigma}_{\square}(\boldsymbol{\mathcal{X}}\boldsymbol{\mathcal{Y}}) = \boldsymbol{\Sigma}^{\infty}_{\square}(\boldsymbol{\mathcal{X}}) + \sum_{\alpha=1}^{n_{\mathrm{M}}} \boldsymbol{\Sigma}^{\alpha}_{\square}(\boldsymbol{\mathcal{X}}, \boldsymbol{\mathcal{Y}}_{\alpha}); \qquad \boldsymbol{\Sigma}^{\infty}_{\square} = \frac{\partial W_{\infty}}{\partial \square}; \qquad \boldsymbol{\Sigma}^{\alpha}_{\square} = \frac{\partial W_{\alpha}}{\partial \square}; \qquad \square = \{\boldsymbol{F}, \boldsymbol{H}, J\}. \tag{15}$$

To fully define the path-dependent viscoelastic model, it is necessary to establish the evolution equations for the internal variables, represented by the viscous strain tensors $\boldsymbol{\mathcal{Y}}$. These equations are derived by considering the dissipation inequality, which ensures that the negative time derivative of the strain energy under constant deformation measures $\boldsymbol{\mathcal{X}}$ is non-negative. Mathematically, this condition is expressed as

$$0 \leq \dot{\mathcal{D}}_{\mathrm{int}} = -\left.\frac{dW}{dt}\right|_{\boldsymbol{\mathcal{X}}} = -\left(\sum_{\alpha=1}^{n_{\mathrm{M}}} \boldsymbol{\Sigma}_{\boldsymbol{Y}_{\alpha}} : \left.\frac{d\boldsymbol{Y}_{\alpha}}{dt}\right|_{\boldsymbol{\mathcal{X}}} + \sum_{\alpha=1}^{n_{\mathrm{M}}} \Sigma_{y_{\alpha}} \left.\frac{dy_{\alpha}}{\partial t}\right|_{\boldsymbol{\mathcal{X}}}\right), \tag{16}$$

where the thermodynamic stresses conjugate to the internal variables are $\boldsymbol{\Sigma}_{\square} = \frac{\partial W_{\alpha}(\boldsymbol{\mathcal{X}}, \boldsymbol{\mathcal{Y}}_{\alpha})}{\partial \square}$, where $\square = \{\boldsymbol{Y}_{\alpha}, y_{\alpha}\}$.

The inequality $\dot{\mathcal{D}}_{\mathrm{int}} \geq 0$ represents the internal dissipation of the viscous material, which is inherently irreversible. To ensure this inequality (16) is met, appropriate evolution equations must be provided for the internal variables $\boldsymbol{\mathcal{Y}}$, depending on the chosen viscoelastic model. These formulations will be discussed in Section 3.1.1.

The Hessian operator $[\mathbb{H}_W]$ of the convex strain energy functional W is defined as the matrix of second derivatives of W with respect to $\boldsymbol{\mathcal{X}}_{\boldsymbol{\mathcal{Y}}}$. It can be expressed in an additive form as

$$[\mathbb{H}_W] = [\mathbb{H}^{\infty}_W] + \sum_{\alpha=1}^{n_{\mathrm{M}}} [\mathbb{H}^{\alpha}_W]. \tag{17}$$

Condition (ii) requires that the Hessian operator to be symmetric and positive definite. The symmetry of $[\mathbb{H}_W]$ follows directly from the convexity of the polyconvex function W, which ensures that the mixed second derivatives are equal. The components of the symmetric Hessian operators $[\mathbb{H}_W]$, $[\mathbb{H}^{\infty}_W]$, and $[\mathbb{H}^{\alpha}_W]$ are defined as

$$[\mathbb{H}^{\square}_W] = \left[\begin{array}{c|c} \mathbb{H}^{\square}_{\boldsymbol{\mathcal{X}}\boldsymbol{\mathcal{X}}} & \mathbb{H}^{\square}_{\boldsymbol{\mathcal{X}}\boldsymbol{\mathcal{Y}}_{\alpha}} \\ \hline \mathbb{H}^{\square}_{\boldsymbol{\mathcal{Y}}_{\alpha}\boldsymbol{\mathcal{X}}} & \mathbb{H}^{\square}_{\boldsymbol{\mathcal{Y}}_{\alpha}\boldsymbol{\mathcal{Y}}_{\alpha}} \end{array}\right] = \left[\begin{array}{ccc|cc} W^{\square}_{\boldsymbol{FF}} & W^{\square}_{\boldsymbol{FH}} & W^{\square}_{\boldsymbol{FJ}} & W^{\square}_{\boldsymbol{FY}_{\alpha}} & W^{\square}_{\boldsymbol{F}y_{\alpha}} \\ W^{\square}_{\boldsymbol{HF}} & W^{\square}_{\boldsymbol{HH}} & W^{\square}_{\boldsymbol{HJ}} & W^{\square}_{\boldsymbol{HY}_{\alpha}} & W^{\square}_{\boldsymbol{H}y_{\alpha}} \\ W^{\square}_{\boldsymbol{JF}} & W^{\square}_{\boldsymbol{JH}} & W^{\square}_{\boldsymbol{JJ}} & W^{\square}_{\boldsymbol{JY}_{\alpha}} & W^{\square}_{\boldsymbol{J}y_{\alpha}} \\ \hline W^{\square}_{\boldsymbol{Y}_{\alpha}\boldsymbol{F}} & W^{\square}_{\boldsymbol{Y}_{\alpha}\boldsymbol{H}} & W^{\square}_{\boldsymbol{Y}_{\alpha}\boldsymbol{J}} & W^{\square}_{\boldsymbol{Y}_{\alpha}\boldsymbol{Y}_{\alpha}} & W^{\square}_{\boldsymbol{Y}_{\alpha}y_{\alpha}} \\ W^{\square}_{y_{\alpha}\boldsymbol{F}} & W^{\square}_{y_{\alpha}\boldsymbol{H}} & W^{\square}_{y_{\alpha}\boldsymbol{J}} & W^{\square}_{y_{\alpha}\boldsymbol{Y}_{\alpha}} & W^{\square}_{y_{\alpha}y_{\alpha}} \end{array}\right]. \tag{18}$$

Here, $\square = \{\infty, \alpha\}$. The notation $W_{\boldsymbol{AB}} = \frac{\partial^2 W}{\partial \boldsymbol{A} \partial \boldsymbol{B}}$ indicates second derivatives of W with respect to variables $\boldsymbol{A}, \boldsymbol{B} \in \{\boldsymbol{F}, \boldsymbol{H}, J, \boldsymbol{Y}_{\alpha}, y_{\alpha}\}$.

3.1.1. Mooney-Rivlin-type viscoelasticity

We now consider a specific polyconvex viscoelastic model. Following [33,39,41,42], the long-term equilibrium component W_{∞} is defined using a polyconvex energy function based on the Mooney-Rivlin material as[5]

$$W_{\infty}(\boldsymbol{\mathcal{X}}) = \xi(\boldsymbol{F} : \boldsymbol{F} - 3) + \zeta(\boldsymbol{H} : \boldsymbol{H} - 3) + f(J); \quad f(J) = -2(\xi + 2\zeta)\ln J + \frac{\hat{\lambda}}{2}(J-1)^2. \tag{19}$$

The positive parameters ξ, ζ and $\hat{\lambda}$ satisfy the relations $\xi + \zeta = \frac{\mu}{2}$ and $\lambda = \hat{\lambda} + 4\zeta$, where μ and λ represent the shear modulus and Lamé parameter of the material[6], respectively. Note that setting $\zeta = 0$ recovers the polyconvex neoHookean model. The long-term

[5] For Maxwell viscoelastic fluids [25], the long-term equilibrium strain energy is typically associated only with volumetric changes. Shear response is purely viscous and relaxes over time, contributing to the non-equilibrium (time-dependent) part of the strain energy.

[6] The Lame's constants can be expressed in terms of the Young's modulus E and the Poisson's ratio ν as

$$\lambda = \frac{E\nu}{(1+\nu)(1-2\nu)}; \qquad \mu = \frac{E}{2(1+\nu)}.$$

potential $W_\infty(\boldsymbol{\mathcal{X}})$ is polyconvex in $\boldsymbol{\mathcal{X}}$, since it can be expressed as a convex function of $\boldsymbol{F}$, $\boldsymbol{H}$, and J. In particular, the volumetric contribution $f(J)$ is convex in J when $\{\hat{\lambda}, \xi, \zeta\} \geq 0$.

For isotropic viscoelastic solids, we introduce the non-equilibrium (viscous) energy component $W_\alpha(\boldsymbol{\mathcal{X}}, \boldsymbol{\mathcal{Y}}_\alpha)$ as

$$W_\alpha(\boldsymbol{\mathcal{X}}, \boldsymbol{\mathcal{Y}}_\alpha) = \frac{\mu_\alpha}{2}\left[\boldsymbol{C} : \boldsymbol{Y}_\alpha^{-1} - 3 - \ln\left(J^2 y_\alpha\right)\right], \tag{20}$$

where $\mu_\alpha = \mu\beta_\alpha$. The dimensionless proportionality factor β_α is conveniently introduced to control the magnitude of the viscous effects and must be calibrated from experiments. This form ensures that W_α (20) and its derivatives with respect to both $\boldsymbol{\mathcal{X}}$ and $\boldsymbol{\mathcal{Y}}_\alpha$ vanish at equilibrium (i.e., $W_\alpha = 0$ when $\boldsymbol{Y}_\alpha = \boldsymbol{C}$ and $y_\alpha = J^{-2}$), thus guaranteeing thermodynamic consistency. Furthermore, this non-equilibrium (viscous) potential is designed to be jointly convex in its arguments $\{\boldsymbol{\mathcal{X}}, \boldsymbol{\mathcal{Y}}_\alpha\}$. A detailed proof of polyconvexity is demonstrated in Remark 2. Explicit expressions for the associated thermodynamic conjugate stresses $\boldsymbol{\Sigma}_\square$ (with respect to $\square = \{\boldsymbol{\mathcal{X}}, \boldsymbol{\mathcal{Y}}_\alpha\}$), as well as the Hessian operators $[\mathbb{H}_W]$, are derived and presented in A.

Remark 2. The first directional derivative of the strain energy W_α with respect to perturbations $\{\delta\boldsymbol{\mathcal{X}}, \delta\boldsymbol{\mathcal{Y}}_\alpha\}$ is given by

$$DW_\alpha[\delta\boldsymbol{\mathcal{X}}, \delta\boldsymbol{\mathcal{Y}}_\alpha] = \frac{\mu_\alpha}{2}\left[\mathrm{tr}\left(\delta\boldsymbol{F}\boldsymbol{Y}_\alpha^{-1}\boldsymbol{F}^T + \boldsymbol{F}\boldsymbol{Y}_\alpha^{-1}\delta\boldsymbol{F}^T + \boldsymbol{F}\delta\boldsymbol{Y}_\alpha^{-1}\boldsymbol{F}^T\right) - 2J^{-1}\delta J - y_\alpha^{-1}\delta y_\alpha\right]. \tag{21}$$

Here, $\delta\boldsymbol{Y}_\alpha^{-1} = D\boldsymbol{Y}_\alpha^{-1}[\delta\boldsymbol{Y}_\alpha] = -\boldsymbol{Y}_\alpha^{-1}\delta\boldsymbol{Y}_\alpha\boldsymbol{Y}_\alpha^{-1}$ denotes the directional derivative of $\boldsymbol{Y}_\alpha^{-1}$ in the direction of $\delta\boldsymbol{Y}_\alpha$. Utilising the property $\mathrm{tr}(\boldsymbol{A}\boldsymbol{B}^T) = \mathrm{tr}(\boldsymbol{B}\boldsymbol{A}^T)$, expression (21) simplifies to

$$DW_\alpha[\delta\boldsymbol{\mathcal{X}}, \delta\boldsymbol{\mathcal{Y}}_\alpha] = \frac{\mu_\alpha}{2}\left[\mathrm{tr}\left(2\delta\boldsymbol{F}\boldsymbol{K}^T - \boldsymbol{K}\delta\boldsymbol{Y}_\alpha\boldsymbol{K}^T\right) - 2J^{-1}\delta J - y_\alpha^{-1}\delta y_\alpha\right]; \quad \boldsymbol{K} = \boldsymbol{F}\boldsymbol{Y}_\alpha^{-1}. \tag{22}$$

Taking the second directional derivative yields

$$D^2W_\alpha[\delta\boldsymbol{\mathcal{X}}, \delta\boldsymbol{\mathcal{Y}}_\alpha] = \mu_\alpha\left[\mathrm{tr}\left(\delta\boldsymbol{F}\delta\boldsymbol{K}^T - \delta\boldsymbol{K}\delta\boldsymbol{Y}_\alpha\boldsymbol{K}^T\right) + J^{-2}(\delta J)^2 + \frac{1}{2}y_\alpha^{-2}(\delta y_\alpha)^2\right]. \tag{23}$$

Since the terms involving $(\delta J)^2$ and $(\delta y_\alpha)^2$ are non-negative, the positivity of D^2W_α (23) depends on the sign of the trace terms. To achieve this, note that $\delta\boldsymbol{K} = D\boldsymbol{K}[\delta\boldsymbol{F}, \delta\boldsymbol{Y}_\alpha] = D\boldsymbol{F}\boldsymbol{Y}_\alpha^{-1}[\delta\boldsymbol{F}, \delta\boldsymbol{Y}_\alpha] = \delta\boldsymbol{F}\boldsymbol{Y}_\alpha^{-1} - \boldsymbol{F}\boldsymbol{Y}_\alpha^{-1}\delta\boldsymbol{Y}_\alpha\boldsymbol{Y}_\alpha^{-1}$. Substituting this back into the trace expression, we obtain

$$\begin{aligned}\mathrm{tr}\left(\delta\boldsymbol{F}\delta\boldsymbol{K}^T - \delta\boldsymbol{K}\delta\boldsymbol{Y}_\alpha\boldsymbol{K}^T\right) &= \mathrm{tr}\left[\delta\boldsymbol{F}\boldsymbol{Y}_\alpha^{-1}\delta\boldsymbol{F}^T - 2\delta\boldsymbol{F}\boldsymbol{Y}_\alpha^{-1}\delta\boldsymbol{Y}_\alpha\boldsymbol{K}^T + \boldsymbol{K}\delta\boldsymbol{Y}_\alpha\boldsymbol{Y}_\alpha^{-1}\delta\boldsymbol{Y}_\alpha\boldsymbol{K}^T\right] \\ &= \left(\delta\boldsymbol{F}\boldsymbol{Y}_\alpha^{-1/2} - \boldsymbol{K}\delta\boldsymbol{Y}_\alpha\boldsymbol{Y}_\alpha^{-1/2}\right) : \left(\delta\boldsymbol{F}\boldsymbol{Y}_\alpha^{-1/2} - \boldsymbol{K}\delta\boldsymbol{Y}_\alpha\boldsymbol{Y}_\alpha^{-1/2}\right) \geq 0.\end{aligned} \tag{24}$$

Consequently, the second directional derivative D^2W_α is non-negative for all admissible perturbations, confirming the polyconvexity of W_α.

To close the system and ensure thermodynamic consistency, it is necessary to introduce appropriate evolution laws for the internal variables $\boldsymbol{Y}_\alpha$ and y_α that satisfy the second law of thermodynamics. In accordance with the dissipation inequality (16), we propose the following extended set of evolution equations, which generalises the formulation presented in [25] by additionally incorporating the evolution of y_α, to give

$$\left.\frac{d\boldsymbol{Y}_\alpha}{dt}\right|_{\boldsymbol{\mathcal{X}}} = \underbrace{\frac{1}{\tau_\alpha}\left(\boldsymbol{Y}_\alpha - \boldsymbol{Y}_\alpha\boldsymbol{C}^{-1}\boldsymbol{Y}_\alpha\right)}_{\mathcal{R}_{\boldsymbol{Y}_\alpha}}; \qquad \left.\frac{dy_\alpha}{dt}\right|_{\boldsymbol{\mathcal{X}}} = \underbrace{\frac{1}{\tau_\alpha}y_\alpha\left(\boldsymbol{C}^{-1} : \boldsymbol{Y}_\alpha - 3\right)}_{\mathcal{R}_{y_\alpha}}. \tag{25}$$

These evolution laws guarantee non-negative internal dissipation, as demonstrated in Remark 3. When $\boldsymbol{Y}_\alpha$ equals $\boldsymbol{C}$, the system reaches an elastic equilibrium, with both $\boldsymbol{Y}_\alpha$ and y_α remaining constant in time. Using the identity $\left.\frac{\partial\boldsymbol{Y}_\alpha^{-1}}{dt}\right|_{\boldsymbol{\mathcal{X}}} = -\boldsymbol{Y}_\alpha^{-1}\left.\frac{d\boldsymbol{Y}_\alpha}{dt}\right|_{\boldsymbol{\mathcal{X}}}\boldsymbol{Y}_\alpha^{-1}$, the evolution law for $\boldsymbol{Y}_\alpha$ can equivalently be expressed in terms of its inverse as

$$\left.\frac{d\boldsymbol{Y}_\alpha^{-1}}{dt}\right|_{\boldsymbol{\mathcal{X}}} = \frac{1}{\tau_\alpha}\left(\boldsymbol{C}^{-1} - \boldsymbol{Y}_\alpha^{-1}\right). \tag{26}$$

This is a linear, first-order, non-homogeneous ordinary differential equation for $\boldsymbol{Y}_\alpha^{-1}$, which admits an exact closed-form solution in time. Details can be found in Section 6.

Remark 3. To demonstrate that the dissipation inequality $\dot{\mathcal{D}}_{\mathrm{int}} \geq 0$ is satisfied, we first recall expression (16), which has been generalised from Linder *et al.*[43] to account for the extended set of internal variables and is reproduced here for convenience

$$\dot{\mathcal{D}}_{\mathrm{int}} = -\left(\sum_{\alpha=1}^{n_{\mathrm{M}}}\boldsymbol{\Sigma}_{\boldsymbol{Y}_\alpha} : \left.\frac{d\boldsymbol{Y}_\alpha}{dt}\right|_{\boldsymbol{\mathcal{X}}} + \sum_{\alpha=1}^{n_{\mathrm{M}}}\Sigma_{y_\alpha}\left.\frac{dy_\alpha}{\partial t}\right|_{\boldsymbol{\mathcal{X}}}\right). \tag{27}$$

Using the thermodynamic conjugate stresses $\boldsymbol{\Sigma}_{\boldsymbol{Y}_\alpha}$ and Σ_{y_α} from (A.2) together with the evolution Eqs. (25) for $\boldsymbol{Y}_\alpha$ and y_α, we can combine terms to show that

$$\dot{\mathcal{D}}_{\mathrm{int}} = \sum_{\alpha=1}^{n_{\mathrm{M}}}\frac{\mu_\alpha}{2\tau_\alpha}\left[\boldsymbol{Y}_\alpha^{-1}\boldsymbol{C}\boldsymbol{Y}_\alpha^{-1} : \left(\boldsymbol{Y}_\alpha - \boldsymbol{Y}_\alpha\boldsymbol{C}^{-1}\boldsymbol{Y}_\alpha\right) + \boldsymbol{C}^{-1} : \boldsymbol{Y}_\alpha - 3\right] = \sum_{\alpha=1}^{n_{\mathrm{M}}}\frac{\mu_\alpha}{2\tau_\alpha}\mathrm{tr}\left[\boldsymbol{C}\boldsymbol{Y}_\alpha^{-1} + \boldsymbol{C}^{-1}\boldsymbol{Y}_\alpha - 2\boldsymbol{I}\right]. \tag{28}$$

Noting that $\mathrm{tr}\big(\boldsymbol{C}\boldsymbol{Y}_\alpha^{-1}\big) = \mathrm{tr}\Big(\boldsymbol{Y}_\alpha^{-1/2}\boldsymbol{C}\boldsymbol{Y}_\alpha^{-1/2}\Big)$ and similarly $\mathrm{tr}(\boldsymbol{C}^{-1}\boldsymbol{Y}_\alpha) = \mathrm{tr}(\boldsymbol{Y}_\alpha^{1/2}\boldsymbol{C}^{-1}\boldsymbol{Y}_\alpha^{1/2})$, we introduce $\boldsymbol{M} = \boldsymbol{Y}_\alpha^{-1/2}\boldsymbol{C}\boldsymbol{Y}_\alpha^{-1/2}$ so that the above expression simplifies to

$$\dot{\mathcal{D}}_{\mathrm{int}} = \sum_{\alpha=1}^{n_{\mathrm{M}}} \frac{\mu_\alpha}{2\tau_\alpha}\mathrm{tr}\big[\boldsymbol{M} + \boldsymbol{M}^{-1} - 2\boldsymbol{I}\big]. \tag{29}$$

Since $\boldsymbol{M}$ is a symmetric positive definite tensor, consider its spectral decomposition and its inverse in the form

$$\boldsymbol{M} = \sum_{I=1}^{3} \lambda_I \boldsymbol{N}_I \otimes \boldsymbol{N}_I; \qquad \boldsymbol{M}^{-1} = \sum_{I=1}^{3} \lambda_I^{-1} \boldsymbol{N}_I \otimes \boldsymbol{N}_I, \tag{30}$$

where $\lambda_I > 0$ are positive eigenvalues and $\boldsymbol{N}_I$ are the corresponding normalised eigenvectors. Consequently,

$$\dot{\mathcal{D}}_{\mathrm{int}} = \sum_{\alpha=1}^{n_{\mathrm{M}}} \left[\frac{\mu_\alpha}{2\tau_\alpha}\sum_{I=1}^{3}\big(\lambda_I + \lambda_I^{-1} - 2\big)\right] \geq 0, \tag{31}$$

using the inequality $\lambda_I + \lambda_I^{-1} \geq 2$.

3.1.2. Complete first-order hyperbolic system

To express the governing system in first-order hyperbolic form for polyconvex viscoelasticity, we combine the linear momentum conservation Eq. (1), the evolution equations for the internal variables (25) associated with each Maxwell branch α, and the geometric conservation laws for the triplet of deformation measures $\boldsymbol{\mathcal{X}}$[7]. The components of the conservation unknowns $\boldsymbol{\mathcal{U}}$, fluxes $\boldsymbol{\mathcal{F}}_I$, external source term $\boldsymbol{\mathcal{S}}_{\mathrm{ext}}$, and the relaxation term $\boldsymbol{\mathcal{R}}$ in the resulting first-order hyperbolic system with relaxation can then be written as

$$\boldsymbol{\mathcal{U}} = \begin{bmatrix} \boldsymbol{p}_R \\ \boldsymbol{F} \\ \boldsymbol{H} \\ J \\ \boldsymbol{Y}_1 \\ y_1 \\ \vdots \\ \boldsymbol{Y}_{n_{\mathrm{M}}} \\ y_{n_{\mathrm{M}}} \end{bmatrix}; \quad \boldsymbol{\mathcal{F}}_I = -\begin{bmatrix} \boldsymbol{P}\boldsymbol{E}_I \\ \boldsymbol{v}\otimes\boldsymbol{E}_I \\ \boldsymbol{F}\times(\boldsymbol{v}\otimes\boldsymbol{E}_I) \\ \boldsymbol{H}:(\boldsymbol{v}\otimes\boldsymbol{E}_I) \\ \boldsymbol{0} \\ 0 \\ \vdots \\ \boldsymbol{0} \\ 0 \end{bmatrix}; \quad \boldsymbol{\mathcal{S}}_{\mathrm{ext}} = \begin{bmatrix} \boldsymbol{f}_R \\ \boldsymbol{0} \\ \boldsymbol{0} \\ 0 \\ \boldsymbol{0} \\ 0 \\ \vdots \\ \boldsymbol{0} \\ 0 \end{bmatrix}; \quad \boldsymbol{\mathcal{R}} = \begin{bmatrix} \boldsymbol{0} \\ \boldsymbol{0} \\ \boldsymbol{0} \\ 0 \\ \boldsymbol{\mathcal{R}}_{\boldsymbol{Y}_1} \\ \mathcal{R}_{y_1} \\ \vdots \\ \boldsymbol{\mathcal{R}}_{\boldsymbol{Y}_{n_{\mathrm{M}}}} \\ \mathcal{R}_{y_{n_{\mathrm{M}}}} \end{bmatrix}, \tag{32}$$

where $\boldsymbol{E}_I$ are the Cartesian unit vectors. The geometric conservation laws for $\boldsymbol{\mathcal{X}}$ are included to ensure that the system of conservation laws (7) can be symmetrised. The evolution equations for the internal variables are purely local and do not contain spatial flux terms. Finally, the flux vector in the direction of an arbitrary material unit normal $\boldsymbol{N}$ is given by $\boldsymbol{\mathcal{F}}_{\boldsymbol{N}} = \sum_{I=1}^{3}\boldsymbol{\mathcal{F}}_I N_I$. Note that $\sum_{\alpha=1}^{n_{\mathrm{M}}} -\boldsymbol{\mathcal{V}}^T\boldsymbol{\mathcal{R}}_\alpha = \dot{\mathcal{D}}_{\mathrm{int}} \geq 0$, as required by condition (iv) defined in Section 3.

For smooth solutions, the conservation laws for $\boldsymbol{F}$ and $\boldsymbol{H}$ must satisfy the so-called involutions (or compatibility conditions) described by [5,45–51]

$$\mathrm{CURL}\boldsymbol{F} = \boldsymbol{0}; \quad \mathrm{DIV}\boldsymbol{H} = \boldsymbol{0}. \tag{33}$$

The curl-free condition on $\boldsymbol{F}$ ensures it is compatible with a deformation mapping (i.e., that it is a gradient field), whilst the divergence-free condition on $\boldsymbol{H}$ enforces the Piola identity, ensuring consistency between $\boldsymbol{F}$ and its Jacobian J.

In general, the system can only be written in symmetric hyperbolic form (in terms of conjugate stress variables) if it includes the full set of unknowns $\{\boldsymbol{p}_R, \boldsymbol{\mathcal{X}}, \boldsymbol{\mathcal{Y}}_\alpha\}$. However, for computational efficiency and to reduce the amount of experimental calibration required for the internal variables, it may be useful to consider reduced systems that include only $\boldsymbol{p}_R$, $\boldsymbol{\mathcal{X}}$, and $\boldsymbol{C}_{v_\alpha}$ (or $\boldsymbol{C}_{v_\alpha}^{-1}$).

For post-processing purposes, the current geometry $\boldsymbol{\phi}$ can be updated via

$$\frac{\partial\boldsymbol{\phi}(\boldsymbol{X},t)}{\partial t} = \boldsymbol{v}(\boldsymbol{X},t). \tag{34}$$

3.2. Symmetric hyperbolic system

Symmetrisation is crucial to ensure that a first-order hyperbolic system is mathematically well-posed. Specifically, symmetric hyperbolic systems have real eigenvalues and a complete set of eigenvectors, which correspond to physical wave speeds and propagation directions. To achieve symmetrisation, we introduce a strictly convex scalar function, referred to as a generalised entropy $S(\boldsymbol{X},t)$. The strict convexity ensures that its Hessian matrix is positive-definite, which provides a one-to-one mapping between the conservation variables and the corresponding conjugate variables. Intuitively, the generalised entropy provides a measure of the energy-like behaviour within a system, allowing derivation of stability estimates [32,34].

[7] The derivation of the associated geometric conservation equations for $\boldsymbol{F}$, $\boldsymbol{H}$, and J was presented in Reference [33] and is summarised here for completeness [44] :

$$\frac{\partial\boldsymbol{F}}{\partial t} = \boldsymbol{\nabla}_0\boldsymbol{v}; \qquad \frac{\partial\boldsymbol{H}}{\partial t} = \mathrm{CURL}(\boldsymbol{v}\times\boldsymbol{F}); \qquad \frac{\partial J}{\partial t} = \mathrm{DIV}\big(\boldsymbol{H}^T\boldsymbol{v}\big).$$

In our context, the convex entropy function is defined as

$$S(\boldsymbol{X},t) = \frac{1}{2\rho_R}\boldsymbol{p}_R \cdot \boldsymbol{p}_R + W(\mathcal{X}_{\mathcal{Y}}). \tag{35}$$

The first term represents the kinetic energy per unit undeformed volume and the second term corresponds to the polyconvex strain energy density per unit undeformed volume. The associated conjugate variables[8] $\mathcal{V}$ are then given by

$$\mathcal{V} = \frac{\partial S}{\partial \mathcal{U}} = \begin{bmatrix} \frac{\partial S}{\partial \boldsymbol{p}_R} \\ \frac{\partial S}{\partial \boldsymbol{F}} \\ \frac{\partial S}{\partial \boldsymbol{H}} \\ \frac{\partial S}{\partial J} \\ \frac{\partial S}{\partial \boldsymbol{Y}_1} \\ \frac{\partial S}{\partial y_1} \\ \vdots \\ \frac{\partial S}{\partial \boldsymbol{Y}_{n_{\mathrm{M}}}} \\ \frac{\partial S}{\partial y_{n_{\mathrm{M}}}} \end{bmatrix} = \begin{bmatrix} \boldsymbol{v} \\ \frac{\partial W(\mathcal{X}_{\mathcal{Y}})}{\partial \boldsymbol{F}} \\ \frac{\partial W(\mathcal{X}_{\mathcal{Y}})}{\partial \boldsymbol{H}} \\ \frac{\partial W(\mathcal{X}_{\mathcal{Y}})}{\partial J} \\ \frac{\partial W(\mathcal{X}_{\mathcal{Y}})}{\partial \boldsymbol{Y}_1} \\ \frac{\partial W(\mathcal{X}_{\mathcal{Y}})}{\partial y_1} \\ \vdots \\ \frac{\partial W(\mathcal{X}_{\mathcal{Y}})}{\partial \boldsymbol{Y}_{n_{\mathrm{M}}}} \\ \frac{\partial W(\mathcal{X}_{\mathcal{Y}})}{\partial y_{n_{\mathrm{M}}}} \end{bmatrix} = \begin{bmatrix} \boldsymbol{v} \\ \boldsymbol{\Sigma}_{\boldsymbol{F}} \\ \boldsymbol{\Sigma}_{\boldsymbol{H}} \\ \Sigma_J \\ \boldsymbol{\Sigma}_{\boldsymbol{Y}_1} \\ \Sigma_{y_1} \\ \vdots \\ \boldsymbol{\Sigma}_{\boldsymbol{Y}_{n_{\mathrm{M}}}} \\ \Sigma_{y_{n_{\mathrm{M}}}} \end{bmatrix}. \tag{36}$$

Consider the following notation

$$\mathcal{A}_0 = \frac{\partial \mathcal{U}}{\partial \mathcal{V}}; \qquad \mathcal{A}_I = \frac{\partial \mathcal{F}_I}{\partial \mathcal{U}}; \qquad \tilde{\mathcal{A}}_I = \mathcal{A}_I \mathcal{A}_0. \tag{37}$$

Applying the chain rule to the time derivtive of the conservation variables and the spatial derivatives of the fluxes yields

$$\frac{\partial \mathcal{U}}{\partial t} = \mathcal{A}_0 \frac{\partial \mathcal{V}}{\partial t}; \qquad \frac{\partial \mathcal{F}_I}{\partial X_I} = \tilde{\mathcal{A}}_I \frac{\partial \mathcal{V}}{\partial X_I}. \tag{38}$$

Substituting these expressions into the hyperbolic system (7), the resulting equations in terms of the entropy conjugate variables are

$$\mathcal{A}_0 \frac{\partial \mathcal{V}}{\partial t} + \sum_{I=1}^{3} \tilde{\mathcal{A}}_I \frac{\partial \mathcal{V}}{\partial X_I} = \mathcal{S}. \tag{39}$$

Here,

- $\mathcal{A}_0 = \left[\frac{\partial^2 S}{\partial \mathcal{U} \partial \mathcal{U}}\right]^{-1} = \begin{bmatrix} \rho_R \boldsymbol{I} & \boldsymbol{0} \\ \boldsymbol{0} & [\mathbb{H}_W]^{-1} \end{bmatrix}$, a symmetric positive-definite matrix.
- The matrices $\tilde{\mathcal{A}}_I$ are symmetric flux Jacobian matrices satisfying condition (iii) (refer to Section 3).

Particularising the general framework to the system under consideration and accounting for the involutions (33), the symmetric structure of the system becomes clearer in indicial notation, which can be expressed as[9]

$$\left[\mathcal{A}_0\right] \frac{\partial}{\partial t} \begin{bmatrix} v_j \\ \left[\boldsymbol{\Sigma}_{\boldsymbol{F}}\right]_{lL} \\ \left[\boldsymbol{\Sigma}_{\boldsymbol{H}}\right]_{lL} \\ \Sigma_J \\ \left[\boldsymbol{\Sigma}_{\boldsymbol{Y}_1}\right]_{NO} \\ \Sigma_{y_1} \\ \vdots \\ \left[\boldsymbol{\Sigma}_{\boldsymbol{Y}_{n_{\mathrm{M}}}}\right]_{NO} \\ \Sigma_{y_{n_{\mathrm{M}}}} \end{bmatrix} - \left[\tilde{\mathcal{A}}_I\right] \frac{\partial}{\partial X_I} \begin{bmatrix} v_k \\ \left[\boldsymbol{\Sigma}_{\boldsymbol{F}}\right]_{kK} \\ \left[\boldsymbol{\Sigma}_{\boldsymbol{H}}\right]_{kK} \\ \Sigma_J \\ \left[\boldsymbol{\Sigma}_{\boldsymbol{Y}_1}\right]_{NO} \\ \Sigma_{y_1} \\ \vdots \\ \left[\boldsymbol{\Sigma}_{\boldsymbol{Y}_{n_{\mathrm{M}}}}\right]_{NO} \\ \Sigma_{y_{n_{\mathrm{M}}}} \end{bmatrix} = \begin{bmatrix} \left[\boldsymbol{f}_R\right]_i \\ \boldsymbol{0} \\ \boldsymbol{0} \\ 0 \\ \left[\boldsymbol{\mathcal{R}}_{\boldsymbol{Y}_1}\right]_{KM} \\ \mathcal{R}_{y_1} \\ \vdots \\ \left[\boldsymbol{\mathcal{R}}_{\boldsymbol{Y}_{n_{\mathrm{M}}}}\right]_{KM} \\ \mathcal{R}_{y_{n_{\mathrm{M}}}} \end{bmatrix}. \tag{40}$$

[8] Entropy conjugate variables $\mathcal{V}$ are the thermodynamic forces associated with the conserved variables $\mathcal{U}$, representing the driving forces that govern their evolution.

[9] Pre-multiplying system (40) by $\mathcal{A}_0^{-1}$ yields an extended hydrocode formulation, expressed in terms of velocity and entropy-conjugate variables [33]. Note however that this hydrocode formulation is no longer symmetric.

The symmetric flux Jacobian matrix $\tilde{\mathcal{A}}_I$ is given explicitly as

$$\left[\tilde{\mathcal{A}}_I\right] = \begin{bmatrix} \mathbf{0} & \delta_{ik}\delta_{KI} & \mathcal{E}_{ijk}\mathcal{E}_{IJK}F_{jJ} & H_{iI} & \mathbf{0} & \mathbf{0} & \cdots & \mathbf{0} & \mathbf{0} \\ \delta_{ik}\delta_{JI} & \mathbf{0} & \mathbf{0} & \mathbf{0} & \mathbf{0} & \mathbf{0} & \cdots & \mathbf{0} & \mathbf{0} \\ \mathcal{E}_{ijk}\mathcal{E}_{JKI}F_{jK} & \mathbf{0} & \mathbf{0} & \mathbf{0} & \mathbf{0} & \mathbf{0} & \cdots & \mathbf{0} & \mathbf{0} \\ H_{kI} & \mathbf{0} & \mathbf{0} & 0 & \mathbf{0} & 0 & \cdots & \mathbf{0} & \mathbf{0} \\ \mathbf{0} & \mathbf{0} & \mathbf{0} & \mathbf{0} & \mathbf{0} & \mathbf{0} & \cdots & \mathbf{0} & \mathbf{0} \\ \mathbf{0} & \mathbf{0} & \mathbf{0} & 0 & \mathbf{0} & 0 & \cdots & \mathbf{0} & \mathbf{0} \\ \vdots & \vdots & \vdots & \vdots & \vdots & \vdots & \ddots & \vdots & \vdots \\ \mathbf{0} & \mathbf{0} & \mathbf{0} & \mathbf{0} & \mathbf{0} & \mathbf{0} & \cdots & \mathbf{0} & \mathbf{0} \\ \mathbf{0} & \mathbf{0} & \mathbf{0} & 0 & \mathbf{0} & 0 & \cdots & \mathbf{0} & \mathbf{0} \end{bmatrix}. \tag{41}$$

4. Hyperbolicity and relaxation

To examine the hyperbolicity and dissipative properties of the system, we consider plane wave solutions to the linearised Eqs. (9) of the form

$$\delta\boldsymbol{\mathcal{U}}(\boldsymbol{X},t) = \mathrm{Re}\left[\boldsymbol{\mathcal{U}}_j e^{\mathrm{i}k_j(\boldsymbol{X}\cdot\boldsymbol{N}-c_j t)}\right], \tag{42}$$

where k_j is a positive real wave number, $\boldsymbol{\mathcal{U}}_j$ is a complex vector of unknowns, c_j is a generally complex wave speed, and $\boldsymbol{N}$ is a unit vector in the direction of wave propagation. The operator Re[•] ensures that the perturbation field $\delta\boldsymbol{\mathcal{U}}(\boldsymbol{X},t)$ remains real-valued, as required for physical solutions. The wave speed c_j can be decomposed as $c_j = c_j^R + \mathrm{i}c_j^I$ with real and imaginary parts. Substituting this decomposition into expression (42) yields

$$\delta\boldsymbol{\mathcal{U}}(\boldsymbol{X},t) = \mathrm{Re}\left[\left(\boldsymbol{\mathcal{U}}_j e^{k_j c_j^I t}\right) e^{\mathrm{i}k_j(\boldsymbol{X}\cdot\boldsymbol{N}-c_j^R t)}\right]. \tag{43}$$

This describes a wave propagating at speed c_j^R, with amplitude that grows or decays in time depending on the sign of c_j^I. For stability, we require $c_j^I \leq 0$ so that perturbations decay exponentially over time.

Taking derivatives of (42) with respect to time and space gives

$$\frac{\partial\delta\boldsymbol{\mathcal{U}}}{\partial t} = \mathrm{Re}\left[-c_j\mathrm{i}k_j e^{\mathrm{i}k_j(\boldsymbol{X}\cdot\boldsymbol{N}-c_j t)}\boldsymbol{\mathcal{U}}_j\right]; \qquad \frac{\partial\delta\boldsymbol{\mathcal{U}}}{\partial X_I} = \mathrm{Re}\left[\mathrm{i}k_j e^{\mathrm{i}k_j(\boldsymbol{X}\cdot\boldsymbol{N}-c_j t)}N_I\boldsymbol{\mathcal{U}}_j\right]. \tag{44}$$

Substituting these expressions into the linearised system (9) and cancelling the common exponential terms leads to

$$\mathrm{Re}\left[c_j\boldsymbol{\mathcal{U}}_j\right] = \mathrm{Re}\left[\left(\boldsymbol{\mathcal{A}}_{\boldsymbol{N}} + \frac{\mathrm{i}}{k_j}\boldsymbol{\mathcal{J}}\right)\boldsymbol{\mathcal{U}}_j\right]; \qquad \boldsymbol{\mathcal{A}}_{\boldsymbol{N}} = \sum_{I=1}^{3}\boldsymbol{\mathcal{A}}_I N_I. \tag{45}$$

Decomposing the wave speed and perturbation into real and imaginary parts, such as $c_j = c_j^R + \mathrm{i}c_j^I$ and $\boldsymbol{\mathcal{U}}_j = \boldsymbol{\mathcal{U}}_j^R + \mathrm{i}\boldsymbol{\mathcal{U}}_j^I$, the left-hand side becomes

$$\mathrm{Re}\left[c_j\boldsymbol{\mathcal{U}}_j\right] = c_j^R\boldsymbol{\mathcal{U}}_j^R - c_j^I\boldsymbol{\mathcal{U}}_j^I, \tag{46}$$

and the right-hand side becomes

$$\mathrm{Re}\left[\left(\boldsymbol{\mathcal{A}}_{\boldsymbol{N}} + \frac{\mathrm{i}}{k_j}\boldsymbol{\mathcal{J}}\right)\boldsymbol{\mathcal{U}}_j\right] = \boldsymbol{\mathcal{A}}_{\boldsymbol{N}}\boldsymbol{\mathcal{U}}_j^R - \frac{1}{k_j}\boldsymbol{\mathcal{J}}\boldsymbol{\mathcal{U}}_j^I. \tag{47}$$

Equating both sides leads to the following eigenvalue problem

$$c_j^R\boldsymbol{\mathcal{U}}_j^R - c_j^I\boldsymbol{\mathcal{U}}_j^I = \boldsymbol{\mathcal{A}}_{\boldsymbol{N}}\boldsymbol{\mathcal{U}}_j^R - \frac{1}{k_j}\boldsymbol{\mathcal{J}}\boldsymbol{\mathcal{U}}_j^I. \tag{48}$$

This system couples the real and imaginary parts of both the wave speed and the perturbation vector. Several approaches can be used to analyse this problem. One convenient approach is to decouple the problem by considering two asymptotic regimes, namely

- Purely hyperbolic regime (no relaxation). Setting $\boldsymbol{\mathcal{J}} = \mathbf{0}$ and $\boldsymbol{\mathcal{U}}_j^I = \mathbf{0}$ reduces the problem to

  $$c_j^R\boldsymbol{\mathcal{U}}_j^R = \boldsymbol{\mathcal{A}}_{\boldsymbol{N}}\boldsymbol{\mathcal{U}}_j^R, \tag{49}$$

  which governs the wave propagation properties and reflects the hyperbolicity of the system. Physically, this corresponds to determining wave speeds whilst treating the internal variables as fixed (i.e., without allowing their relaxation dynamics to evolve).
- Purely relaxation regime (vanishing convective flux). Setting $\boldsymbol{\mathcal{A}}_{\boldsymbol{N}} = \mathbf{0}$ and $\boldsymbol{\mathcal{U}}_j^R = \mathbf{0}$ yields the attetuation rate in time ω_j^I, given by

  $$\omega_j^I\boldsymbol{\mathcal{U}}_j^I = \boldsymbol{\mathcal{J}}\boldsymbol{\mathcal{U}}_j^I; \qquad \omega_j^I = k_j c_j^I, \tag{50}$$

  which describes the relaxation dynamics and quantifies the dissipative response of the system. In this regime, the analysis focuses on temporal decay of internal variables whilst deformation remains fixed.

These two limiting cases highlight the dual nature of the governing equations, namely a wave-like (hyperbolic) component driven by convective fluxes, and a dissipative (relaxational) component controlled by internal dissipation.

4.1. Hyperbolicity and its associated wave speed

Utilising the concept of directional derivative [29], it is instructive to observe that expression (49) can be recast into the eigenvalue form $D\boldsymbol{\mathcal{F}}_{\boldsymbol{N}}[\boldsymbol{\mathcal{U}}_j^R] = c_j^R \boldsymbol{\mathcal{U}}_j^R$. Applying this framework to the conservation equations considered in this study yields the system

$$-\begin{bmatrix} D(\boldsymbol{PN})[\boldsymbol{F}_j, \boldsymbol{H}_j, J_j, \boldsymbol{Y}_1^j, y_1^j, \dots, \boldsymbol{Y}_{n_M}^j, y_{n_M}^j] \\ D\left(\frac{1}{\rho_R}\boldsymbol{p}_R \otimes \boldsymbol{N}\right)[\boldsymbol{p}_R^j] \\ D\left(\boldsymbol{F} \times \left(\frac{1}{\rho_R}\boldsymbol{p}_R \otimes \boldsymbol{N}\right)\right)[\boldsymbol{p}_R^j, \boldsymbol{F}_j] \\ D\left(\boldsymbol{H} : \left(\frac{1}{\rho_R}\boldsymbol{p}_R \otimes \boldsymbol{N}\right)\right)[\boldsymbol{p}_R^j, \boldsymbol{H}_j] \\ \boldsymbol{0} \\ 0 \\ \vdots \\ \boldsymbol{0} \\ 0 \end{bmatrix} = c_j^R \begin{bmatrix} \boldsymbol{p}_R^j \\ \boldsymbol{F}_j \\ \boldsymbol{H}_j \\ J_j \\ \boldsymbol{Y}_1^j \\ y_1^j \\ \vdots \\ \boldsymbol{Y}_{n_M}^j \\ y_{n_M}^j \end{bmatrix}. \tag{51}$$

Since the evolution equations for $\{\mathcal{Y}_1^j, \dots, \mathcal{Y}_{n_M}^j\}$ are governed by local differential equations without spatial flux terms, they do not contribute to the characteristic structure of the system. Therefore, they can be excluded from the wave speed analysis.

Let us first consider the geometric conservation equation for $\boldsymbol{F}_j$, $\boldsymbol{H}_j$, and J_j. For a non-trivial solution with $c_j^R \neq 0$, and after enforcing the involutions constraints, the resulting expressions are [33]

$$\boldsymbol{F}_j = -\frac{1}{c_j^R}\boldsymbol{v}_j \otimes \boldsymbol{N}; \qquad \boldsymbol{H}_j = -\boldsymbol{F} \times \left(\frac{1}{c_j^R}\boldsymbol{v}_j \otimes \boldsymbol{N}\right); \qquad J_j = -\boldsymbol{H} : \left(\frac{1}{c_j^R}\boldsymbol{v}_j \otimes \boldsymbol{N}\right). \tag{52}$$

Using these relations, we turn to the linear momentum equation $\boldsymbol{p}_R^j$

$$-c_j^R \boldsymbol{p}_R^j = -\rho_R c_j^R \boldsymbol{v}_j = D(\boldsymbol{PN})\left[\boldsymbol{F}_j, \boldsymbol{H}_j, J_j, \boldsymbol{0}, 0, \dots, \boldsymbol{0}, 0\right]. \tag{53}$$

Multiplying by an arbitrary virtual velocity field $\delta\boldsymbol{v}$ and using the definitions for the first Piola $\boldsymbol{P}$ (14) and the area map $\boldsymbol{H}_j = \boldsymbol{F} \times \boldsymbol{F}_j$ yields the following reduced expression

$$\rho_R\left(c_j^R\right)^2 \delta\boldsymbol{v} \cdot \boldsymbol{v}_j = \begin{bmatrix} (\delta\boldsymbol{v} \otimes \boldsymbol{N}) : \\ \boldsymbol{F} \times (\delta\boldsymbol{v} \otimes \boldsymbol{N}) : \\ \boldsymbol{H} : (\delta\boldsymbol{v} \otimes \boldsymbol{N}) \end{bmatrix}^T [\mathbb{H}_{\chi\chi}] \begin{bmatrix} : (\boldsymbol{v}_j \otimes \boldsymbol{N}) \\ : \boldsymbol{F} \times (\boldsymbol{v}_j \otimes \boldsymbol{N}) \\ \boldsymbol{H} : (\boldsymbol{v}_j \otimes \boldsymbol{N}) \end{bmatrix}. \tag{54}$$

It is worth noting that the (polyconvex) Hessian operator $[\mathbb{H}_{\chi\chi}]$ depends only on the triplet of deformation measures. By setting $\delta\boldsymbol{v} = \boldsymbol{v}_j$, the Legendre-Hadamard condition ensures that the system remains hyperbolic, meaning all wave speeds are real and physically meaningful.

Instead of deriving a closed-form solution for any possible orientation $\boldsymbol{N}$, it is sufficient to obtain bounds for the wave speeds by assuming $\boldsymbol{N}$ aligns with a principal direction. The first two eigenvalues correspond to pressure wave speeds c_p, obtained by choosing $\boldsymbol{v}_j = \boldsymbol{n}$, where $\boldsymbol{n}$ is a unit vector orthogonal to the vectors $\boldsymbol{t}_{1,2} = \boldsymbol{FT}_{1,2}/\|\boldsymbol{FT}_{1,2}\|$ spanning the propagation surface. By enforcing $\delta\boldsymbol{v} = \boldsymbol{v}_j = \boldsymbol{n}$ and substituting the Hessian components $\{W_{\boldsymbol{FF}}^{\infty}, W_{\boldsymbol{HH}}^{\infty}, W_{JJ}^{\infty}, W_{\boldsymbol{FF}}^{\alpha}, W_{JJ}^{\alpha}\}$ (derived in A) for $[\mathbb{H}_{\chi\chi}]$ into (54), the resulting expression after some algebraic manipulation yields

$$c_{1,2} = \pm c_p, \tag{55}$$

where the pressure wave speed c_p is given by

$$c_p = \sqrt{\left(\frac{2\xi + 2\zeta\Lambda_I^2 + f''_{\infty}\Lambda_{\boldsymbol{H}}^2}{\rho_R}\right) + \sum_{\alpha=1}^{n_M}\left(\frac{\mu_\alpha \boldsymbol{N} \cdot \left(\boldsymbol{Y}_\alpha^{-1}\boldsymbol{N}\right) + \mu_\alpha \Lambda_{\boldsymbol{H}}^2 J^{-2}}{\rho_R}\right)}. \tag{56}$$

The associated eigenvectors $\boldsymbol{\mathcal{U}}_\alpha$ are

$$\boldsymbol{\mathcal{U}}_{1,2}^R = \begin{bmatrix} \boldsymbol{n} \\ -\frac{1}{c_{1,2}}\boldsymbol{n} \otimes \boldsymbol{N} \\ -\frac{1}{c_{1,2}}\boldsymbol{F} \times (\boldsymbol{n} \otimes \boldsymbol{N}) \\ -\frac{1}{c_{1,2}}\boldsymbol{H} : (\boldsymbol{n} \otimes \boldsymbol{N}) \\ \boldsymbol{0} \\ 0 \\ \vdots \\ \boldsymbol{0} \\ 0 \end{bmatrix}. \tag{57}$$

Similarly, setting $\boldsymbol{v}_j = \boldsymbol{t}_{1,2}$ yields the other four eigenvalues corresponding to the shear wave speeds, namely

$$c_{3,4}^R = \pm c_{s_1}; \qquad c_{5,6}^R = \pm c_{s_2}, \tag{58}$$

where

$$c_{s_1} = \sqrt{\left(\frac{2\xi + 2\zeta\lambda_2^2}{\rho_R}\right) + \sum_{\alpha=1}^{n_{\mathrm{M}}}\left(\frac{\mu_\alpha \boldsymbol{N}\cdot\left(\boldsymbol{Y}_\alpha^{-1}\boldsymbol{N}\right)}{\rho_R}\right)}; \quad c_{s_2} = \sqrt{\left(\frac{2\xi + 2\zeta\lambda_1^2}{\rho_R}\right) + \sum_{\alpha=1}^{n_{\mathrm{M}}}\left(\frac{\mu_\alpha \boldsymbol{N}\cdot\left(\boldsymbol{Y}_\alpha^{-1}\boldsymbol{N}\right)}{\rho_R}\right)}. \tag{59}$$

Here, $\lambda_{1,2}^2$ are the eigenvalues of $\boldsymbol{\Lambda}_T$ given by

$$\boldsymbol{\Lambda}_T = \lambda_1^2 \boldsymbol{t}_1 \otimes \boldsymbol{t}_1 + \lambda_2^2 \boldsymbol{t}_2 \otimes \boldsymbol{t}_2. \tag{60}$$

The corresponding eigenvectors are

$$\boldsymbol{\mathcal{U}}_{3,4}^R = \begin{bmatrix} \boldsymbol{t}_1 \\ -\frac{1}{c_{3,4}}\boldsymbol{t}_1 \otimes \boldsymbol{N} \\ -\frac{1}{c_{3,4}}\boldsymbol{F}\times\left(\boldsymbol{t}_1 \otimes \boldsymbol{N}\right) \\ 0 \\ \boldsymbol{0} \\ 0 \\ \vdots \\ \boldsymbol{0} \\ 0 \end{bmatrix}; \quad \boldsymbol{\mathcal{U}}_{5,6} = \begin{bmatrix} \boldsymbol{t}_2 \\ -\frac{1}{c_{5,6}}\boldsymbol{t}_2 \otimes \boldsymbol{N} \\ -\frac{1}{c_{5,6}}\boldsymbol{F}\times\left(\boldsymbol{t}_2 \otimes \boldsymbol{N}\right) \\ 0 \\ \boldsymbol{0} \\ 0 \\ \vdots \\ \boldsymbol{0} \\ 0 \end{bmatrix}. \tag{61}$$

Remark 4. Linearising the evolution equations of the internal variables for each Maxwell branch α about thermodynamic equilibrium yields

$$\begin{aligned} c_j^I \kappa_j \bar{\boldsymbol{Y}}_j^I &= D\boldsymbol{\mathcal{R}}_{\boldsymbol{Y}_j}[\bar{\boldsymbol{Y}}_j^I]\Big|_{\boldsymbol{C}^{-1}\boldsymbol{Y}_j \approx \boldsymbol{I}} = -\frac{1}{\tau_\alpha}\bar{\boldsymbol{Y}}_j^I, \\ c_j^I \kappa_j \bar{y}_j^I &= D\mathcal{R}_{y_j}[\bar{\boldsymbol{Y}}_j^I, \bar{y}_j^I]\Big|_{\mathrm{tr}(\boldsymbol{C}^{-1}\boldsymbol{Y}_j)\approx 3} = \frac{1}{\tau_\alpha} y_j \boldsymbol{C}^{-1} : \bar{\boldsymbol{Y}}_j^I. \end{aligned} \tag{62}$$

This leads to the following eigenvalues for the internal variable subsystem

$$c_{1-6}^I = -\frac{1}{\kappa_j \tau_\alpha} \quad \text{and} \quad c_7^I = 0. \tag{63}$$

Thus, each Maxwell branch contributes six exponentially decaying eigenmodes associated with $\boldsymbol{Y}_j$, and one non-decaying eigenmode associated with y_j. This results in a total of $6 \times n_{\mathrm{M}}$ dissipative modes that do not influence wave propagation directly.

4.2. Second law of thermodynamics

We revisit the global form of the second law of thermodynamics expressed in terms of the convex entropy function S. The time derivative of the entropy function over the material configuration Ω_R is written as

$$\frac{d}{dt}\int_{\Omega_R} S\, d\Omega_R = \int_{\Omega_R} \frac{\partial \hat{S}(\boldsymbol{p}_R, \boldsymbol{\mathcal{X}}_{\mathcal{Y}})}{\partial t}\, d\Omega_R. \tag{64}$$

Applying the chain rule to expand the total time derivative in terms of its variables yields

$$\frac{d}{dt}\int_{\Omega_R} S\, d\Omega_R = \int_{\Omega_R} \left(\frac{\partial \hat{S}}{\partial \boldsymbol{p}_R}\cdot\frac{\partial \boldsymbol{p}_R}{\partial t} + \frac{\partial \hat{S}}{\partial \boldsymbol{\mathcal{X}}} \bullet \frac{\partial \boldsymbol{\mathcal{X}}}{\partial t} + \underbrace{\sum_{\alpha=1}^{n_{\mathrm{M}}}\left(\frac{\partial \hat{S}}{\partial \boldsymbol{Y}_\alpha} : \frac{\partial \boldsymbol{Y}_\alpha}{\partial t} + \frac{\partial \hat{S}}{\partial y_\alpha}\frac{\partial y_\alpha}{\partial t}\right)}_{-\dot{D}_{\mathrm{int}}} \right) d\Omega_R. \tag{65}$$

Here, we introduce the operator $\bullet$ as a compact notation to represent the combined contractions over the geometric variables $\boldsymbol{\mathcal{X}}$ as $\frac{\partial \hat{S}}{\partial \boldsymbol{\mathcal{X}}} \bullet \frac{\partial \boldsymbol{\mathcal{X}}}{\partial t} = \frac{\partial \hat{S}}{\partial \boldsymbol{F}} : \frac{\partial \boldsymbol{F}}{\partial t} + \frac{\partial \hat{S}}{\partial \boldsymbol{H}} : \frac{\partial \boldsymbol{H}}{\partial t} + \frac{\partial \hat{S}}{\partial J}\frac{\partial J}{\partial t}$. Substituting the conjugate relations from (36) and the local entropy production $\dot{D}_{\mathrm{int}}$ from (16) leads to

$$\frac{d}{dt}\int_{\Omega_R} S\, d\Omega_R = \int_{\Omega_R} \left(\boldsymbol{v}\cdot\frac{\partial \boldsymbol{p}_R}{\partial t} + \underbrace{\left(\boldsymbol{\Sigma}_{\boldsymbol{F}} + \boldsymbol{\Sigma}_{\boldsymbol{H}}\times\boldsymbol{F} + \Sigma_J \boldsymbol{H}\right)}_{\boldsymbol{P}} : \boldsymbol{\nabla}_0 \boldsymbol{v} - \dot{D}_{\mathrm{int}} \right) d\Omega_R. \tag{66}$$

To derive a physically meaningful expression for the global evolution of S, we substitute the weak form of the linear momentum conservation equation (obtained via integration by parts) into the expression above. This naturally leads to a reformulation that separates internal dissipation and the mechanical power of external forces, as described by

$$\frac{d}{dt}\int_{\Omega_R} S\, d\Omega_R - \dot{\Pi}_{\mathrm{ext}} = -\int_{\Omega_R} \dot{D}_{\mathrm{int}}\, d\Omega_R; \qquad \dot{\Pi}_{\mathrm{ext}} = \int_{\Omega_R} \boldsymbol{v}\cdot\boldsymbol{f}_R\, d\Omega_R + \int_{\partial\Omega_R} \boldsymbol{v}_B \cdot \boldsymbol{t}_B\, dA_R, \tag{67}$$

where $\dot{\Pi}_{\text{ext}}$ denotes the mechanical power of external forces. Thermodynamic consistency requires non-negative internal dissipation $\dot{\mathcal{D}}_{\text{int}} \geq 0$, ensuring the right-hand side of (67) is non-positive. This leads to the inequality

$$\frac{d}{dt}\int_{\Omega_R} S\, d\Omega_R - \dot{\Pi}_{\text{ext}} \leq 0, \tag{68}$$

which is a global expression of the second law of thermodynamics [52]. Satisfaction of inequality (68) is a necessary *ab initio* requirement for stability and thermodynamic admissibility, aligning with the classical Coleman-Noll procedure [28,30,53,54].

Remark 5. For an isolated elastic body, where the external work from body and boundary forces vanish (i.e., $\dot{\Pi}_{\text{ext}} = 0$) and viscous dissipation is absent (i.e., $\dot{\mathcal{D}}_{\text{int}} = 0$), expression (67) simplifies to the conservation of total energy, given by

$$\frac{d}{dt}\int_{\Omega_R} S\, d\Omega_R = 0. \tag{69}$$

5. Smoothed particle hydrodynamics spatial discretisation

5.1. SPH approximation for conservation equations

We consider a solid discretised in space by a set of particles. In this collocation-based framework, each particle also serves as a quadrature (integration) point. The material gradient of a velocity field $\boldsymbol{v}$ at particle a is then approximated as

$$\boldsymbol{\nabla}_0 \boldsymbol{v}(\boldsymbol{X}_a, t) \approx \frac{1}{\Omega_R^a}\sum_{b\in\Lambda_a}\frac{1}{2}\big(\boldsymbol{v}_b(t) - \boldsymbol{v}_a(t)\big)\otimes \boldsymbol{C}_{ab}; \qquad \boldsymbol{C}_{ab} = 2\Omega_R^a\Omega_R^b\tilde{\boldsymbol{\nabla}}_0 W_b(\boldsymbol{X}_a). \tag{70}$$

Here, $b \in \Lambda_a$ denotes the set of neighbouring particles b located within the support radius of particle a, and Ω_R^b is the material volume associated with neighbour b. The term $-\boldsymbol{v}_a$ ensures zero contribution for a constant field. The corrected kernel gradient $\tilde{\boldsymbol{\nabla}}_0$ enforces exactness for linear fields given by [55–57]

$$\tilde{\boldsymbol{\nabla}}_0 W_b(\boldsymbol{X}_a) = \boldsymbol{L}_a \boldsymbol{\nabla}_0 W_b(\boldsymbol{X}_a); \qquad \boldsymbol{L}_a = \left[\sum_{b\in\Lambda_a}\Omega_R^b \boldsymbol{\nabla}_0 W_b(\boldsymbol{X}_a)\otimes(\boldsymbol{X}_b - \boldsymbol{X}_a)\right]^{-1}. \tag{71}$$

Note that due to SPH gradient correction, $\boldsymbol{C}_{ab} \neq -\boldsymbol{C}_{ba}$. For further details, readers are referred to References [56,57].

In the current work, we adopt a reduced formulation for $\{\boldsymbol{p}_R, \boldsymbol{\mathcal{X}}, \boldsymbol{C}_{v_\alpha}^{-1}\}$ that retains the necessary kinematic and internal variables whilst simplifying viscous calibration. Using the SPH velocity gradient approximation (70) and ensuring variational consistency following References [2,58], we approximate the evolution of these variables as

$$\frac{d\boldsymbol{p}_R^a(t)}{dt} = \boldsymbol{E}_a(t) - \boldsymbol{T}_a(t) + \boldsymbol{\mathcal{D}}_a(t); \tag{72a}$$

$$\frac{d\boldsymbol{F}_a(t)}{dt} = \boldsymbol{\nabla}_0 \boldsymbol{v}(\boldsymbol{X}_a, t); \tag{72b}$$

$$\frac{d\boldsymbol{H}_a(t)}{dt} = \boldsymbol{F}_a(t) \boldsymbol{\times} \boldsymbol{\nabla}_0 \boldsymbol{v}(\boldsymbol{X}_a, t); \tag{72c}$$

$$\frac{d\boldsymbol{J}_a(t)}{dt} = \boldsymbol{H}_a(t) : \boldsymbol{\nabla}_0 \boldsymbol{v}(\boldsymbol{X}_a, t); \tag{72d}$$

$$\left.\frac{d\boldsymbol{C}_{v_\alpha,a}^{-1}(t)}{dt}\right|_{\boldsymbol{X}} = \frac{1}{\tau_\alpha}\Big(\boldsymbol{C}_a^{-1}(t) - \boldsymbol{C}_{v_\alpha,a}^{-1}(t)\Big); \qquad \alpha = \{1, \ldots, n_{\text{M}}\}. \tag{72e}$$

The external and internal forces acting on particle a are given by

$$\boldsymbol{E}_a(t) = \frac{A_R^a}{\Omega_R^a}\boldsymbol{t}_B^a(t) + \boldsymbol{f}_R^a(t); \qquad \boldsymbol{T}_a(t) = \sum_{b\in\Lambda_a^b}\boldsymbol{T}_{ab}(t); \qquad \boldsymbol{T}_{ab}(t) = \frac{1}{2}\big(\boldsymbol{P}_b(t)\boldsymbol{C}_{ba} - \boldsymbol{P}_a(t)\boldsymbol{C}_{ab}\big), \tag{73}$$

where A_R^a is the material tributary area and $\boldsymbol{t}_B^a$ is the prescribed boundary traction. For particles not on the boundary, $A_R^a = 0$[10]. In this SPH formulation, the pairwise internal force is antisymmetric $\boldsymbol{T}_{ba} = -\boldsymbol{T}_{ab}$, which guarantees local and global conservation of linear momentum. Moreover, the discrete SPH formulations of the divergence and gradient operators are skew-adjoint, ensuring that conservative forces do not lead to spurious dissipation [59]. The full SPH derivation of expressions (72a) and (72d) from their weak form is provided in References [41,42].

Following previous work by the authors [1,2,58], the dissipation term satisfies pairwise antisymmetry, that is, $\boldsymbol{\mathcal{D}}_a = \sum_{b\in\Lambda_a^b}\boldsymbol{\mathcal{D}}_{ab}$ with $\boldsymbol{\mathcal{D}}_{ab} = -\boldsymbol{\mathcal{D}}_{ba}$. Specifically,[11]

$$\boldsymbol{\mathcal{D}}_{ab} = \boldsymbol{S}_{ab}\big(\boldsymbol{v}_b - \boldsymbol{v}_a\big), \tag{74}$$

[10] The numerical examples presented in this paper are driven by a prescribed initial velocity field, so no external prescribed boundary tractions are applied and the tributary areas do not play a role.

[11] See Appendix B for the derivation of the pair-wise dissipation using the time rate of the convex entropy extension.

where $\boldsymbol{S}_{ab}$ is the self-adjoint dissipation operator, acting on the velocity jump [58,60,61]. Such a formulation is a characteristic of Godunov-type upwinding terms [62], commonly referred to as Riemann solvers [4]. To achieve second-order accuracy, a linear reconstruction procedure[12] must be applied to reconstruct the associated velocities at the mid-edge between particle pairs a and b. Further details can be found in References [1,63].

The symmetric positive semi-definite stabilisation matrix is then chosen to combine both pressure and shear waves components, expressed as

$$\boldsymbol{S}_{ab} = \frac{1}{2}\rho_R^{\text{Ave}}\|\boldsymbol{C}_{ab}^{\text{Skew}}\|\Big[c_p^{\text{Ave}}\boldsymbol{n}_{ab}\otimes\boldsymbol{n}_{ab} + c_s^{\text{Ave}}\big(\boldsymbol{I}-\boldsymbol{n}_{ab}\otimes\boldsymbol{n}_{ab}\big)\Big], \tag{75}$$

where $[\bullet]^{\text{Ave}} = \frac{1}{2}\big([\bullet]_a + [\bullet]_b\big)$, $\boldsymbol{C}_{ab}^{\text{Skew}} = \frac{1}{2}\big(\boldsymbol{C}_{ab} - \boldsymbol{C}_{ba}\big)$ and $\|\boldsymbol{C}_{ab}^{\text{Skew}}\|^2 = \boldsymbol{C}_{ab}^{\text{Skew}}\cdot\boldsymbol{C}_{ab}^{\text{Skew}}$.

Finally, to track the evolution of the deformed geometry, the following discretised kinematic relation is employed

$$\frac{d\boldsymbol{\phi}_a(t)}{dt} = \boldsymbol{v}_a(t). \tag{76}$$

6. Time integration

Given the size of the semi-discrete equations, we employ a three-stage Runge-Kutta explicit time integrator [3,6,7] to advance the solution from time step t^n to t^{n+1} as

$$\begin{aligned}
\boldsymbol{\mathcal{U}}_a^{\star} &= \boldsymbol{\mathcal{U}}_a^n + \Delta t\,\dot{\boldsymbol{\mathcal{U}}}_a^n(\boldsymbol{\mathcal{U}}_a^n),\\
\boldsymbol{\mathcal{U}}_a^{\star\star} &= \frac{3}{4}\boldsymbol{\mathcal{U}}_a^n + \frac{1}{4}\Big(\boldsymbol{\mathcal{U}}_a^{\star} + \Delta t\,\dot{\boldsymbol{\mathcal{U}}}_a^{\star}(\boldsymbol{\mathcal{U}}_a^{\star})\Big),\\
\boldsymbol{\mathcal{U}}_a^{n+1} &= \frac{1}{3}\boldsymbol{\mathcal{U}}_a^n + \frac{2}{3}\Big(\boldsymbol{\mathcal{U}}_a^{\star\star} + \Delta t\,\dot{\boldsymbol{\mathcal{U}}}_a^{\star\star}(\boldsymbol{\mathcal{U}}_a^{\star\star})\Big).
\end{aligned} \tag{77}$$

Here, $\boldsymbol{\mathcal{U}}_a$ consists of the primary unknowns $\{\boldsymbol{p}_R^a, \boldsymbol{F}_a, \boldsymbol{H}_a, J_a\}$. These variables, along with the particle geometry $\boldsymbol{\phi}_a$, are updated explicitly in time using the Runge-Kutta scheme described above. The internal variables (72e), however, are updated analytically over the same time increment Δt. In this work, the term $\boldsymbol{C}_a^{-1}$ and the relaxation times τ_α are held fixed during each time interval. Under these conditions, the exact solution of the linear evolution Eq. (72e) reads

$$\boldsymbol{C}_{v_\alpha,a}^{-1,n+1} = (1-\epsilon)\boldsymbol{C}_{v_\alpha,a}^{-1,n} + \epsilon\boldsymbol{C}_a^{-1,n}; \qquad \epsilon = 1 - e^{-\frac{\Delta t}{\tau_\alpha}}, \tag{78}$$

where $\epsilon \in [0,1]$ is the relaxation fraction over the time step. This provides an exact temporal update of the internal viscoelastic state, whilst the conservation equations for linear momentum, deformation measures, and geometry are advanced explicitly using the Runge-Kutta scheme in (77). The maximum time step Δt is restricted by[13]

$$\Delta t \le \min\left(\alpha_{CFL}\min\left(\frac{h_{\min}}{c_p}\right), \alpha_{\text{relax}}\tau_{\min}\right), \tag{79}$$

where $\tau_{\min} = \min_\alpha \tau_\alpha$. Here, α_{CFL} is the Courant-Friedrichs-Lewy (CFL) stability number, α_{relax} is typically chosen to be less than 1 to account for the stability limit of the relaxation terms, c_p is the pressure wave speed (as defined in (56)) which in this work is obtained directly from the proposed viscoelastic constitutive model, and $h_{\min}$ is the minimum (or characteristic) particle spacing within the computational domain. In this work, we consider convective-dominated problems in which relaxation stability can be neglected. A large $\tau_{\min}$ value makes the convective term the primary constraint on Δt. Unless specified otherwise, a value of $\alpha_{CFL} = 0.9$ is chosen in the subsequent examples to ensure a balance between accuracy and stability.

7. Numerical examples

Several two- and three-dimensional problems are presented to demonstrate the capabilities of the proposed SPH algorithm. First, a manufactured problem for linear viscelasticity is used to examine the convergence order of the scheme. Second, the stability of the algorithm is assessed by verifying that it does not exhibit spurious zero-energy modes, using punch and tensile test cases. Third, the performance of the algorithm under large strain is investigated through a twisting column and a thin plate problem. Fourth, the applicability of the method to challenging thin-walled structures is demonstrated. In all examples, the viscoelastic material properties (such as relaxation time τ_α and proportionality factor β_α) are purely numerical and not experimentally calibrated. The primary objective of the current paper is to assess the effectiveness and efficiency of the SPH algorithm for viscoelastic solids. Solutions obtained with the proposed Total Lagrangian SPH scheme are compared with analytical results, an in-house Updated Reference Lagrangian SPH (URL-SPH) scheme [2,3], and a vertex-centred Finite Volume Method (FVM) [4–6,64].

7.1. Assessment of consistency and convergence

The main objective of this example is to demonstrate the order of convergence of the proposed SPH algorithm. Following the approach in References [1,30], we extend the analysis of an *ad-hoc* manufactured solution to linear viscoelasticity (see Appendix C).

[12] No slope limiter is required as the numerical examples in this work are restricted to smooth, large strain solids and are not dominated by shocks.
[13] The optimal time increment can be determined when appropriate maximum wave speeds are used, which generally depend on the constitutive model.

Table 1
Material properties for manufactured problem.

Equilibrium (long-term) linear elastic model		
Young's modulus [MPa]	E	17
Material density [kg/m^3]	ρ_R	1100
Poisson's ratio	ν	0.3
Non-equilibrium linear viscous model		
Number of Maxwell branch	n_{M}	1
Proportionality factor	β_1	0.1
Relaxation time [s]	τ_1	0.02

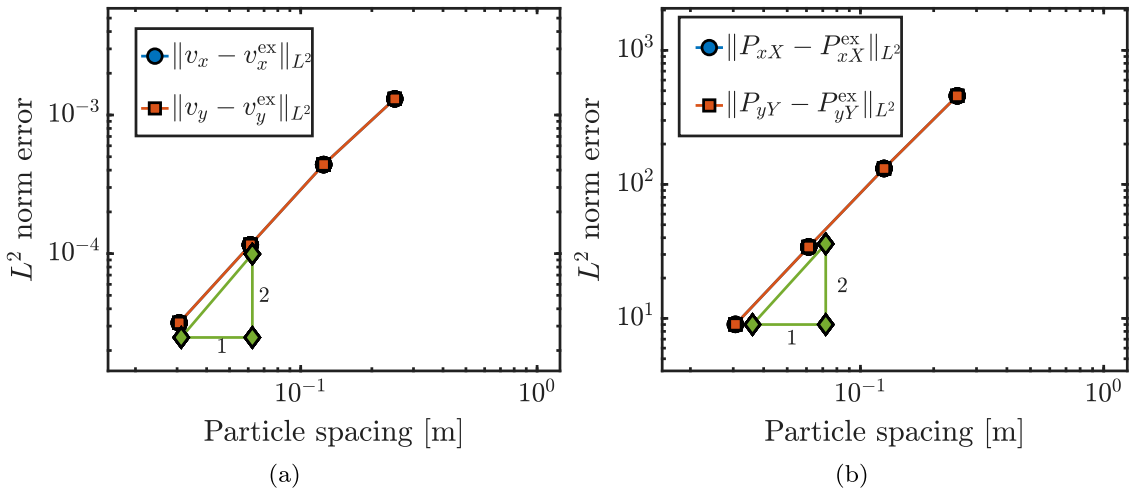

Fig. 1. Manufactured problem. L^2 global convergence analysis at time $t = 0.0094$ s for (a) the components of velocity, and (b) the components of the first Piola-Kirchhoff stress tensor. A linear viscoelastic model is used with parameters listed in Table 1.

We consider a unit square plate under plane strain. The west and south boundaries are constrained to move only tangentially, whilst the north and east boundaries are restricted to normal motion, as depicted in Figure 10 of Reference [1]. In the small deformation case, the mapping function $\boldsymbol{\varphi}(\boldsymbol{X}, t)$ is chosen as

$$\boldsymbol{\varphi}(\boldsymbol{X}, t) = \boldsymbol{X} + U_0 \cos\left(\frac{c_s \pi t}{\sqrt{2}}\right)\begin{bmatrix} \sin\left(\frac{\pi X_1}{2}\right)\cos\left(\frac{\pi X_2}{2}\right) \\ -\cos\left(\frac{\pi X_1}{2}\right)\sin\left(\frac{\pi X_2}{2}\right) \end{bmatrix}. \tag{80}$$

For values of U_0 below 0.001 m, the solution can be considered to be linear. The parameter c_s represents the shear wave for the linear viscoelasticity and is defined as

$$c_s = \sqrt{\frac{\bar{\mu}}{\rho_R}}; \qquad \bar{\mu} = \mu + \sum_{\alpha=1}^{n_{\mathrm{M}}} \left(\mu_\alpha e^{-\frac{t}{\tau_\alpha}}\right). \tag{81}$$

Consequently, the exact velocity and deformation gradient tensor can be computed as

$$\boldsymbol{v}(\boldsymbol{X}, t) = -\frac{\pi c_s U_0}{\sqrt{2}} \sin\left(\frac{c_s \pi t}{\sqrt{2}}\right)\begin{bmatrix} \sin\left(\frac{\pi X_1}{2}\right)\cos\left(\frac{\pi X_2}{2}\right) \\ -\cos\left(\frac{\pi X_1}{2}\right)\sin\left(\frac{\pi X_2}{2}\right) \end{bmatrix}, \tag{82}$$

and

$$\boldsymbol{F}(\boldsymbol{X}, t) = \begin{bmatrix} 1 + \alpha\cos\left(\frac{\pi X_1}{2}\right)\cos\left(\frac{\pi X_2}{2}\right) & -\alpha\sin\left(\frac{\pi X_1}{2}\right)\sin\left(\frac{\pi X_2}{2}\right) \\ \alpha\sin\left(\frac{\pi X_1}{2}\right)\sin\left(\frac{\pi X_2}{2}\right) & 1 - \alpha\cos\left(\frac{\pi X_1}{2}\right)\cos\left(\frac{\pi X_2}{2}\right) \end{bmatrix}; \qquad \alpha = \frac{U_0 \pi}{2}\cos\left(\frac{c_s \pi t}{\sqrt{2}}\right), \tag{83}$$

respectively.

This plate is initially loaded with deformation gradient (by substituting $t = 0$ into (83)) without any initial velocity. A list of parameters used for this simulation is summarised in Table 1. As compared to the closed form solutions described in (82) and (83), Fig. 1 shows the L^2 global convergence analysis at time $t = 0.0094$ s for (1) the components of the velocity $\boldsymbol{v}$, and (2) the components of the first Piola-Kirchhoff stress tensor $\boldsymbol{P}$. As expected, the proposed SPH algorithm achieves equal second-order convergence for all the variables solved, namely velocity and the stresses. This equal order convergence for all derived variables is one of the advantages of the mixed-based framework.

Table 2
Material properties for punch problem.

Equilibrium (long-term) Mooney-Rivin model		
Young's modulus [MPa]	E	17
Material density [kg/m^3]	ρ_R	1100
Poisson's ratio	ν	0.45
Parameters [Pa]	$\{\xi, \zeta\}$	$\{\mu/2, 0\}$
Non-equilibrium viscous model		
Number of Maxwell branch	n_{M}	1
Proportionality factor	β_1	3
Relaxation time [s]	τ_1	0.02

7.2. Assessment of robustness and numerical stability

In this section, we consider two dimensional problems under plane strain, previously studied in Reference [65]. The first problem involves the compression of a square plate subjected to an initial compressive velocity field. The second problem is a tensile test, in which the same plate with slightly modified boundary conditions, is stretched vertically. These examples are designed to assess the robustness of the proposed SPH algorithm for viscoelastic solid dynamics.

7.2.1. Punch test

A punch test case is presented. A square plate with unit side length of $L_X = L_Y = 1$ m is constrained by roller supports (i.e., symmetry boundary conditions) along the south, west, and east edges (see the left structure in Fig. 2). The domain is subjected to an initial smooth vertical velocity profile v_y given by[14]

$$\boldsymbol{v}\Big|_{t=0} = \boldsymbol{v}(\boldsymbol{X}, t=0) = \begin{bmatrix} 0 \\ v_y \end{bmatrix}; \qquad v_y = \begin{cases} \alpha \frac{2XY}{L_X L_Y}; & 0 \le X \le L_X/2 \\ \alpha \frac{Y}{L_Y}; & X \ge L_X/2 \end{cases}, \tag{84}$$

where $\alpha = -100$ m/s. Three levels of particle refinement are considered, namely {M1, M2, M3} corresponding to $\{289, 525, 1089\}$ particles, respectively. Material properties are summarised in Table 2.

First, a particle refinement study is carried out using the proposed SPH algorithm with compressible viscoelasticity. Fig. 3 shows the deformation and pressure distribution at $t = 3.1$ ms (top row) and $t = 10.2$ ms (bottom row). The first three columns (from left to right) show results for the proposed SPH algorithm at increasing refinement levels. The fourth column (second from the right) shows results from URL-SPH [2,3], and the last column (on the right) shows results from the vertex-centred FVM [4] for comparison. Both deformation patterns and pressure distributions converge as the particle resolution increases. Second, Fig. 4(a) presents the time history of different energy measures during the deformation process. It is interesting to notice how kinetic energy converts into strain

[14] The velocity profile is chosen to ensure smooth solutions, producing a deformation pattern with a wave-like spatial structure.

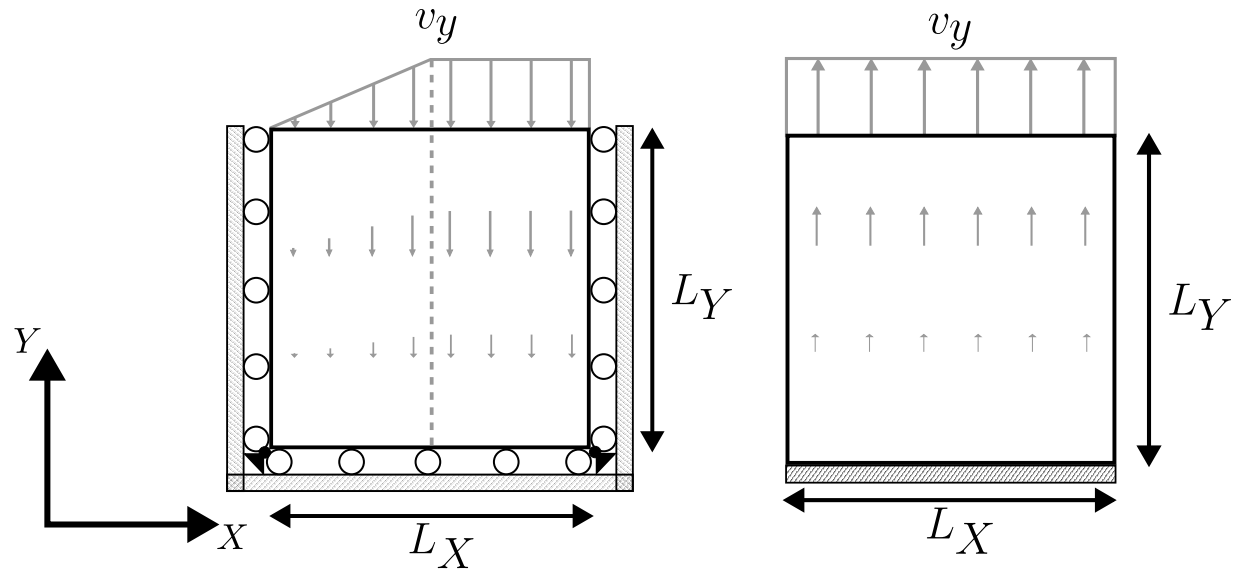

Fig. 2. (Left) Structure initialised with a compressive vertical velocity v_y. (Right) Structure initialised with a tensile vertical velocity v_y.

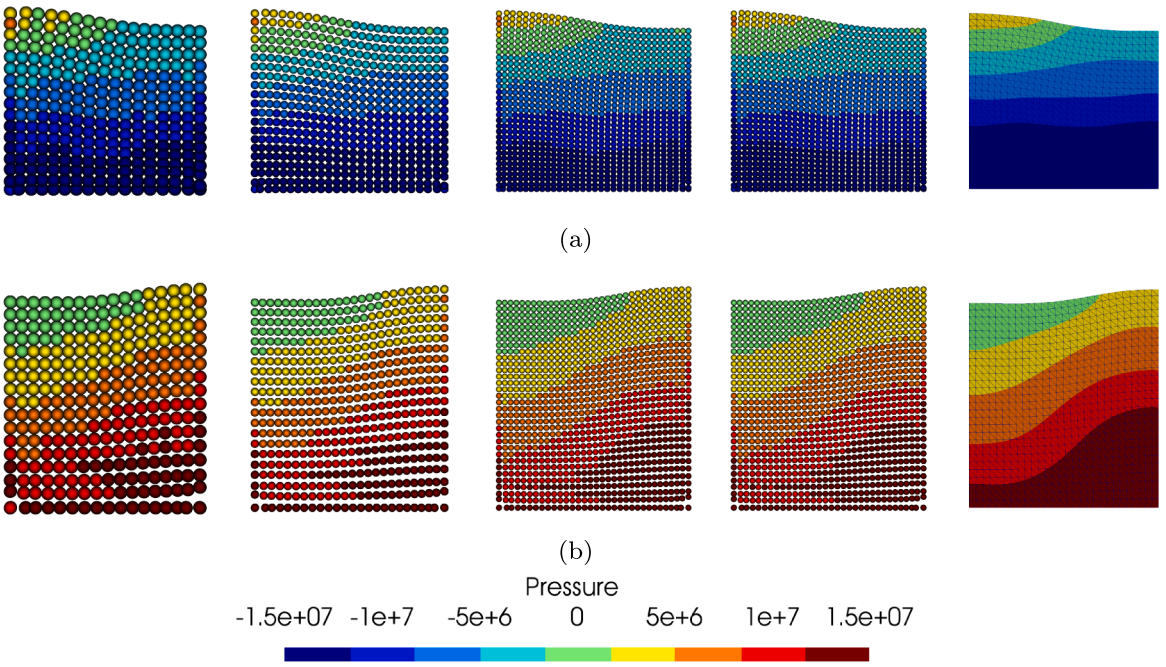

Fig. 3. Punch test. Comparison of deformed shapes using compressible viscoelasticity at time (a) $t = 3.1$ ms (b) $t = 10.2$ ms. The first three columns (left to right) show the particle refinement of a structure simulated using the proposed Total Lagrangian SPH algorithm. The fourth column (second from the right) shows results from an alternative in-house URL-SPH algorithm [3], and the last column (on the right) shows results from the vertex-centred FVM [4]. Colour indicates the pressure profile. Material properties are summarised in Table 2.

Table 3
Material properties for tensile problem.

Equilibrium (long-term) Mooney-Rivin model		
Young's modulus [GPa]	E	21
Material density [kg/m^3]	ρ_R	7000
Poisson's ratio	ν	0.3
Parameters [Pa]	$\{\xi, \zeta\}$	$\{\mu/2, 0\}$
Non-equilibrium viscous model		
Number of Maxwell branch	n_{M}	1
Proportionality factor	β_1	3
Relaxation time [s]	τ_1	0.02

energy and viscoelastic dissipation, with a small portion converting to numerical dissipation. The rate of internal (viscous) dissipation and the rate of numerical dissipation increase over time, ensuring discrete satisfaction of the second law of thermodynamics. This can be seen in Fig. 4(b) and (c). Third, for qualitative assessment, Fig. 4(d) tracks the time evolution of the vertical velocity component at $\boldsymbol{X} = [1, 1]^T$ m (top right corner of the plate), demonstrating convergence with refinement. Finally, Fig. 5 shows a series of deformed states using the M3 model, with the pressure profile indicated by the colour contour plot. Stable solutions are observed even over long-term simulations.

7.2.2. Tensile test

Similar to the punch test, a tensile test is considered to further study the material response under different loading conditions. A square plate is initially pulled vertically upward with $v_y = 500$ m/s (right structure in Fig. 2). The south boundary is fixed, whilst the remaining edges are traction-free. Material properties are summarised in Table 3. Fig. 6 compares the hyperelastic model (with parameter $\beta_1 = 0$) and the compressible viscoelastic model. Snapshots at time $t = \{0.62, 0.93, 1.23, 1.54, 1.86, 2.17\}$ ms show the pressure field. As expected, the viscoelastic model exhibits reduced deformation due to the dissipative effect of material viscosity, and the results agree well with those obtained using a vertex-centred FVM [4] (see Fig. 7). This behaviour is further analysed through the time history of energy measures, illustrated in Fig. 8. Comparing Fig. 8(a) (hyperelastic model) and (b) (viscoelastic model), the total energy (the sum of kinetic energy and strain energy) consistently decreases, primarily due to internal viscous dissipation. Specifically, the time derivatives of material and numerical dissipation remain non-negative throughout the entire simulation, as shown in Fig. 8(c) and (d). Moreover, the numerical dissipation introduced by the proposed SPH algorithm decreases with increasing

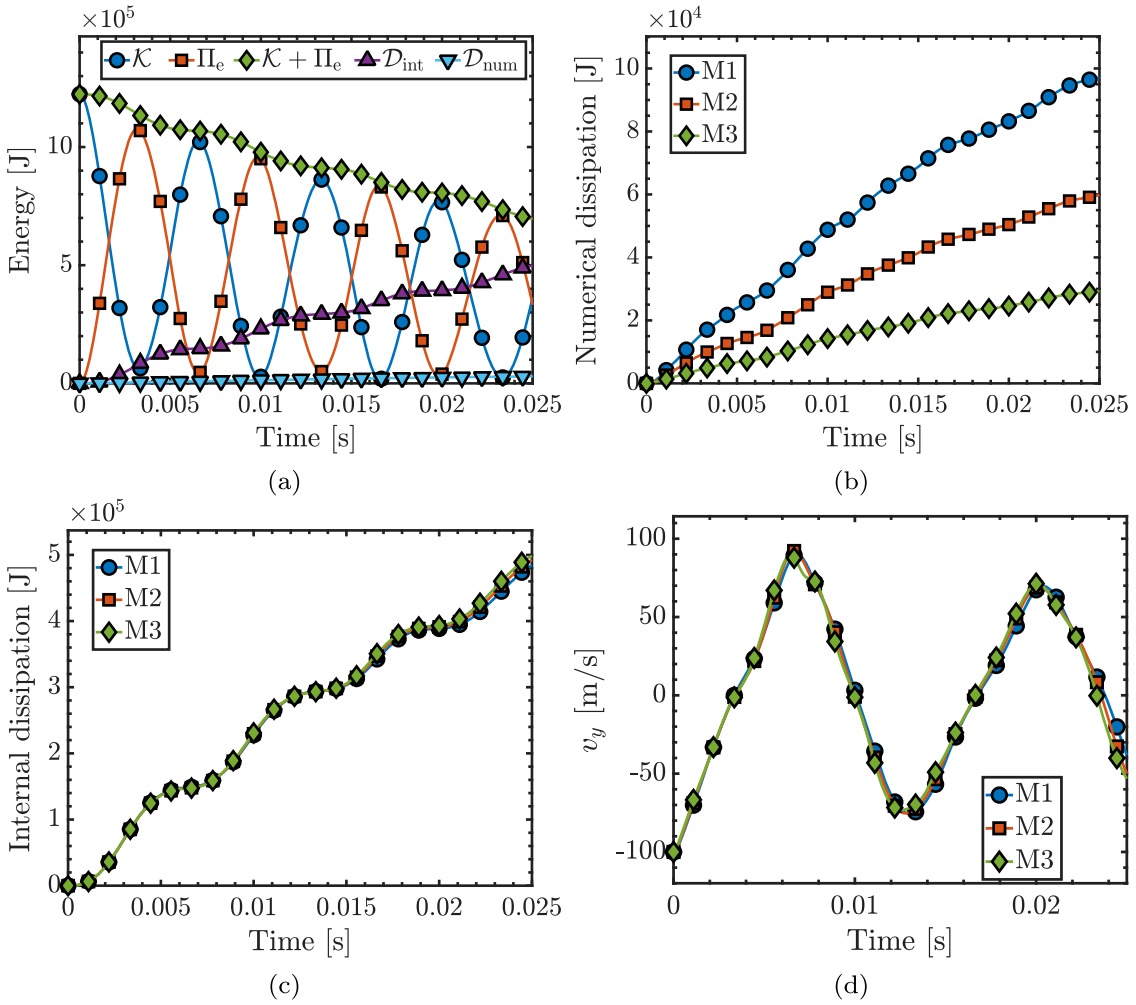

Fig. 4. Punch test. (a) Time evolution of various energy measures computed with discretisation M3, including kinetic energy $\mathcal{K}$, strain energy Π_e, the total energy (summation of kinetic and strain energies), internal viscous dissipation $\mathcal{D}_{\text{int}}$ and numerical dissipation $\mathcal{D}_{\text{num}}$. Time histories of (b) numerical dissipation and (c) internal viscous dissipation for varying particle refinements. (d) Time history of vertical velocity v_y at position $\boldsymbol{X} = [1, 1]^T$ m. Material properties are provided in Table 2.

Table 4
Material properties for twisting problem.

Equilibrium (long-term) Mooney-Rivin model		
Young's modulus [MPa]	E	17
Material density [kg/m^3]	ρ_R	1100
Poisson's ratio	ν	0.45
Parameters [Pa]	$\{\xi, \zeta\}$	$\{\mu/2, 0\}$
Non-equilibrium viscous model		
Number of Maxwell branch	n_{M}	1
Proportionality factor	β_1	1
Relaxation time [s]	τ_1	0.02

particle refinement, indicating the consistency of the method. In this case, M1, M2, and M3 correspond to 225, 441, and 841 SPH particles, respectively. For qualitative assessment, Fig. 9 monitors the time evolution of vertical velocity v_y and displacement u_y at $\boldsymbol{X} = [1, 1]^T$ m (top right corner of the plate). The SPH predictions agree closely with the vertex-centred FVM results, and accurate responses are obtained even with relatively few particles.

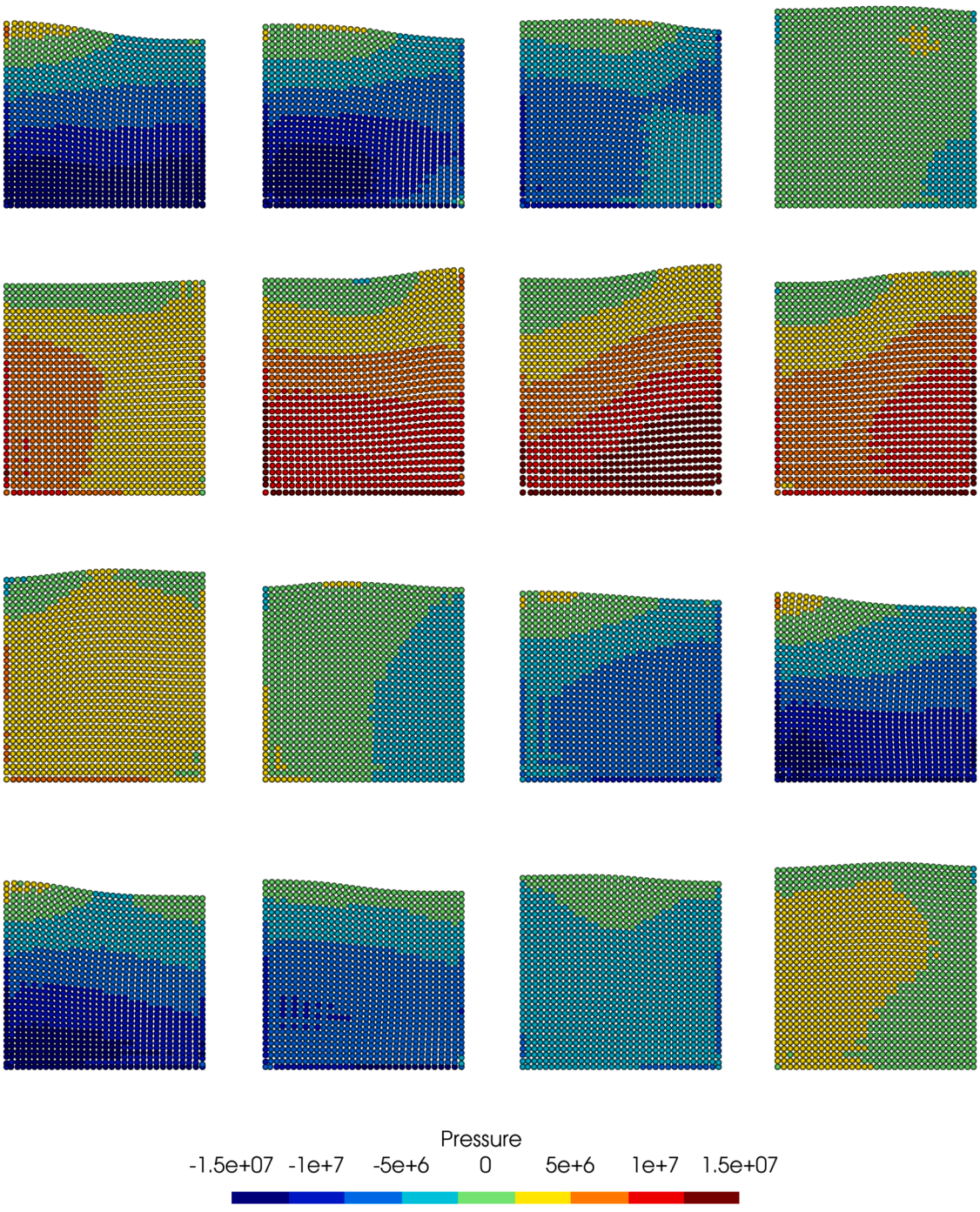

Fig. 5. Punch test. A sequence of deformed structures with pressure distribution at $t = \{3.1, 4.25, 5.4, 6.6, 7.75, 8.9, 10.15, 11.3, 12.45, 13.55, 14.7, 15.85, 17, 18.15, 19.25, 20.4\}$ ms (from left to right and top to bottom), respectively. Results obtained using the compressible viscoelastic model with **M3** model. Material properties are summarised in Table 2.

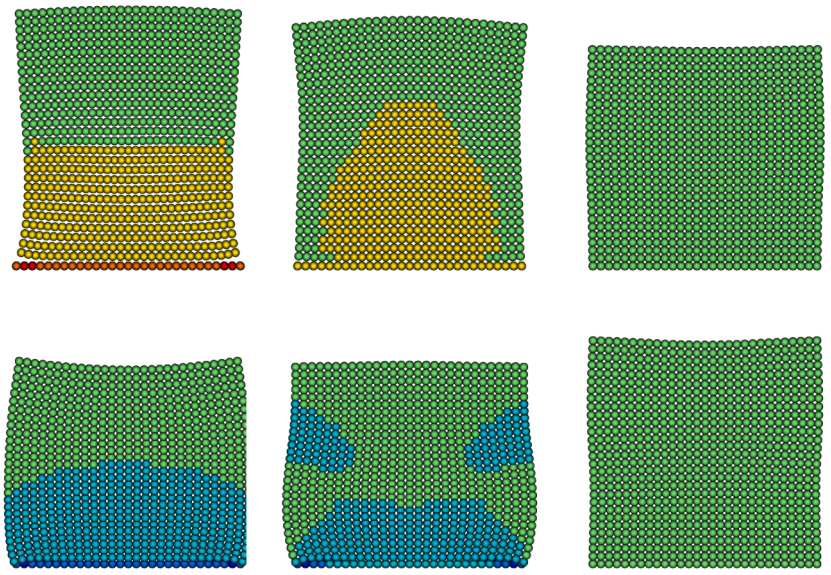

(a) Hyperelastic model (with $\beta_1 = 0$)

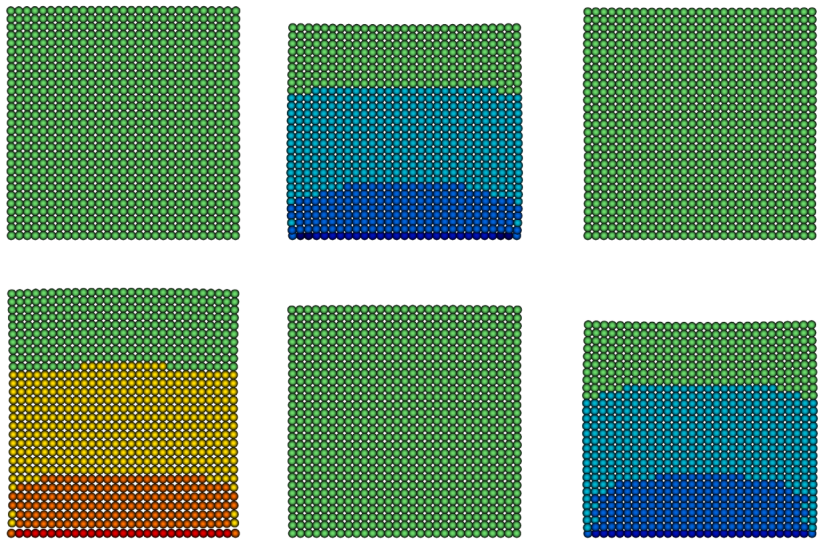

(b) Compressible viscoelasticity ($\beta_1 = 3$ and $\tau_1 = 0.02$ s)

Fig. 6. Tensile test. Sequence of deformed states at time $t = \{0.62, 0.93, 1.23, 1.54, 1.86, 2.17\}$ ms (from left to right and top to bottom) for (a) hyperelastic model (with $\beta_1 = 0$) and (b) compressible viscoelasticity. Colour represents the pressure field. Material properties are provided in Table 3.

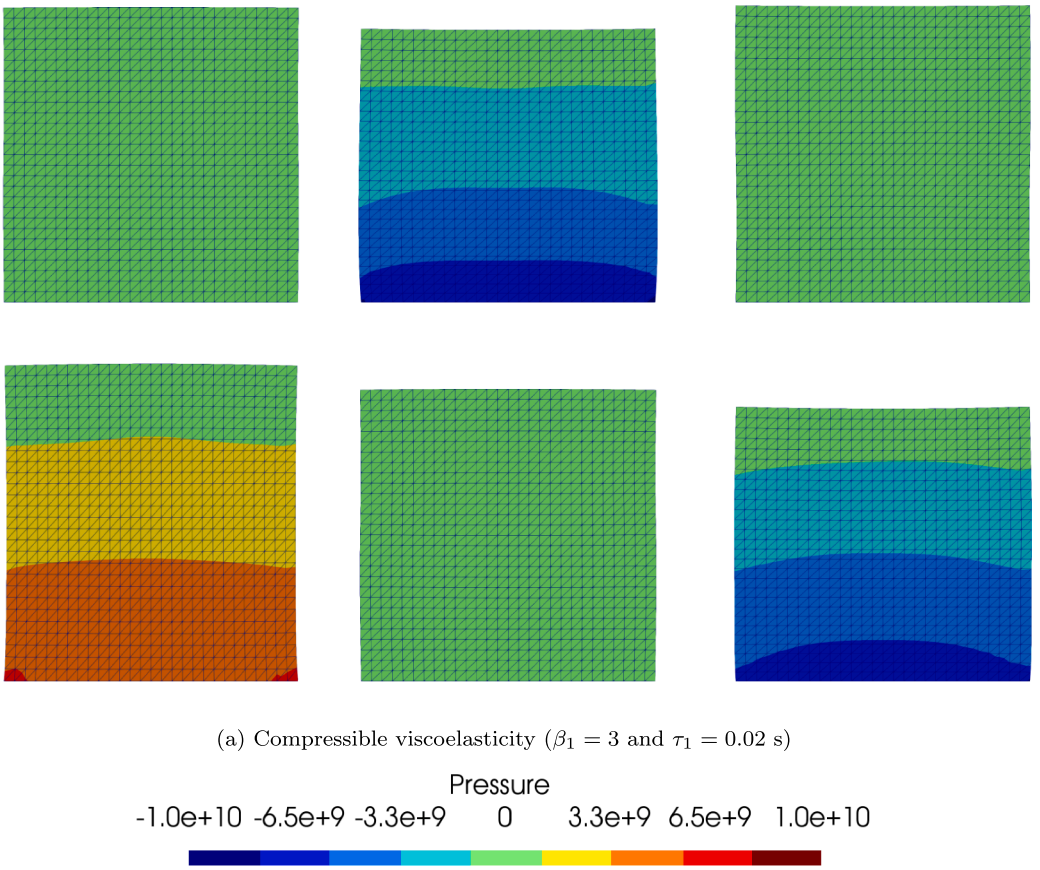

(a) Compressible viscoelasticity ($\beta_1 = 3$ and $\tau_1 = 0.02$ s)

Fig. 7. Tensile test. Sequence of deformed states at time $t = \{0.62, 0.93, 1.23, 1.54, 1.86, 2.17\}$ ms (from left to right and top to bottom) for compressible viscoelasticity using a vertex-centred FVM. Colour represents the pressure field. Material properties are provided in Table 3.

7.3. Analysis of large deformation behaviour

This well-documented three-dimensional example examines the capability of the SPH algorithm in the large strain regime. Initially proposed by [64], it was later extensively explored in References [1,60,66], primarily for hyperelastic models. In this study, we extend the benchmark to include viscoelasticity models, aiming to demonstrate that the proposed SPH algorithm remains free from hourglassing modes, which commonly observed in this test case. A short column of length $L = 6$ m with a unit square cross section is subjected to an initial sinusoidal velocity field about the origin, given by

$$\boldsymbol{v}\Big|_{t=0} = \begin{bmatrix} 0 \\ \Omega_0 \sin\left(\frac{\pi Y}{2L}\right) \\ 0 \end{bmatrix} [\text{m/s}], \tag{85}$$

where $\Omega_0 = 105$ ms^{-1} represents the velocity amplitude (see Figure 2c of Reference [67]). The relevant material properties are provided in Table 4.

The accuracy of the SPH algorithm for viscoelasticity is assessed through a particle refinement study using [M1] 625, [M2] 1715, and [M3] 3969 particles. Fig. 10 shows that the deformations predicted by the proposed SPH algorithm (first three columns) converge with increasing particle refinement and are in good agreement with results from the URL-SPH algorithm [3] and the in-house vertex-centred FVM [4,5,48]. Similar deformation patterns (top view) are observed for both Total Lagrangian SPH and URL-SPH schemes (see Fig. 11). For completeness, Fig. 12 shows the evolution of the accumulated twist angle at four positions: $\boldsymbol{X}_A = [-0.5, 6, -0.5]^T$ m, $\boldsymbol{X}_B = [0.5, 6, -0.5]^T$ m, $\boldsymbol{X}_C = [0.5, 6, 0.5]^T$ m, and $\boldsymbol{X}_D = [-0.5, 6, 0.5]^T$ m. The results show near-identical behaviour when comparing the proposed SPH algorithm with the URL-SPH scheme. It is important to assess how energy is transferred throughout the simulation process. This is seen in Fig. 13(a) and (b). At time $t = 0$, the total energy of the structure is primarily kinetic, which is governed by the initial twisting velocity. As the column twists, kinetic energy is progressively converted into strain energy, with some energy

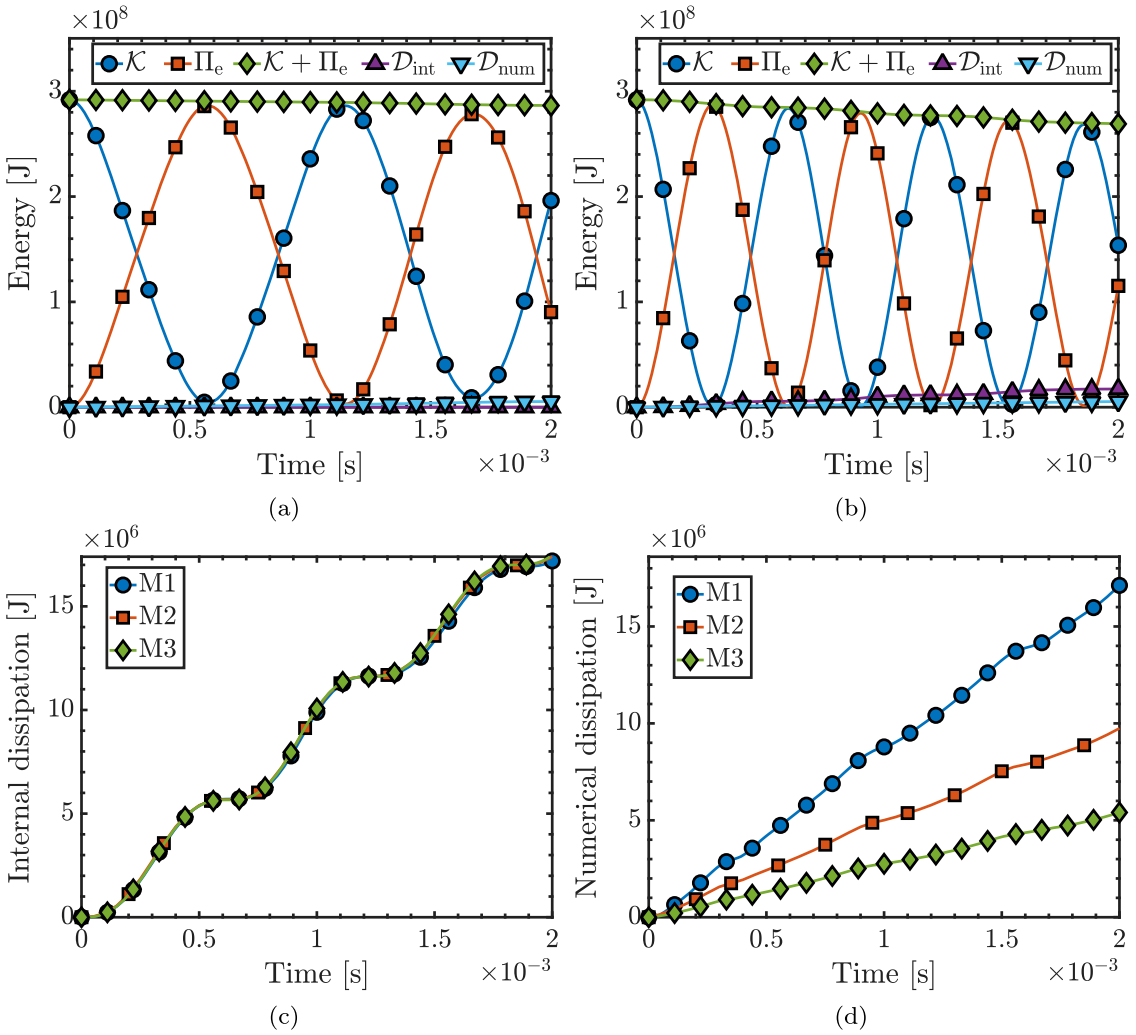

Fig. 8. Tensile test. Time evolution of various energy measures with discretisation M3, including kinetic energy $\mathcal{K}$, strain energy Π_e, the total energy (summation of kinetic and strain energies), internal viscous dissipation $\mathcal{D}_{int}$, and numerical dissipation $\mathcal{D}_{num}$. These are presented for (a) hyperelastic model and (b) compressible viscoelastic model. Time histories of (c) internal viscous dissipation and (d) numerical dissipation for varying particle refinements. Material properties are provided in Table 3.

irrecoverably dissipated due to material viscosity (absent in the hyperelastic model) and a small portion dissipated as numerical dissipation. Once the column reaches its maximum tensile twist, kinetic energy is zero, and strain energy dominates. During the reverse twist, energy again transitions among strain energy, kinetic energy, material viscous dissipation, and numerical dissipation. For the viscoelastic model, material viscous dissipation increases over time, as shown in Fig. 13(c). Furthermore, Fig. 13(d) illustrates that the proposed algorithm introduces numerical dissipation over the duration of the simulation, ensuring the discrete satisfaction of the second law of thermodynamics. The numerical dissipation consistently decreases as the number of particle increases. Finally, Fig. 14 presents a series of deformed states via compressible viscoelasticity, with the pressure profile indicated by the colour contour plot. No instabilities are observed.

7.4. Performance in thin-walled structures

7.4.1. Bending of a thin plate

The bending behaviour of a thin structure is examined to verify that the proposed SPH algorithm circumvents the usual locking difficulties in simulating thin structure. The thin plate (see Figure 18 of Reference [27]) is subjected to an initial velocity profile given

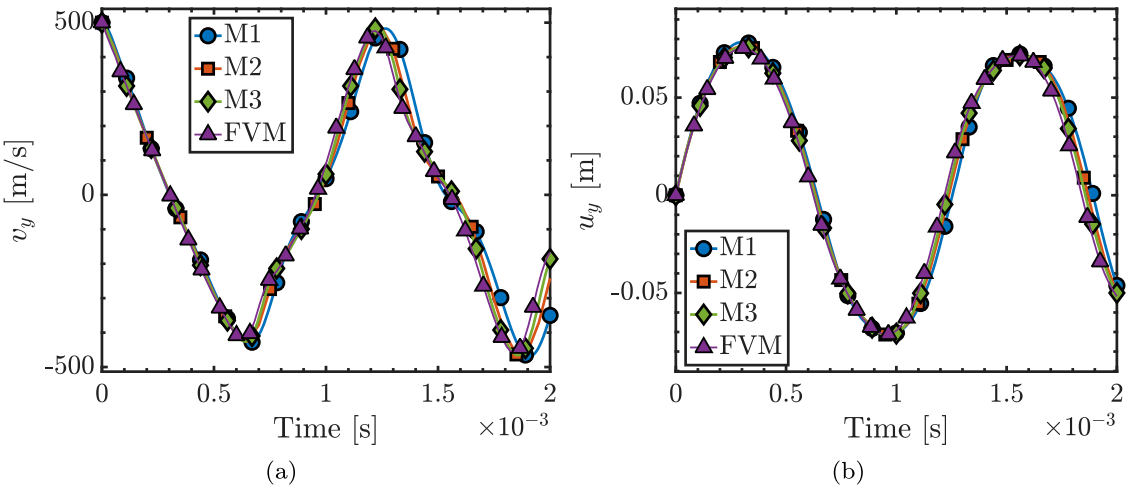

Fig. 9. Tensile test. Time history for (a) vertical velocity v_y and (b) vertical displacement u_y at position $\boldsymbol{X} = [1, 1]^T$ m. Material properties are provided in Table 3.

Table 5
Material properties for a thin plate.

Equilibrium (long-term) Mooney-Rivin model		
Young's modulus [kPa]	E	50.5
Material density [kg/m^3]	ρ_R	1100
Poisson's ratio	ν	0.3
Parameters [Pa]	$\{\xi, \zeta\}$	$\{\mu/2, 0\}$
Non-equilibrium viscous model		
Number of Maxwell branch	n_{M}	1
Proportionality factor	β_1	1
Relaxation time [s]	τ_1	0.02

by the following expression

$$\boldsymbol{v}\Big|_{t=0} = \alpha_1(\boldsymbol{X}) \begin{bmatrix} 0 \\ 0 \\ 1 \end{bmatrix} [\mathrm{m/s}]; \qquad \alpha_1(\boldsymbol{X}) = \sqrt{\frac{2}{\pi}} \left[\exp\left(-\frac{(X-5)^2}{10} \right) + \exp\left(-\frac{(Y-5)^2}{10} \right) \right]. \tag{86}$$

A compressible viscoelasticity model is adopted, with material parameters detailed in Table 5.

To demonstrate particle convergence, three progressively refined models are used: [M1] 867, [M2] 1875 and [M3] 4107 particles. The first three columns of Fig. 15 compare the deformation process of the structure at times $t = 1.5$ s and $t = 4.5$ s using these models. For comparison, the problem is also tested using the mixed-based URL-SPH algorithm [3] with the M3 discretisation. The deformed shape and pressure field remain consistent across all three models using the proposed SPH algorithm and closely match the results from the URL-SPH algorithm. Fig. 16(a) presents the time history of the linear momentum components within the system, showing that linear momentum components are conserved during spatial translation. Since this problem is primarily governed by translation motion, some of the kinetic energy is converted into strain energy, whilst the rest is irreversibly lost due to material and numerical dissipation. This loss is reflected in the decrease in global total energy, as shown in Fig. 16(b). To satisfy the second law of thermodynamics, both material viscous dissipation and numerical dissipation (introduced by the SPH algorithm) increase consistently over time. These are illustrated in Fig. 16(c) and (d). The results obtained using the proposed algorithm are nearly indistinguishable from those of the URL-SPH algorithm, demonstrating strong agreement between the two approaches.

Furthermore, the importance of numerical dissipation, even when using viscoelasticity, is demonstrated in Fig. 17. To highlight this, we first run the same problem using both the hyperelastic model ($\beta_1 = 0$) and the viscoelastic model, with no numerical dissipation in either case. Pressure checkerboarding and incorrect deformation paths are observed in the third and fourth columns. These issues are mitigated by the proposed algorithm with entropy-stable stabilisation, which shows excellent agreement with the URL-SPH results. Finally, Fig. 18 illustrates the time evolution of the plate deformation[15], highlighting smooth pressure variations. Top and bottom views of the deformed structures are also presented in Fig. 19. It is remarkable to see how well the deformation behaviour of the structure is captured.

[15] Self-contact is expected to occur at later times (when $t > 6$ s), but this is beyond the scope of the present study.

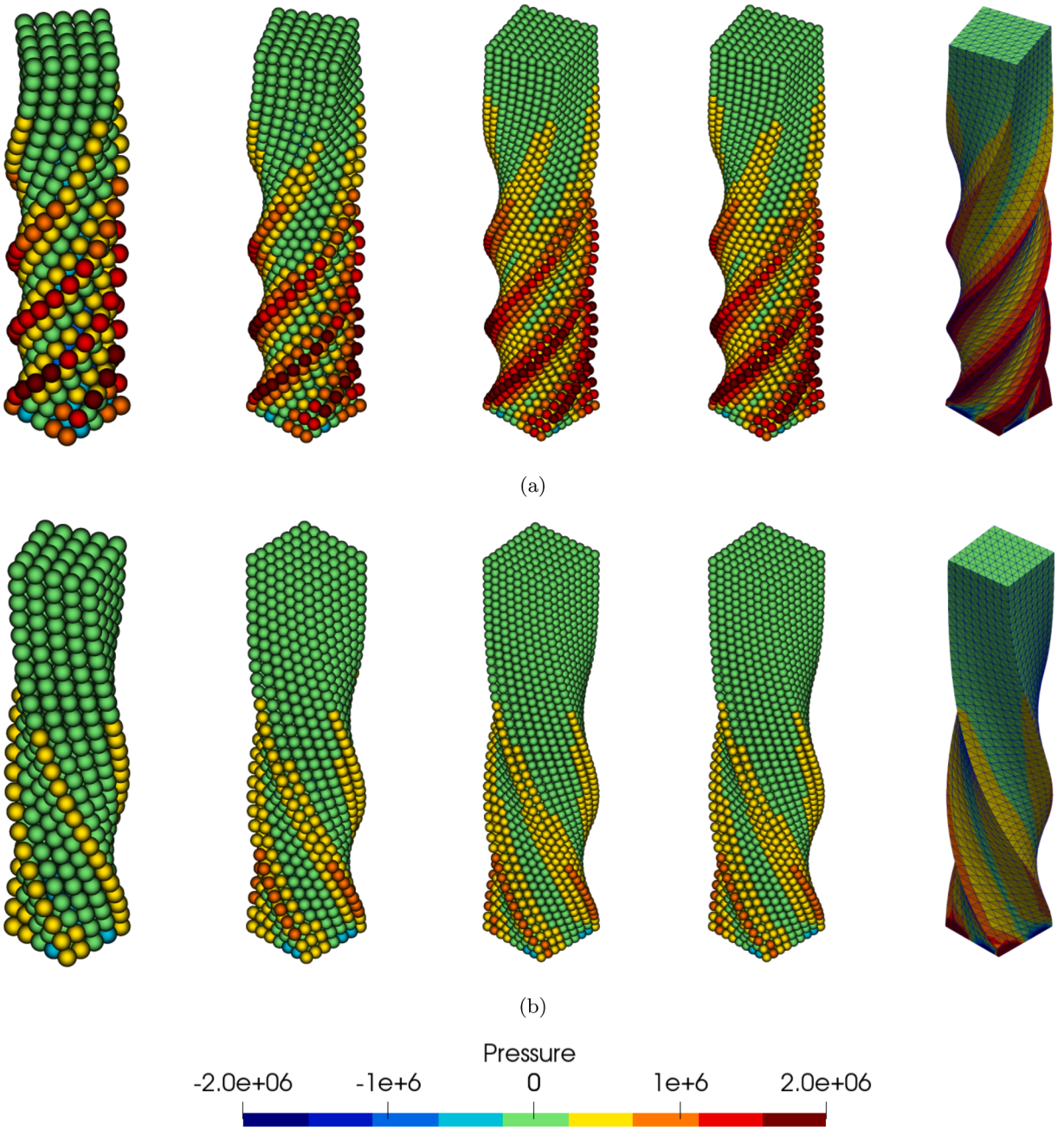

Fig. 10. Twisting column. Comparison of deformed shapes using compressible viscoelasticity at (a) $t = 0.085$ s and (b) $t = 0.26$ s. The first three columns (left to right) show the particle refinement of a structure simulated using the proposed SPH algorithm. The fourth column (second from the right) shows results from an alternative in-house URL-SPH algorithm [3], and the last column (on the right) shows results from the vertex-centred FVM [4]. Colour indicates the pressure profile. Material properties are summarised in Table 4.

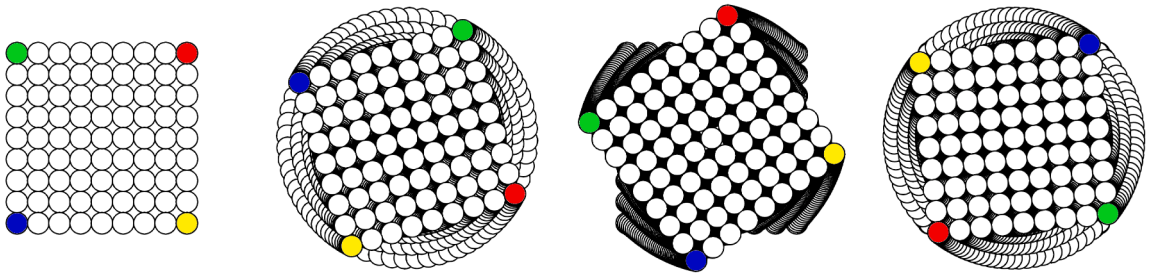

(a) Proposed Total Lagrangian SPH scheme

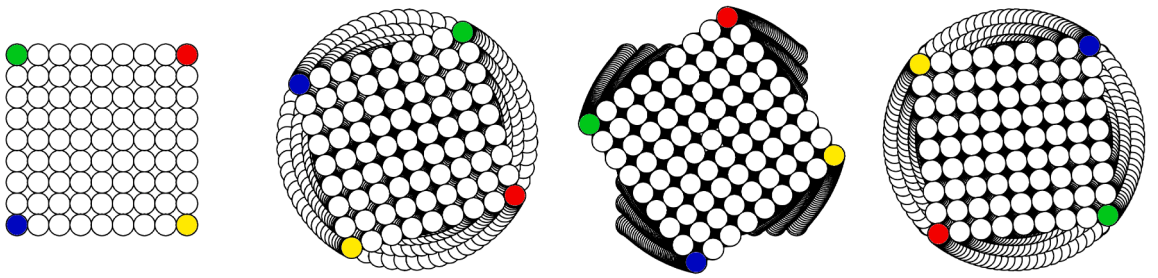

(b) Alternative Updated Reference Lagrangian SPH scheme

Fig. 11. Twisting column. A sequence of deformation states from the top view using (a) the proposed SPH scheme, and (b) URL-SPH scheme at times $t = \{0, 0.085, 0.17, 0.26\}$ s. The colour represents the particle positions. The material parameters are provided in Table 4.

Table 6
Material properties for a cylindrical structure.

Equilibrium (long-term) Mooney-Rivin model		
Young's modulus [GPa]	E	5.56
Material density [kg/m^3]	ρ_R	1000
Poisson's ratio	ν	0.3
Parameters [Pa]	$\{\xi, \zeta\}$	$\{\mu/2, 0\}$
Non-equilibrium viscous model		
Number of Maxwell branch	n_{M}	1
Proportionality factor	β_1	1
Relaxation time [s]	τ_1	0.02

7.4.2. Pinched cylindrical structure

The final example considered in this paper is a pinched cylindrical structure, a benchmark problem [68–70] often studied under quasi-static conditions. The deformation process may involve the formation of wrinkles, which typically requires high-order schemes for accurate capture. The cylinder (see Fig. 20) has a radius $R = 10$ m, length $L = 20$ m, and thickness $t = 0.1$ m. It is subjected at point A to a pair of symmetrical radial pinching velocities $\boldsymbol{v}_A$[16], defined by a Gaussian profile as

$$\boldsymbol{v}_A(t) = \begin{bmatrix} v_x(t) \\ 0 \\ 0 \end{bmatrix} [\mathrm{m/s}]; \qquad v_x(t) = -\frac{a_1}{a_2\sqrt{2\pi}} \exp\left[-\frac{(t-t_0)^2}{2a_2^2}\right], \tag{87}$$

where the parameters $a_1 = 0.075$ m, $a_2 = 5 \times 10^{-4}$ s, and $t_0 = 2 \times 10^{-3}$ s. The cylinder ends are closed with rigid diaphragms, restricting displacement to the y-direction. Due to symmetry, only one-eighth of the geometry is modelled using 2583 particles. Fig. 21 illustrates that the temporal evolution of velocities and displacements at points B and C is in good agreement with the URL-SPH solution. The deformed shapes obtained from both methods also match closely, and the pressure profiles remain stable without spurious modes, as shown in Figs. 22 and 23. These results demonstrate that the proposed SPH scheme is robust and provides a compelling alternative for analysing the deformation of thin-walled structures.

[16] Since the focus here is on dynamic inertial effects, we slightly modify the problem by driving it with prescribed velocities rather than boundary forces.

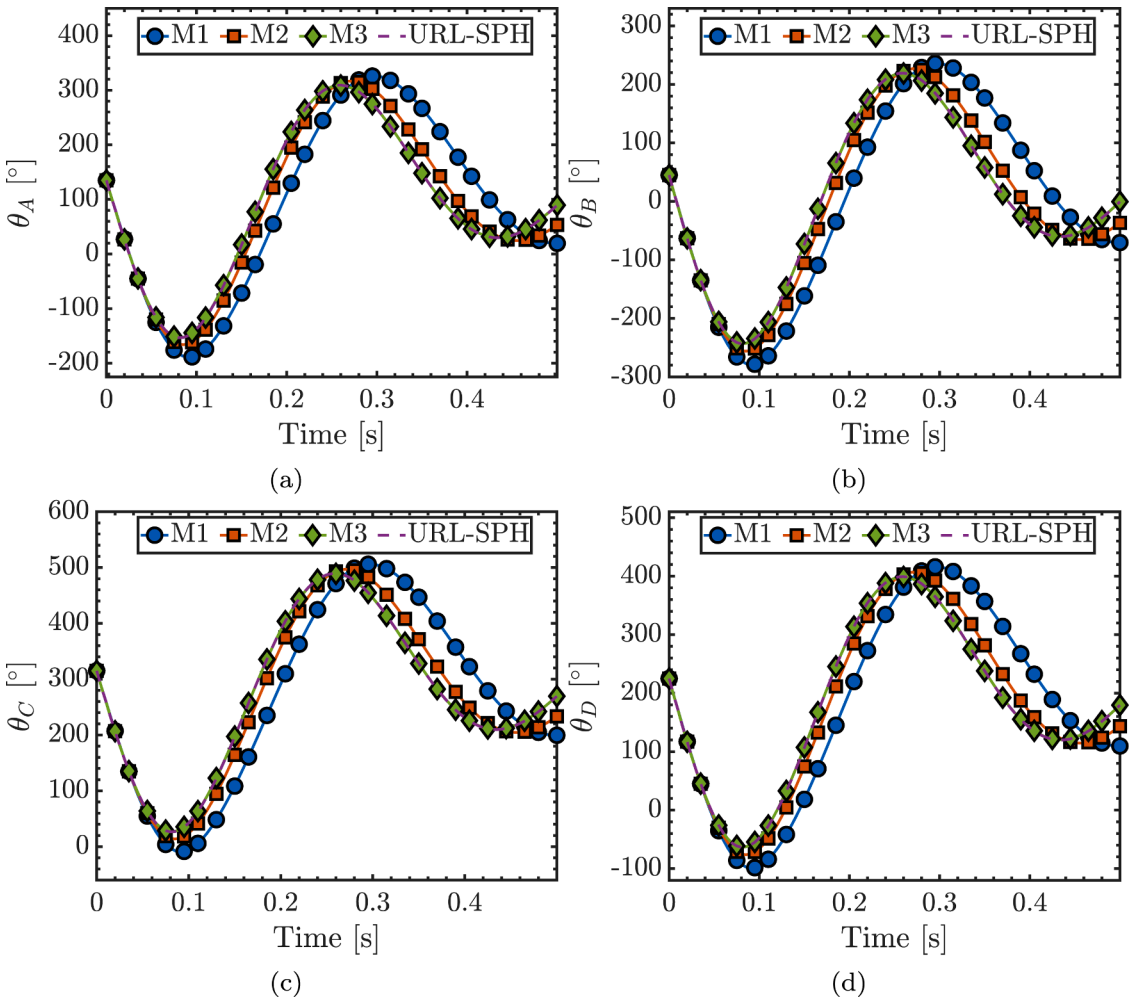

Fig. 12. Twisting column. Time history of the accumulated twist angle via different discretisation at four locations, namely (a) θ_A at $\boldsymbol{X}_A = [-0.5, 6, -0.5]^T$ m, (b) θ_B at $\boldsymbol{X}_B = [0.5, 6, -0.5]^T$ m, (c) θ_C at $\boldsymbol{X}_C = [0.5, 6, 0.5]^T$ m, and (d) θ_D at $\boldsymbol{X}_D = [-0.5, 6, 0.5]^T$ m. Compressible viscoelasticity model is used. The relevant material parameters are tabulated in Table 4.

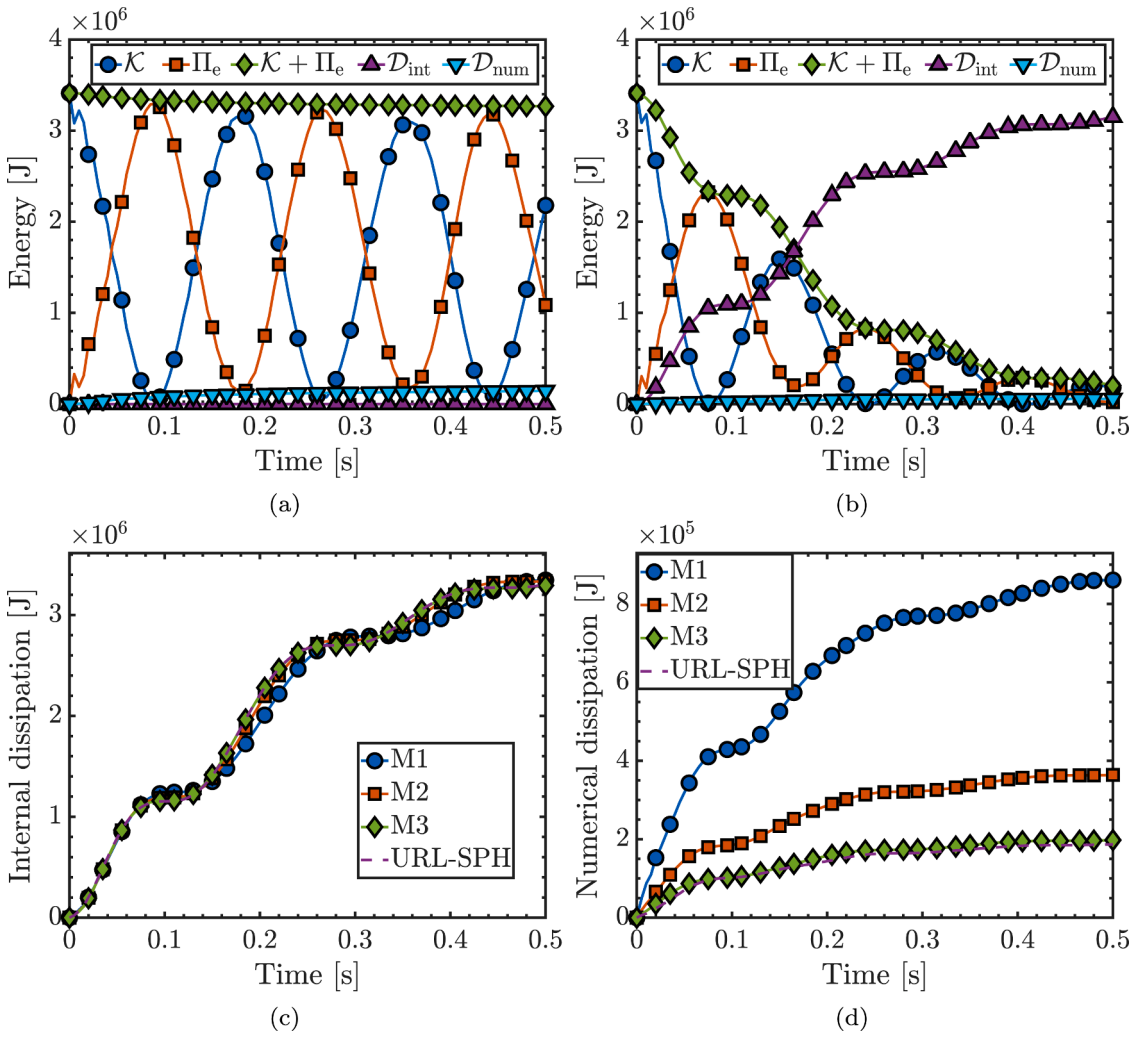

Fig. 13. Twisting column. Time evolution of various energy measures with discretisation M3, including kinetic energy $\mathcal{K}$, strain energy Π_e, the total energy (summation of kinetic and strain energies), internal viscous dissipation $\mathcal{D}_{int}$, and numerical dissipation $\mathcal{D}_{num}$. These are presented for (a) hyperelastic model and (b) the compressible viscoelasticity. Time histories of (c) internal viscous dissipation and (d) numerical dissipation for varying particle refinements. Material properties are provided in Table 4.

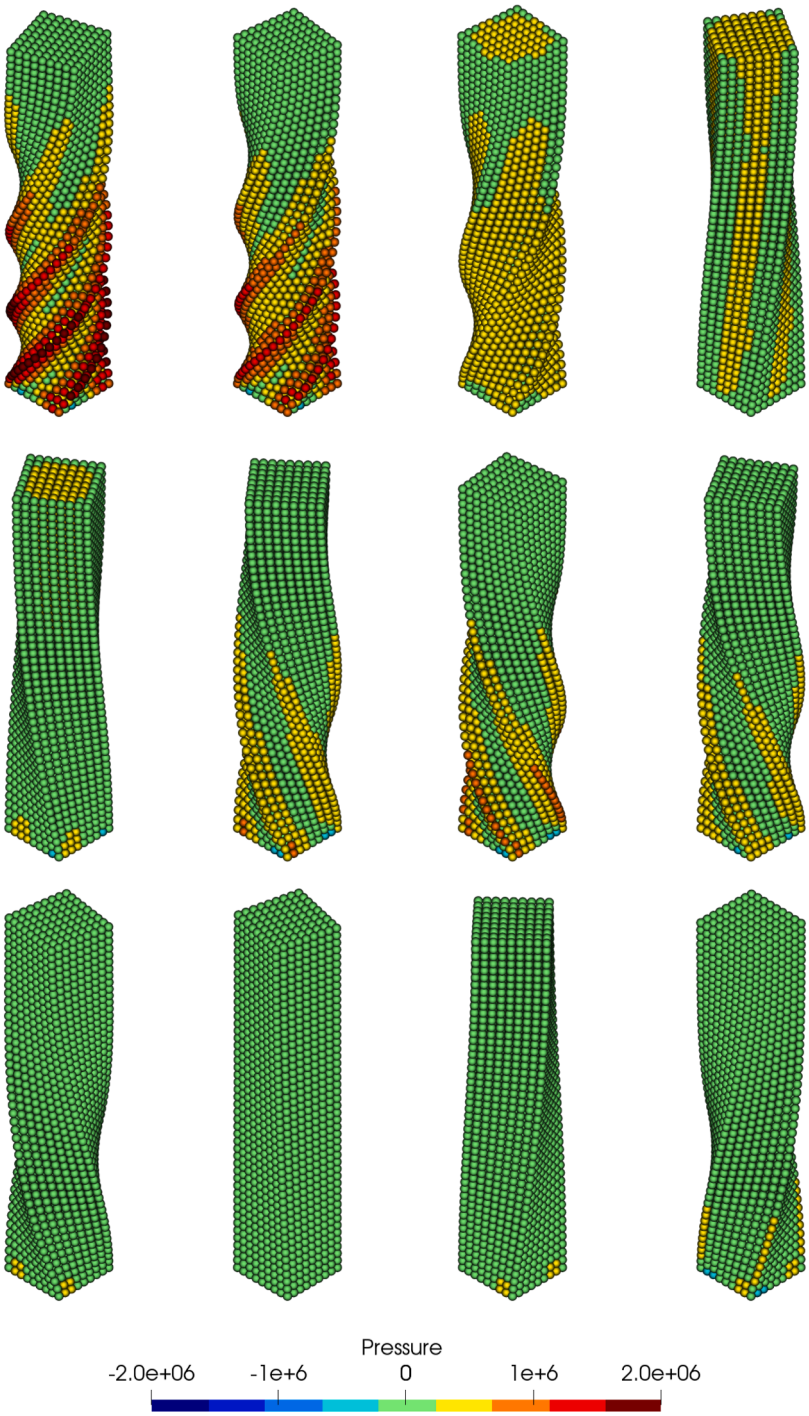

Fig. 14. Twisting column. A sequence of deformed structures with pressure distribution at times $t = \{85, 105, 135, 165, 195, 225, 255, 285, 315, 345, 375, 405\}$ ms (from left to right and top to bottom), respectively. Results obtained using a compressible viscoelastic model with M3 model. Material properties are summarised in Table 4.

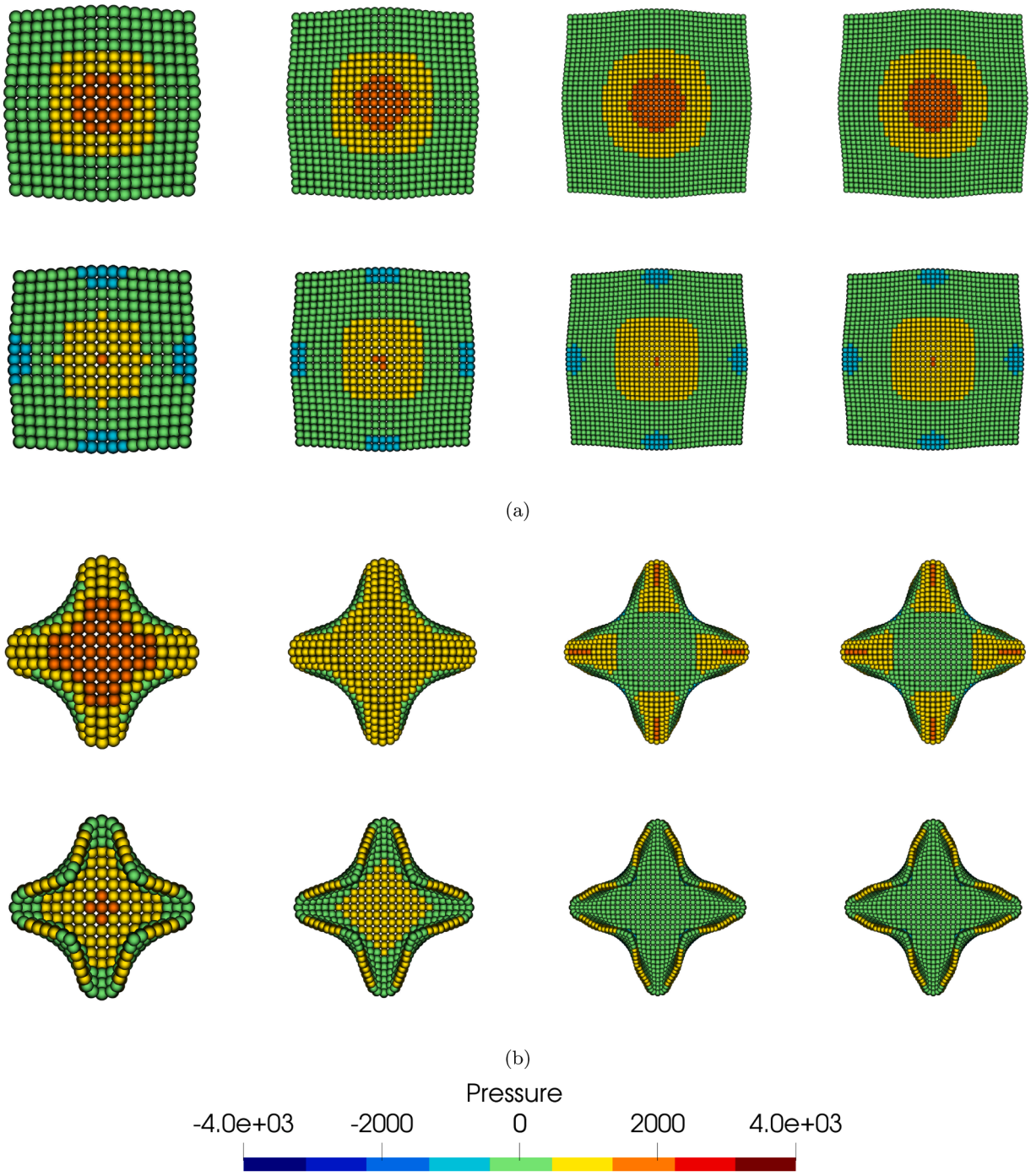

Fig. 15. Bending of a thin plate. Comparison of deformed shapes at (a) $t = 1.5$ s and (b) $t = 4.5$ s. In (a), the top row represents the top view, and the bottom row represents the bottom view. The same applies to (b). The first three columns (from left to right) show the particle refinement of a structure simulated using the proposed SPH algorithm, whereas the last column (rightmost) presents results from an alternative in-house Updated Reference Lagrangian SPH algorithm [3]. Colour indicates the pressure profile. Material properties are summarised in Table 5.

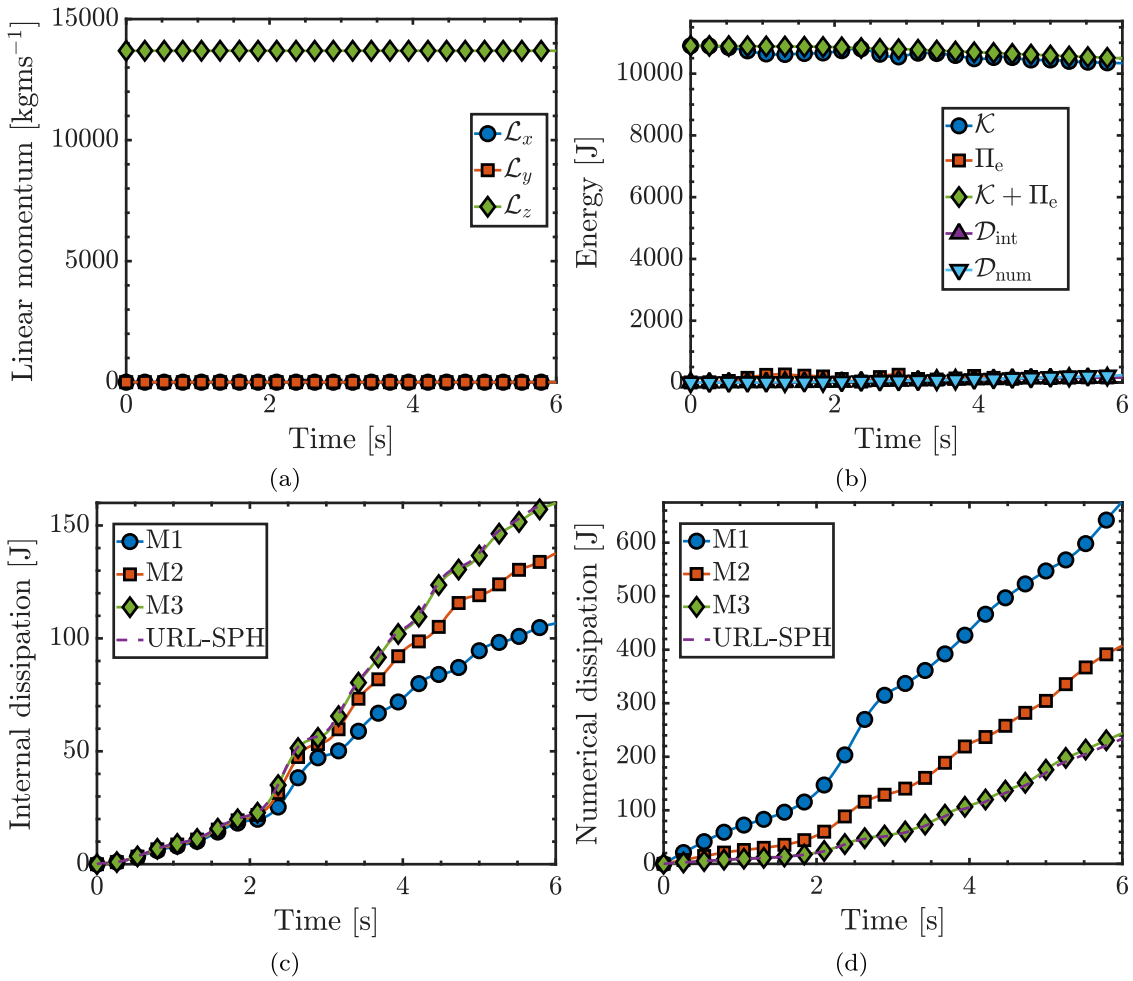

Fig. 16. Bending of a thin plate. (a) Time evolution of the linear momentum components within the system with discretisation M3. (b) Time evolution of various energy measures with discretisation M3, including kinetic energy $\mathcal{K}$, strain energy Π_e, the total energy (summation of kinetic and strain energies), internal viscous dissipation $\mathcal{D}_{int}$, and numerical dissipation $\mathcal{D}_{num}$. Time histories of (c) internal viscous dissipation and (d) numerical dissipation for varying particle refinements. Material properties are provided in Table 5.

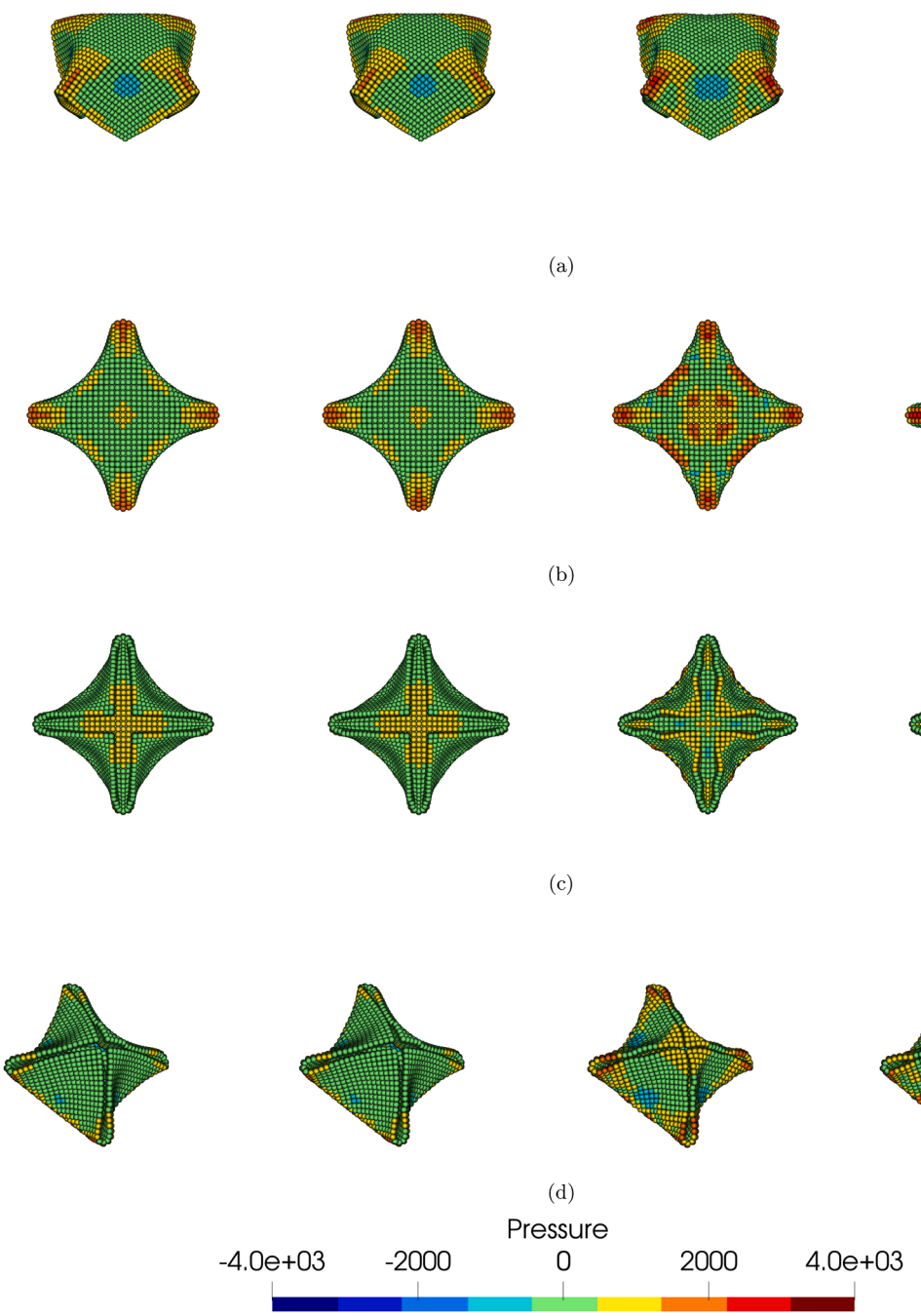

Fig. 17. Bending of a thin plate. Comparison of deformed shapes at (a) $t = 4.5$ s (side view), (b) $t = 5$ s (top view), (c) $t = 5.5$ s (bottom view), and (d) $t = 6$ s (slanted view). The first column shows results using the proposed SPH algorithm, the second column presents the URL-SPH algorithm, the third column shows the hyperelastic model ($\beta_1 = 0$) with no numerical dissipation, and the fourth column presents the viscoelastic model ($\beta_1 = 1$) without numerical dissipation. Colour indicates the pressure profile. Material properties are provided in Table 5.

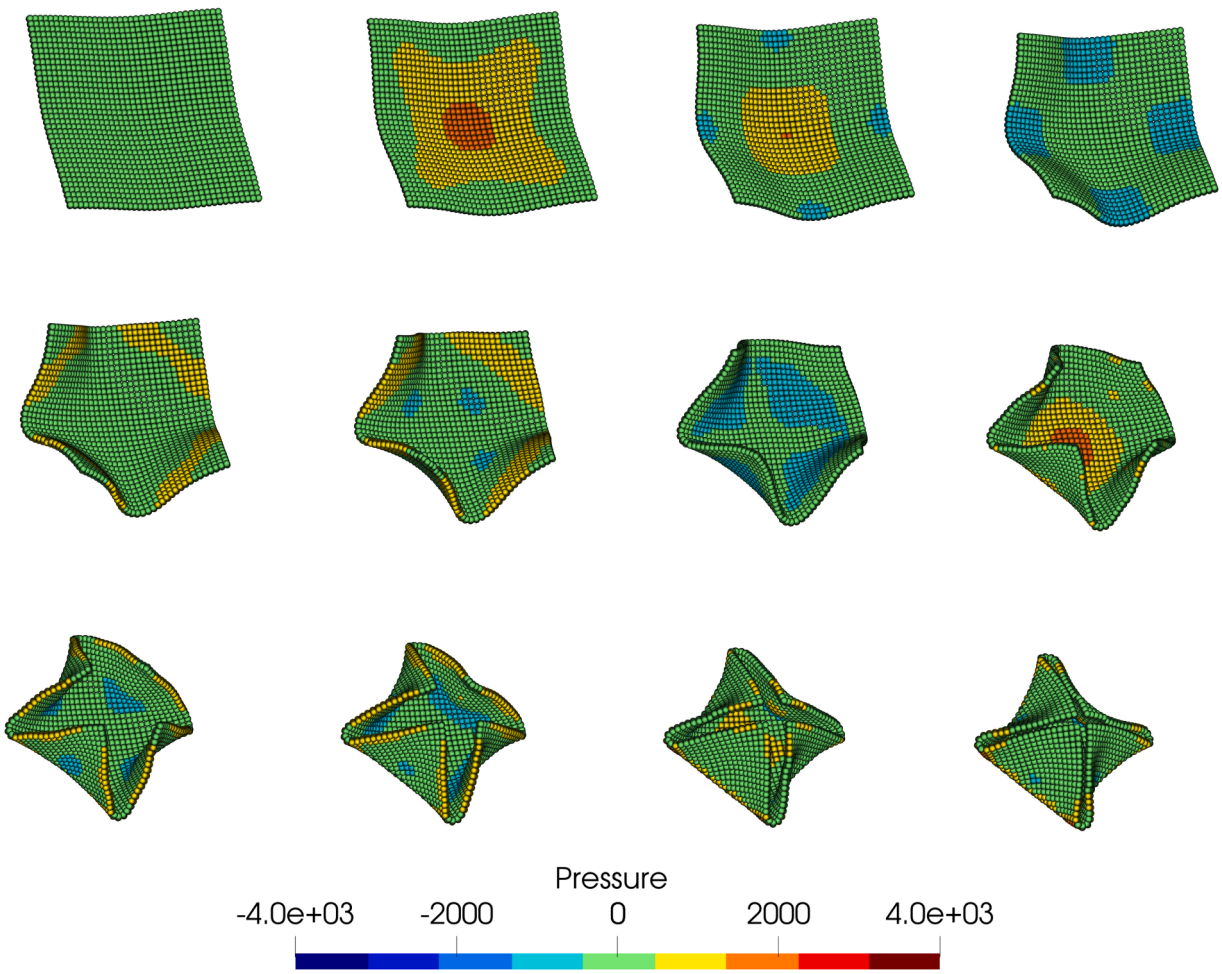

Fig. 18. Bending of a thin plate. A sequence of deformed plate shapes in a 3D slanted view with pressure distribution at times $t = \{0.5, 1, 1.5, 2, 2.5, 3, 3.5, 4, 4.5, 5, 5.5, 6\}$ s (from left to right, top to bottom). Results are obtained using a compressible viscoelastic model with the M3 model. Material properties are summarised in Table 5.

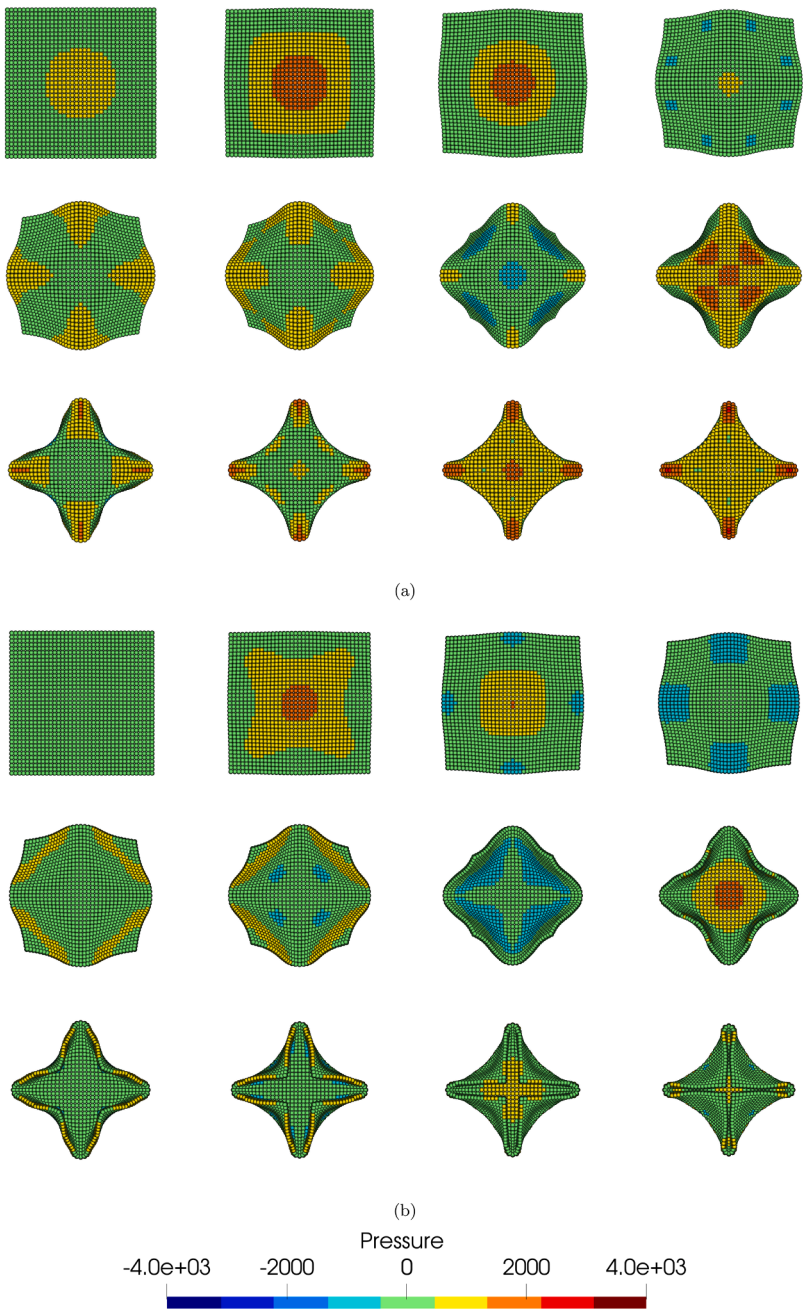

Fig. 19. Bending of a thin plate. A sequence of deformed plate shapes in (a) top view and (b) bottom view, with pressure distribution at times $t = \{0.5, 1, 1.5, 2, 2.5, 3, 3.5, 4, 4.5, 5, 5.5, 6\}$ s (from left to right, top to bottom). Results are obtained using a compressible viscoelastic model with the M3 model. Material properties are summarised in Table 5.

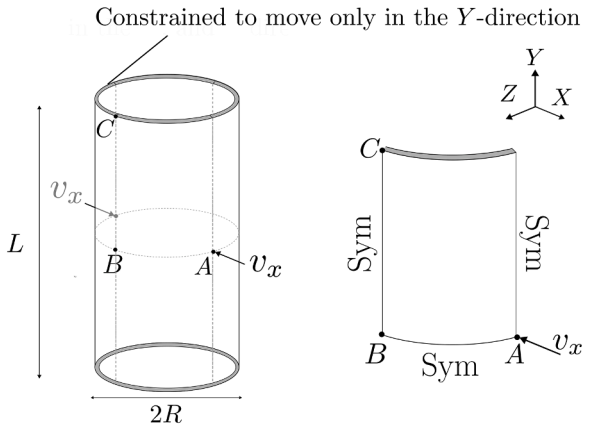

Fig. 20. (Left) Cylindrical structure pinched with radial velocity v_x. (Right) Only one-eighth of the structure is modelled due to symmetry.

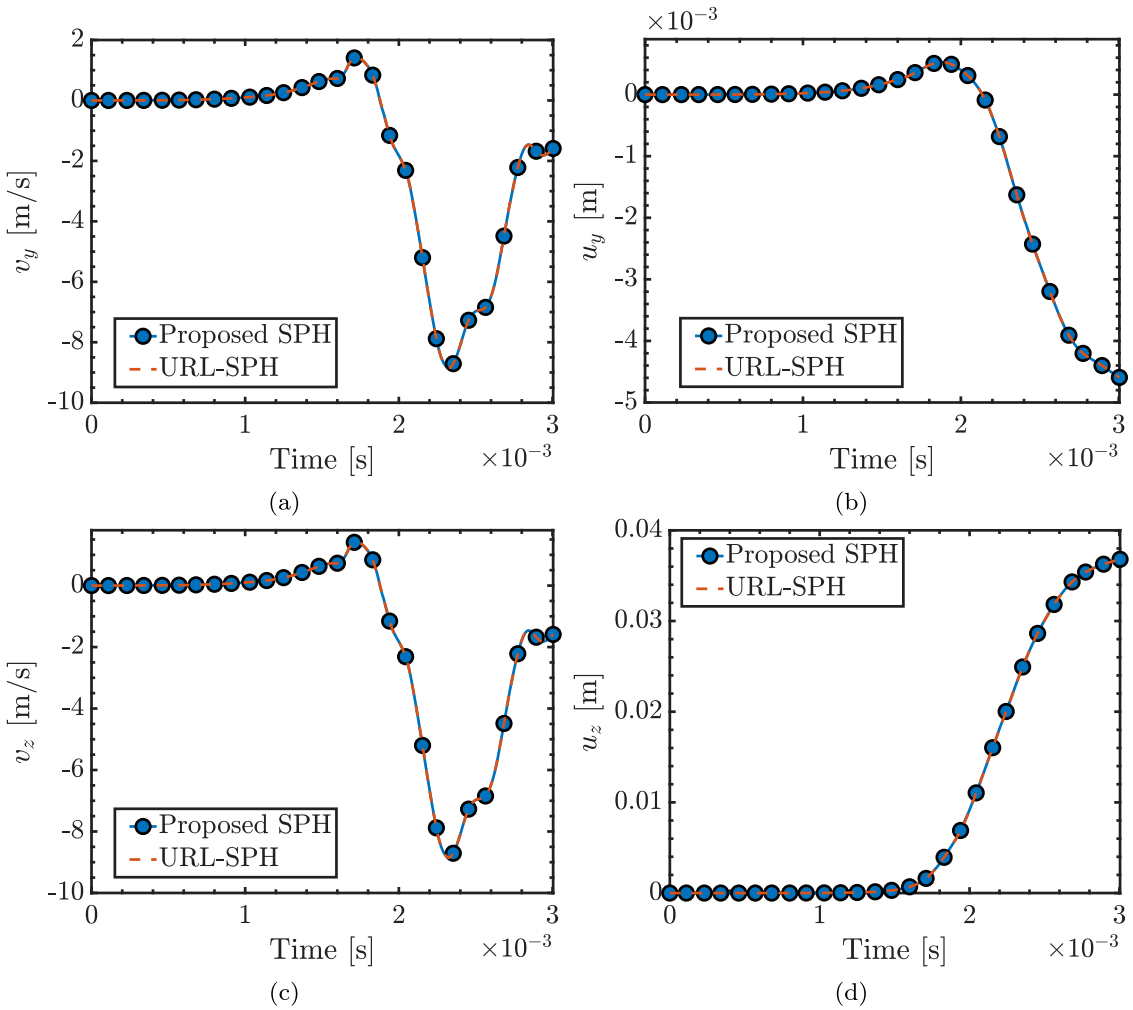

Fig. 21. Pinched cylindrical structure. Time histories of vertical and radial responses of the cylindrical structure: (a) vertical velocity v_y and (b) vertical displacement u_y at position C, and (c) radial velocity v_z and (d) radial displacement u_z at position B. Material properties are summarised in Table 6.

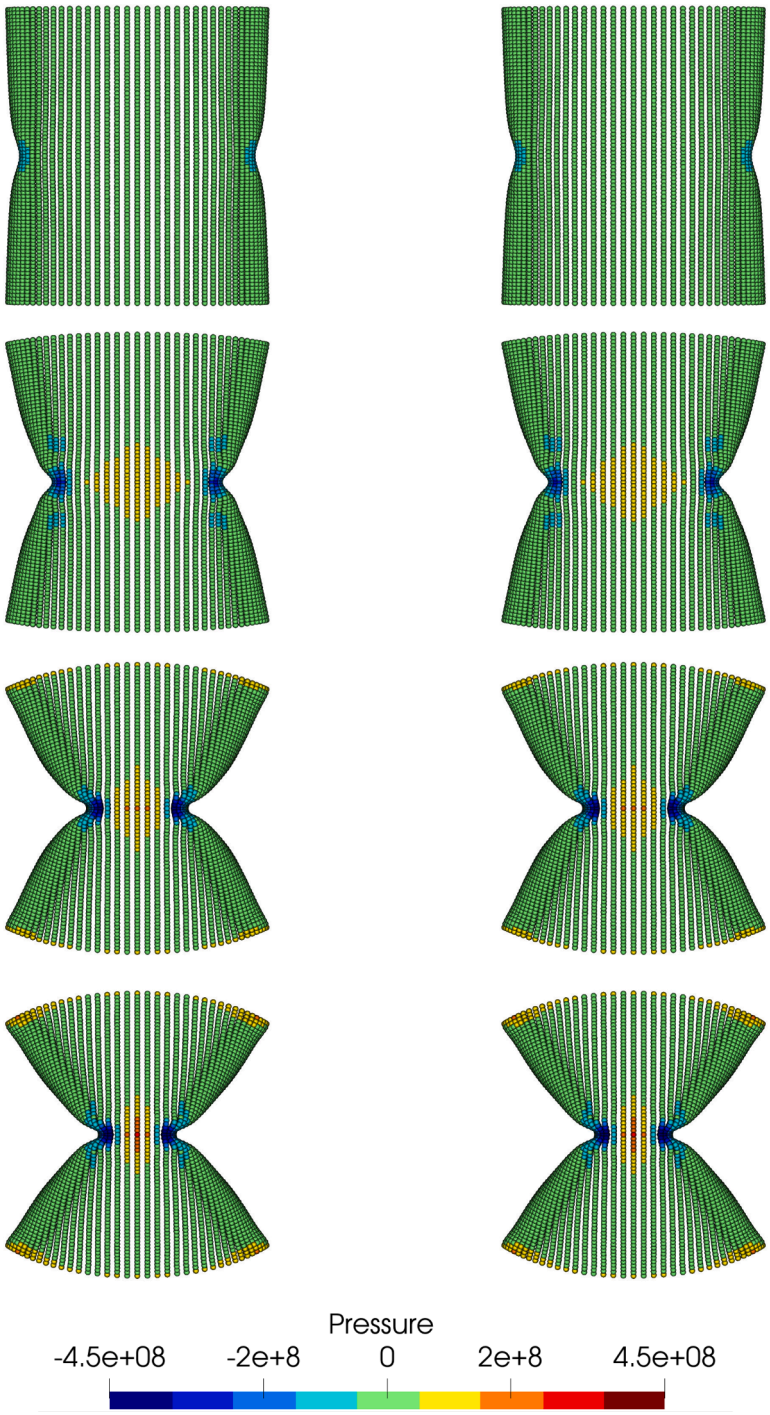

Fig. 22. Cylindrical structure. A sequence of deformed shapes in the X-Y view with pressure distribution at times $t = \{1.5, 2, 2.5, 3\}$ ms (from top to bottom). The left column shows results from the proposed SPH algorithm, and the right column displays the corresponding URL-SPH solutions. Material properties are summarised in Table 6.

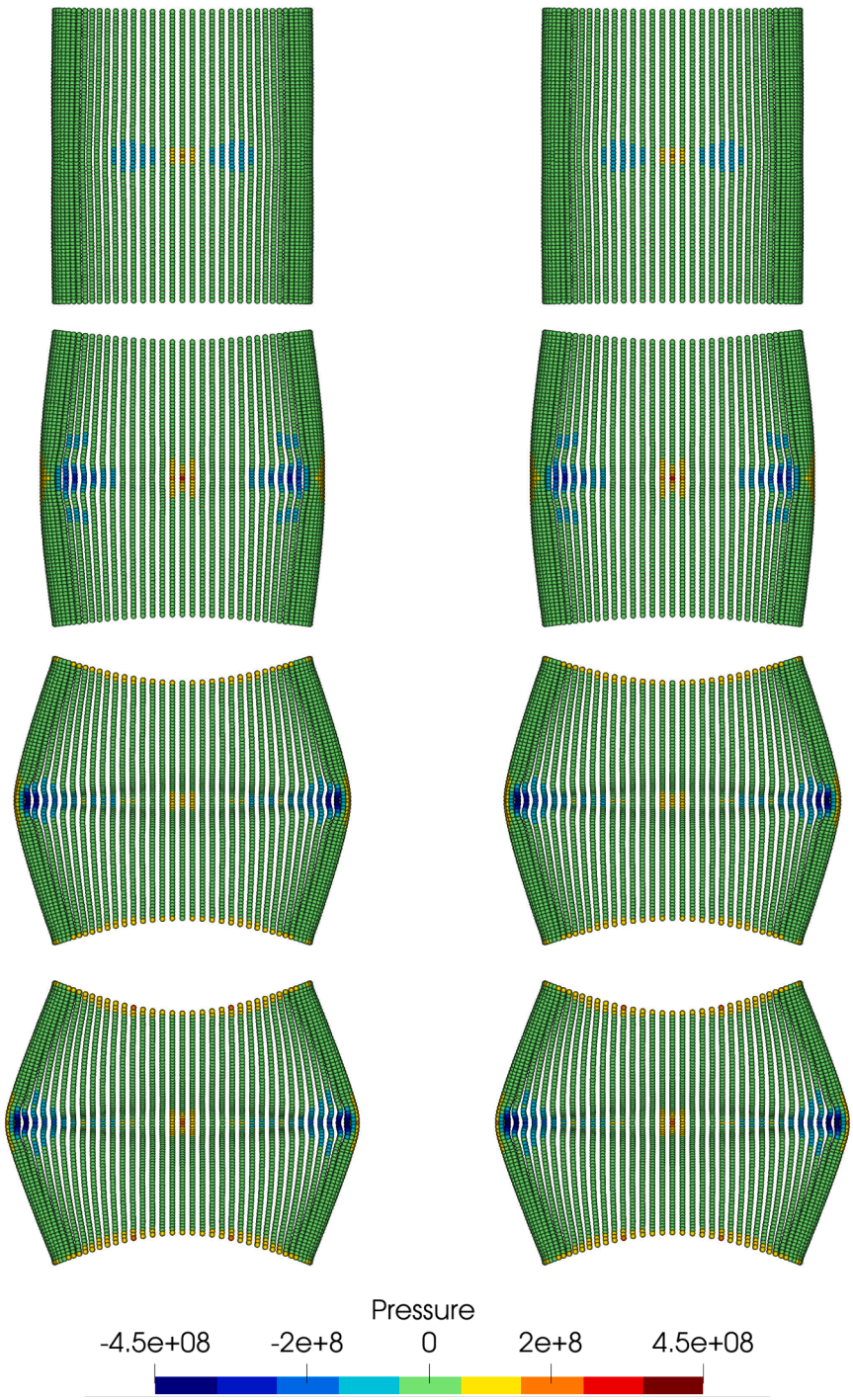

Fig. 23. Cylindrical structure. A sequence of deformed shapes in the Y-Z view with pressure distribution at times $t = \{1.5, 2, 2.5, 3\}$ ms (from top to bottom). The left column shows results from the proposed SPH algorithm, and the right column displays the corresponding URL-SPH solutions. Material properties are summarised in Table 6.

8. Conclusions

This paper has presented a first-order hyperbolic framework for large strain viscoelastic solids, incorporating relaxation terms to model internal dissipation. A key objective was to guarantee hyperbolicity, ensuring real wave speeds across all deformation states. To achieve this, we introduced a convex generalised entropy function, which required a multi-variable strain energy function jointly convex with respect to the deformation measures $\boldsymbol{\mathcal{X}} = \{\boldsymbol{F}, \boldsymbol{H}, J\}$ and the extended set of internal variables $\boldsymbol{\mathcal{Y}} = \{\boldsymbol{Y}_1, y_1, \boldsymbol{Y}_2, y_2, \dots, \boldsymbol{Y}_{n_\mathrm{M}}, y_{n_\mathrm{M}}\}$, where n_M is the total number of Maxwell branches. This enabled symmetrisation of the first-order hyperbolic conservation laws with relaxation terms, leading to a thermodynamically consistent and well-posed formulation. The hyperbolicity and relaxation properties were analysed via the eigenproblem, yielding nonlinear expressions for the pressure and shear wave speeds.

The hyperbolic framework was implemented within an upwinding Smoothed Particle Hydrodynamics (SPH) scheme. The SPH algorithm ensured semi-discrete satisfaction of the second law of thermodynamics, with internal and numerical dissipation monitored separately through the time rate of the generalised convex entropy. Several benchmark problems, including a manufactured solution, demonstrated that the SPH method produced accurate, consistent, and stable results, capturing deformation, energy transfer, and dissipation processes whilst maintaining stable pressure fields and avoiding spurious modes. Comparisons with an in-house Updated Reference Lagrangian SPH algorithm showed excellent agreement, confirming the robustness and reliability of the approach. These findings highlight the effectiveness of the proposed method, particularly for thin-walled structures where wrinkling and large strain effects are significant. Future work will extend the current framework to consider fully incompressible viscoelasticity and incorporate thermal effects.

CRediT authorship contribution statement

Chun Hean Lee: Writing – original draft, Validation, Methodology, Conceptualization; **Antonio J. Gil:** Writing – review & editing, Methodology, Conceptualization; **Tadas Jaugielavičius:** Writing – review & editing, Validation; **Thomas Richardson:** Writing – review & editing, Validation; **Sébastien Boyaval:** Writing – review & editing, Conceptualization; **Damien Violeau:** Writing – review & editing; **Javier Bonet:** Writing – review & editing, Conceptualization.

Data availability

Data will be made available on request.

Declaration of competing interest

The authors declare that they have no known competing financial interests or personal relationships that could have appeared to influence the work reported in this paper.

Acknowledgements

CHL and TJ acknowledge support provided by FIFTY2 Technology GmbH (project 322835), AJG and TR from UK AWE (project PO 40062030), and JB from project POTENTIAL (PID2022-141957OB-C21) funded by MCIN/AEI/10.13039/501100011033/FEDER, UE. AJG also acknowledges support from The Leverhulme Trust Fellowship, and CHL acknowledges support from the RSE Personal Research Fellowship.

Appendix A. Conjugate stresses and Hessian operators

Based on the polyconvex energy functions defined in (19) and (20), the thermodynamic conjugate stresses corresponding to the equilibrium and non-equilibrium components are given by

$$\begin{aligned} &\boldsymbol{\Sigma}^{\infty}_{\boldsymbol{F}}(\boldsymbol{\mathcal{X}}) = 2\xi\boldsymbol{F}; \qquad \boldsymbol{\Sigma}^{\infty}_{\boldsymbol{H}}(\boldsymbol{\mathcal{X}}) = 2\zeta\boldsymbol{H}; \qquad \Sigma^{\infty}_{J}(\boldsymbol{\mathcal{X}}) = -\frac{2(\xi+2\zeta)}{J} + \hat{\lambda}(J-1) = f'_{\infty}; \\ &\boldsymbol{\Sigma}^{\alpha}_{\boldsymbol{F}}(\boldsymbol{\mathcal{X}}, \boldsymbol{\mathcal{Y}}_\alpha) = \mu_\alpha \boldsymbol{F}\boldsymbol{Y}_\alpha^{-1}; \qquad \boldsymbol{\Sigma}^{\alpha}_{\boldsymbol{H}}(\boldsymbol{\mathcal{X}}, \boldsymbol{\mathcal{Y}}_\alpha) = \boldsymbol{0}; \qquad \Sigma^{\alpha}_{J}(\boldsymbol{\mathcal{X}}, \boldsymbol{\mathcal{Y}}_\alpha) = -\frac{\mu_\alpha}{J}. \end{aligned} \tag{A.1}$$

The corresponding thermodynamic conjugate stresses with respect to the internal variables are

$$\boldsymbol{\Sigma}_{\boldsymbol{Y}_\alpha} = -\frac{\mu_\alpha}{2}\boldsymbol{Y}_\alpha^{-1}\boldsymbol{C}\boldsymbol{Y}_\alpha^{-1}; \qquad \Sigma_{y_\alpha} = -\frac{\mu_\alpha}{2}y_\alpha^{-1}. \tag{A.2}$$

For consistent linearisation and stability analysis, the diagonal components of the long-term (equilibrium) Hessian $[\mathbb{H}^{\infty}_{W}]$ are computed as

$$W^{\infty}_{\boldsymbol{F}\boldsymbol{F}} = 2\xi\boldsymbol{\mathcal{I}}; \qquad W^{\infty}_{\boldsymbol{H}\boldsymbol{H}} = 2\zeta\boldsymbol{\mathcal{I}}; \qquad W^{\infty}_{JJ} = \hat{\lambda} + \frac{2(\xi+2\zeta)}{J^2} = f''_{\infty}, \tag{A.3}$$

where $\boldsymbol{\mathcal{I}}$ is the fourth-order identity tensor with components $[\boldsymbol{\mathcal{I}}]_{iIjJ} = \delta_{ij}\delta_{IJ}$. All remaining components of $[\mathbb{H}^{\infty}_{W}]$ (18) are zero.

Additionally, the diagonal components of the viscous Hessian $[\mathbb{H}^{\alpha}_{W}]$ are

$$W^{\alpha}_{\boldsymbol{F}\boldsymbol{F}} = \mu_{\alpha}\boldsymbol{\mathcal{I}}_{\boldsymbol{Y}^{-1}_{\alpha}}; \qquad W^{\alpha}_{JJ} = \frac{\mu_{\alpha}}{J^2}; \qquad W^{\alpha}_{\boldsymbol{Y}_{\alpha}\boldsymbol{Y}_{\alpha}} = \mu_{\alpha}\mathbb{C}; \qquad W^{\alpha}_{y_{\alpha}y_{\alpha}} = \frac{\mu_{\alpha}}{2}y_{\alpha}^{-2}, \tag{A.4}$$

and the non-zero off-diagonal components are

$$W^{\alpha}_{\boldsymbol{F}\boldsymbol{Y}_{\alpha}} = -\mu_{\alpha}\mathbb{A}; \qquad W^{\alpha}_{\boldsymbol{Y}_{\alpha}\boldsymbol{F}} = -\mu_{\alpha}\mathbb{B}, \tag{A.5}$$

where the fourth-order tensors are defined by

$$\begin{aligned}
[\mathbb{A}]_{IMKL} &= \left[\boldsymbol{F}\boldsymbol{Y}^{-1}_{\alpha}\right]_{IK}\left[\boldsymbol{Y}^{-1}_{\alpha}\right]_{ML};\\
[\mathbb{B}]_{IMKL} &= \left[\boldsymbol{Y}^{-1}_{\alpha}\right]_{IK}\left[\boldsymbol{F}\boldsymbol{Y}^{-1}_{\alpha}\right]_{ML};\\
[\mathbb{C}]_{IMKL} &= [\boldsymbol{Y}^{-1}_{\alpha}\boldsymbol{C}\boldsymbol{Y}^{-1}_{\alpha}]_{IK}\left[\boldsymbol{Y}^{-1}_{\alpha}\right]_{ML};\\
[\boldsymbol{\mathcal{I}}_{\boldsymbol{Y}^{-1}_{\alpha}}]_{iIjJ} &= \delta_{ij}[\boldsymbol{Y}^{-1}_{\alpha}]_{IJ}.
\end{aligned} \tag{A.6}$$

All other components of $[\mathbb{H}^{\alpha}_{W}]$ (18) vanish.

Appendix B. Entropy-stable stabilisation

Using expression (66), the semi-discrete entropy function of the system can be approximated via particle integration as

$$\sum_a \Omega^a_R \frac{dS_a}{dt} = \sum_a \Omega^a_R\left(\boldsymbol{v}_a \cdot \frac{d\boldsymbol{p}^a_R}{dt} + \boldsymbol{P}_a : \frac{d\boldsymbol{F}_a}{dt}\right) - \sum_a \Omega^a_R \dot{\mathcal{D}}^a_{\text{int}}. \tag{B.1}$$

Incorporating the discrete linear momentum and deformation gradient updates from (72a) and (72b), the sum of the first two terms in (B.1) becomes

$$\begin{aligned}
\sum_a \Omega^a_R\left(\boldsymbol{v}_a \cdot \frac{d\boldsymbol{p}^a_R}{dt} + \boldsymbol{P}_a : \frac{d\boldsymbol{F}_a}{dt}\right) = &\left[\underbrace{\sum_a \Omega^a_R\left(\boldsymbol{P} : \boldsymbol{\nabla}_0\boldsymbol{v}(\boldsymbol{X}_a, t) - \boldsymbol{v}_a \cdot \boldsymbol{T}_a\right)}_{0}\right] + \sum_a A^a_R \boldsymbol{v}^a_B \cdot \boldsymbol{t}^a_B\\
&+ \sum_a \Omega^a_R \boldsymbol{v}_a \cdot \boldsymbol{f}^a_R + \sum_a \boldsymbol{v}_a \cdot \boldsymbol{\mathcal{D}}_a.
\end{aligned} \tag{B.2}$$

Substituting this relation into (B.1) and rearranging terms yields

$$\sum_a \Omega^a_R \frac{dS_a}{dt} - \dot{\Pi}_{\text{ext}} = -\left[\sum_a \Omega^a_R \mathcal{D}^a_{\text{int}} + \underbrace{\left(-\sum_a \boldsymbol{v}_a \cdot \boldsymbol{\mathcal{D}}_a\right)}_{\dot{\mathcal{D}}_{\text{num}}}\right], \tag{B.3}$$

where the semi-discrete power contribution $\dot{\Pi}_{\text{ext}}$ is

$$\dot{\Pi}_{\text{ext}} = \sum_a \Omega^a_R \boldsymbol{v}_a \cdot \boldsymbol{f}^a_R + \sum_a A^a_R \boldsymbol{t}^a_B \cdot \boldsymbol{v}^a_B. \tag{B.4}$$

To satisfy the second law of thermodynamics (68) at the semi-discrete level, it is necessary to demonstrate that the two terms within the square brackets on the right-hand side of expression (B.3) are non-negative. The first term is straightforward, as the internal dissipation $\dot{\mathcal{D}}^a_{\text{int}} \geq 0$ must be non-negative by definition. For the second term, we must demonstrate the total numerical dissipation $\dot{\mathcal{D}}_{\text{num}} \geq 0$ is also non-negative. This can be achieved by equivalently swapping indices a and b, yielding

$$\dot{\mathcal{D}}_{\text{num}} = -\sum_a \boldsymbol{v}_a \cdot \boldsymbol{\mathcal{D}}_a = -\sum_a \sum_{b\in\Lambda_a}\left(\boldsymbol{v}_a \cdot \boldsymbol{\mathcal{D}}_{ab}\right) = -\sum_a \sum_{b\in\Lambda_a}\left(\boldsymbol{v}_b \cdot \boldsymbol{\mathcal{D}}_{ba}\right) = \sum_a \sum_{b\in\Lambda_a}\left(\boldsymbol{v}_b \cdot \boldsymbol{\mathcal{D}}_{ab}\right). \tag{B.5}$$

By averaging the second and fourth terms in the above expression and noting the anti-symmetric nature of the stabilisation term as $\boldsymbol{\mathcal{D}}_{ba} = -\boldsymbol{\mathcal{D}}_{ab}$, expression above can be alternatively shown as

$$\dot{\mathcal{D}}_{\text{num}} = \frac{1}{2}\sum_a \sum_{b\in\Lambda^b_a}\left(\boldsymbol{v}_b - \boldsymbol{v}_a\right) \cdot \boldsymbol{\mathcal{D}}_{ab}. \tag{B.6}$$

Sufficient conditions for $\dot{\mathcal{D}}_{\text{num}} \geq 0$ are given by

$$\boldsymbol{\mathcal{D}}_{ab} = \boldsymbol{S}_{ab}\left(\boldsymbol{v}_b - \boldsymbol{v}_a\right), \tag{B.7}$$

where $\boldsymbol{S}_{ab}$ is a symmetric positive semi-definite stabilisation matrix.

Appendix C. Linear viscoelastic model

This Appendix is included to derive the expressions for the Cauchy stress tensor and the evolution of internal variables for linear viscoelasticity. We begin by relating the small strain tensor $\boldsymbol{\varepsilon}$ to the deformation gradient tensor $\boldsymbol{F}$

$$\boldsymbol{\varepsilon} = \frac{1}{2}\left(\boldsymbol{\nabla}_0\boldsymbol{u} + (\boldsymbol{\nabla}_0\boldsymbol{u})^T\right) = \frac{1}{2}\left(\boldsymbol{F} + \boldsymbol{F}^T - 2\boldsymbol{I}\right), \tag{C.1}$$

where $\boldsymbol{u}$ is the displacement field and $\boldsymbol{I}$ is the identity tensor.

The strain energy density for the linear viscoelastic model is expressed as the sum of a long-term (equilibrium) component W_∞^{Lin} and a viscous (non-equilibrium) component W_α^{Lin}

$$W^{\text{Lin}}(\boldsymbol{\varepsilon}, \boldsymbol{\varepsilon}_{v_\alpha}) = W_\infty^{\text{Lin}}(\boldsymbol{\varepsilon}) + \sum_{\alpha=1}^{n_{\text{M}}} W_\alpha^{\text{Lin}}(\boldsymbol{\varepsilon}, \boldsymbol{\varepsilon}_{v_\alpha}), \tag{C.2}$$

with

$$W_\infty^{\text{Lin}}(\boldsymbol{\varepsilon}) = \mu(\boldsymbol{\varepsilon} : \boldsymbol{\varepsilon}); \qquad W_\alpha^{\text{Lin}}(\boldsymbol{\varepsilon}, \boldsymbol{\varepsilon}_{v_\alpha}) = \mu_\alpha\left(\boldsymbol{\varepsilon} - \boldsymbol{\varepsilon}_{v_\alpha}\right) : \left(\boldsymbol{\varepsilon} - \boldsymbol{\varepsilon}_{v_\alpha}\right), \tag{C.3a}$$

where μ and μ_α are the shear moduli of the long-term and viscous branches, respectively, and n_{M} denotes the number of Maxwell branches. The Cauchy stress tensor is then obtained from this energy as

$$\boldsymbol{\sigma}(\boldsymbol{\varepsilon}, \boldsymbol{\varepsilon}_{v_\alpha}) = \boldsymbol{\sigma}_\infty(\boldsymbol{\varepsilon}) + \sum_{\alpha=1}^{n_{\text{M}}} \boldsymbol{\sigma}_\alpha(\boldsymbol{\varepsilon}, \boldsymbol{\varepsilon}_{v_\alpha}). \tag{C.4}$$

with components

$$\boldsymbol{\sigma}_\infty = 2\mu\boldsymbol{\varepsilon}; \qquad \boldsymbol{\sigma}_\alpha = 2\mu_\alpha\left(\boldsymbol{\varepsilon} - \boldsymbol{\varepsilon}_{v_\alpha}\right). \tag{C.5}$$

The viscous internal variables evolve according to a standard linear relaxation law

$$\left.\frac{d\boldsymbol{\varepsilon}_{v_\alpha}}{dt}\right|_{\boldsymbol{\varepsilon}} = \frac{1}{\tau_\alpha}\left(\boldsymbol{\varepsilon} - \boldsymbol{\varepsilon}_{v_\alpha}\right), \tag{C.6}$$

where τ_α is the relaxation time of branch α. The exact time integration of this evolution equation over a time increment $\Delta t = t_2 - t_1$ yields

$$\boldsymbol{\varepsilon}_{v_\alpha}\Big|_{t_2} = (1 - \epsilon)\boldsymbol{\varepsilon}_{v_\alpha}\Big|_{t_1} + \epsilon\boldsymbol{\varepsilon}; \qquad \epsilon = 1 - e^{-\frac{\Delta t}{\tau_\alpha}}. \tag{C.7}$$

This formulation provides a consistent, linear viscoelastic framework in which stresses and internal variables are determined by the strain, the viscous history, and the material parameters.

References

[1] C.H. Lee, A.J. Gil, A. Ghavamian, J. Bonet, A total lagrangian upwind smooth particle hydrodynamics algorithm for large strain explicit solid dynamics, Comput. Methods Appl. Mech. Eng. 344 (2019) 209–250. http://www.sciencedirect.com/science/article/pii/S0045782518304857. https://doi.org/10.1016/j.cma.2018.09.033

[2] C.H. Lee, P.R. Refachinho De Campos, A.J. Gil, M. Giacomini, J. Bonet, An entropy-stable updated reference lagrangian smoothed particle hydrodynamics algorithm for thermo-elasticity and thermo-visco-plasticity, Comput. Particle Mech. 10 (2023) 1493–1531. https://doi.org/10.1007/s40571-023-00564-3

[3] P.R. Refachinho de Campos, A.J. Gil, C.H. Lee, M. Giacomini, J. Bonet, A new updated reference lagrangian smooth particle hydrodynamics algorithm for isothermal elasticity and elasto-plasticity, Comput. Methods Appl. Mech. Eng. 392 (2022) 114680. https://doi.org/10.1016/j.cma.2022.114680

[4] C.J. Runcie, C.H. Lee, J. Haider, A.J. Gil, J. Bonet, An acoustic riemann solver for large strain computational contact dynamics, Int. J. Numer. Methods Eng. 123 (23) (2022) 5700–5748. https://doi.org/10.1002/nme.7085

[5] O.I. Hassan, A. Ghavamian, C.H. Lee, A.J. Gil, J. Bonet, F. Auricchio, An upwind vertex centred finite volume algorithm for nearly and truly incompressible explicit fast solid dynamic applications: total and updated lagrangian formulations, J. Comput. Phys. X 3 (2019) 100025.

[6] T.B.J. Di Giusto, C.H. Lee, A.J. Gil, J. Bonet, M. Giacomini, A first-order hyperbolic arbitrary lagrangian eulerian conservation formulation for non-linear solid dynamics, Int. J. Numer. Methods Eng. 125 (15) (2024) e7467.

[7] T.B.J. Di Giusto, C.H. Lee, A.J. Gil, J. Bonet, C. Wood, M. Giacomini, A first-order hyperbolic arbitrary lagrangian eulerian conservation formulation for nonlinear solid dynamics in irreversible processes, J. Comput. Phys. 518 (2024) 113322.

[8] S. Reese, S. Govindjee, A theory of finite viscoelasticity and numerical aspects, Int. J. Solids Struct. 35 (26) (1998) 3455–3482. https://doi.org/10.1016/S0020-7683(97)00217-5

[9] J. Bonet, Large strain viscoelastic constitutive models, Int. J. Solids Struct. 38 (17) (2001) 2953–2968. https://doi.org/10.1016/S0020-7683(00)00215-8

[10] F. Marín, R. Ortigosa, J. Martínez-Frutos, A.J. Gil, Viscoelastic up-scaling rank-one effects in-silico modelling of electro-active polymers, Comput. Methods Appl. Mech. Eng. 389 (2022) 114358. https://doi.org/10.1016/j.cma.2021.114358

[11] G.A. Holzapfel, On large strain viscoelasticity: continuum formulation and finite element applications to elastomeric structures, Int. J. Numer. Methods Eng. 39 (22) (1996) 3903–3926.

[12] J. Lubliner, A model of rubber viscoelasticity, Mech. Res. Commun. 12 (2) (1985) 93–99. https://doi.org/10.1016/0093-6413(85)90075-8

[13] J.S. Bergström, M.C. Boyce, Constitutive modeling of the large strain time-dependent behavior of elastomers, J. Mech. Phys. Solids. 46 (5) (1998) 931–954.

[14] N. Huber, C. Tsakmakis, Finite deformation viscoelasticity laws, Mech. Mater. 32 (1) (2000) 1–18.

[15] Y. Vidal, J. Bonet, A. Huerta, Stabilized updated lagrangian corrected SPH for explicit dynamic problems, Int. J. Numer. Methods Eng. 69 (2006) 2687–2710.

[16] R. Naghdabadi, M. Baghani, J. Arghavani, A viscoelastic constitutive model for compressible polymers based on logarithmic strain and its finite element implementation, Finite Elem. Anal. Des. 62 (2012) 18–27.

[17] R.J. Clifton, X. Wang, T. Jiao, A physically-based, quasilinear viscoelasticity model for the dynamic response of polyurea 93 (2016) 8–15. https://doi.org/10.1016/j.jmps.2016.04.027

[18] P. Haupt, A. Lion, On finite linear viscoelasticity of incompressible isotropic materials, Acta Mech. 159 (1) (2002) 87–124.
[19] M.E. Gurtin, On the thermodynamics of materials with memory, Arch. Ration. Mech. Anal. 28 (1) (1968) 40–50.
[20] A. Kaye, Non-Newtonian Flow in Incompressible Fluids (1962). Report.
[21] B. Bernstein, E.A. Kearsley, L.J. Zapas, A study of stress relaxation with finite strain, Trans. Soc. Rheol. 7 (1) (1963) 391–410.
[22] X. Zeng, G. Scovazzi, N. Abboud, O. Colomés, S. Rossi, A dynamic variational multiscale method for viscoelasticity using linear tetrahedral elements, Int. J. Numer. Methods Eng. 112 (13) (2017) 1951–2003. https://doi.org/10.1002/nme.5591
[23] N. Abboud, G. Scovazzi, A variational multiscale method with linear tetrahedral elements for multiplicative viscoelasticity, Mech. Res. Commun. 112 (2021) 103610.
[24] A. Jeribi, The evolutionary problem, in: Perturbation Theory for Linear Operators: Denseness and Bases with Applications, Springer, 2021, pp. 131–175.
[25] S. Boyaval, Viscoelastic flows of maxwell fluids with conservation laws, ESAIM: M2AN 55 (3) (2021) 807–831.
[26] A.J. Gil, C.H. Lee, J. Bonet, R. Ortigosa, A first order hyperbolic framework for large strain computational solid dynamics. part II: total lagrangian compressible, nearly incompressible and truly incompressible elasticity, Comput. Methods Appl. Mech. Eng. 300 (2016) 146–181.
[27] J. Bonet, C.H. Lee, A.J. Gil, A. Ghavamian, A first order hyperbolic framework for large strain computational solid dynamics: part III: thermo-elasticity, Comput. Methods Appl. Mech. Eng. 373 (2021) 113505. https://doi.org/10.1016/j.cma.2020.113505
[28] G.A. Holzapfel, Nonlinear Solid Mechanics: A Continuum Approach for Engineering, Wiley and Sons, 2000.
[29] J. Bonet, A.J. Gil, R.D. Wood, Nonlinear Solid Mechanics for Finite Element Analysis: Statics, Cambridge University Press, 2016.
[30] J. Bonet, A.J. Gil, R.D. Wood, Nonlinear Solid Mechanics for Finite Element Analysis: Dynamics, Cambridge University Press, 2020.
[31] G.A. Holzapfel, Nonlinear Solid Mechanics: A Continuum Approach (2007) 455. ISBN: 0471823198.
[32] D.H. Wagner, Symmetric-hyperbolic equations of motion for a hyperelastic material, J. Hyperb. Differ. Equ. 06 (03) (2009) 615–630. https://doi.org/10.1142/S0219891609001940
[33] J. Bonet, A.J. Gil, C.H. Lee, M. Aguirre, R. Ortigosa, A first order hyperbolic framework for large strain computational solid dynamics. part i: total lagrangian isothermal elasticity, Comput. Methods Appl. Mech. Eng. 283 (2015) 689–732.
[34] Q. Tiehu, Symmetrizing nonlinear elastodynamic system, J. Elast. 50 (3) (1998) 245–252.
[35] G.-Q. Chen, C.D. Levermore, T.-P. Liu, Hyperbolic conservation laws with stiff relaxation terms and entropy 47 (6) (1994) 787–830. https://doi.org/10.1002/cpa.3160470602
[36] T. Kato, The cauchy problem for quasi-linear symmetric hyperbolic systems, Arch. Ration. Mech. Anal. 58 (3) (1975) 181–205.
[37] G. Warnecke, On godunov's interesting class of systems - the symmetric hyperbolic euler equations of gas dynamics, J. Comput. Phys. 522 (2025) 113588.
[38] E.H. Lieb, Convex trace functions and the Wigner-Yanase-Dyson conjecture, Adv. Math. 11 (3) (1973) 267–288.
[39] J. Bonet, A.J. Gil, R. Ortigosa, On a tensor cross product based formulation of large strain solid mechanics, Int. J. Solids Struct. 84 (2016) 49–63.
[40] J. Bonet, A.J. Gil, R. Ortigosa, A computational framework for polyconvex large strain elasticity, Comput. Methods Appl. Mech. Eng. 283 (2015) 1061–1094.
[41] C.H. Lee, A.J. Gil, G. Greto, S. Kulasegaram, J. Bonet, A new Jameson-Schmidt-Turkel smooth particle hdrodynamics algorithm for large strain explicit fast dynamics, Comput. Methods Appl. Mech. Eng. 311 (2016) 71–111.
[42] C.H. Lee, A.J. Gil, O.I. Hassan, J. Bonet, S. Kulasegaram, A variationally consistent streamline upwind petrov galerkin smooth particle hydrodynamics algorithm for large strain solid dynamics, Comput. Methods Appl. Mech. Eng. 318 (2017) 514–536.
[43] C. Linder, M. Tkachuk, C. Miehe, A micromechanically motivated diffusion-based transient network model and its incorporation into finite rubber viscoelasticity, J. Mech. Phys. Solids. 59 (10) (2011) 2134–2156.
[44] H. Badnava, C.H. Lee, S.H. Nourbakhsh, P.R. Refachinho De Campos, et al., A stabilised total lagrangian element-free galerkin method for transient nonlinear solid dynamics, Comput. Mech. 75 (1) (2025) 327–355.
[45] J.A. Trangenstein, A second-order Godunov algorithm for two-dimensional solid mechanics, Comput. Mech. 13 (1994) 343–359.
[46] G. Kluth, B. Després, Discretization of hyperelasticity on unstructured mesh with a cell-centered Lagrangian scheme, J. Comput. Phys. 229 (2010) 9092–9118.
[47] C.M. Dafermos, Quasilinear hyperbolic systems with involutions, Arch. Ration Mech. Anal. 94 (4) (1986) 373–389. https://doi.org/10.1007/BF00280911
[48] M. Aguirre, A.J. Gil, J. Bonet, C.H. Lee, An upwind vertex centred finite volume solver for Lagrangian solid dynamics, J. Comput. Phys. 300 (2015) 387–422.
[49] A.J. Gil, C.H. Lee, J. Bonet, M. Aguirre, A stabilised Petrov-Galerkin formulation for linear tetrahedral elements in compressible, nearly incompressible and truly incompressible fast dynamics, Comput. Methods Appl. Mech. Eng. 276 (2014) 659–690.
[50] C.H. Lee, A.J. Gil, J. Bonet, Development of a stabilised Petrov-Galerkin formulation for conservation laws in Lagrangian fast solid dynamics, Comput. Methods Appl. Mech. Eng. 268 (2014) 40–64. https://doi.org/10.1016/j.cma.2013.09.004
[51] I.A. Karim, C.H. Lee, A.J. Gil, J. Bonet, A two-step Taylor Galerkin formulation for fast dynamics, Eng. Comput. 31 (2014) 366–387. https://doi.org/10.1108/EC-12-2012-0319
[52] K.W.Q. Low, C.H. Lee, A.J. Gil, J. Haider, J. Bonet, et al., A parameter-free total Lagrangian smooth particle hydrodynamics algorithm applied to problems with free surfaces, Comput. Part. Mech. 8 (4) (2021) 859–892.
[53] T. Belytschko, W.K. Liu, B. Moran, Nonlinear Finite Elements for Continua and Structures, John Wiley and Sons, 2000.
[54] O. Gonzalez, A.M. Stuart, A First Course in Continuum Mechanics, Cambridge University Press, 2008.
[55] T. Gotoh, D. Sakoda, A. Khayyer, C.H. Lee, A. Gil, H. Gotoh, J. Bonet, et al., An enhanced total lagrangian SPH for non-Linear and finite strain elastic structural dynamics, Comput. Mech. 76 (1) (2025) 147–179.
[56] J. Bonet, T.S.L. Lok, Variational and momentum preservation aspects of smooth particle hydrodynamic formulations, Comput. Methods Appl. Mech. Eng. 180 (1999) 97–115. https://doi.org/10.1016/S0045-7825(99)00051-1
[57] J. Bonet, S. Kulasegaram, Correction and stabilization of smooth particle hydrodynamics methods with applications in metal forming simulations, Int. J. Numer. Methods Eng. 47 (2000) 1189–1214.
[58] A. Ghavamian, C.H. Lee, A.J. Gil, J. Bonet, T. Heuzé, L. Stainier, et al., An entropy-stable smooth particle hydrodynamics algorithm for large strain thermo-elasticity, Comput. Methods Appl. Mech. Eng. 379 (2021) 113736. https://doi.org/10.1016/j.cma.2021.113736
[59] A. Mayrhofer, B.D. Rogers, D. Violeau, M. Ferrand, Investigation of wall bounded flows using SPH and the unified semi-analytical wall boundary conditions, Comput. Phys. Commun. 184 (11) (2013) 2515–2527.
[60] J. Haider, C.H. Lee, A.J. Gil, J. Bonet, A first-order hyperbolic framework for large strain computational solid dynamics: an upwind cell centred total lagrangian scheme, Int. J. Numer. Methods Eng. 109 (3) (2017) 407–456. https://doi.org/10.1002/nme.5293
[61] J. Haider, C.H. Lee, A.J. Gil, A. Huerta, J. Bonet, et al., An upwind cell centred total Lagrangian finite volume algorithm for nearly incompressible explicit fast solid dynamic applications, Comput. Methods Appl. Mech. Eng. 340 (2018) 684–727.
[62] E.F. Toro, Riemann Solvers and Numerical Methods for Fluid Dynamics: A Practical Introduction, Springer-Verlag, 2nd ed., 2006.
[63] A. Khayyer, Y. Shimizu, C.H. Lee, A. Gil, H. Gotoh, J. Bonet, et al., An improved updated Lagrangian SPH method for structural modelling, Comput. Part. Mech. 11 (3) (2024) 1055–1086.
[64] M. Aguirre, A.J. Gil, J. Bonet, A.A. Carreño, A vertex centred finite volume Jameson-Schmidt-Turkel (JST) algorithm for a mixed conservation formulation in solid dynamics, J. Comput. Phys. 259 (2014) 672–699. https://doi.org/10.1016/j.jcp.2013.12.012
[65] C.H. Lee, A.J. Gil, J. Bonet, Development of a cell centred upwind finite volume algorithm for a new conservation law formulation in structural dynamics, Comput. Struct. 118 (2013) 13–38.
[66] G. Scovazzi, B. Carnes, X. Zeng, S. Rossi, A simple, stable, and accurate linear tetrahedral finite element for transient, nearly and fully incompressible solid dynamics: a dynamic variational multiscale approach, Int. J. Numer. Methods Eng. 106 (2016) 799–839.
[67] C.H. Lee, A.J. Gil, P.R. Refachinho de Campos, J. Bonet, T. Jaugielavičius, S. Joshi, C. Wood, A novel arbitrary Lagrangian Eulerian smooth particle hydrodynamics algorithm for nonlinear solid dynamics, Comput. Methods Appl. Mech. Eng 427 (2024) 117055.
[68] S. Terrana, N.C. Nguyen, J. Bonet, J. Peraire, A hybridizable discontinuous Galerkin method for both thin and 3D nonlinear elastic structures, Comput. Methods Appl. Mech. Eng. 352 (2019) 561–585.

[69] J.C. Simo, D.D. Fox, M.S. Rifai, On a stress resultant geometrically exact shell model. part II: the linear theory; computational aspects, Comput. Method Appl. Mech. Eng. 73 (1) (1989) 53–92.
[70] R. Hauptmann, K. Schweizerhof, A systematic development of 'solid-shell' element formulations for linear and non-linear analyses employing only displacement degrees of freedom, Int. J. Numer. Meth. Eng. 42 (1) (1998) 49–69.